UNIVERSIDADE DE LISBOA

FACULDADE DE CIÊNCIAS

DEPARTAMENTO DE ENGENHARIA GEOGRÁFICA, GEOFÍSICA E ENERGIA

Magnetic and gravimetric modeling of the Monchique magmatic intrusion in south Portugal

Gabriela Cunha Camargo

Mestrado em Ciências Geofísicas
Especialização em Geofísica Interna

Dissertação orientada por:
Dr. Susana Custódio, FCUL
Dr. Marta Neres, IPMA

2022

Acknowledgments

First of all, I would like to thank Dr. Marta Neres, who followed my work since the beginning and helped me in all matters of my research always with patience and understanding. I also thank Dr. Susana Custodio for accepting my invitation to do the orientation of this thesis along with Dr. Marta Neres, when it was already an ongoing project.

I also thanks Dr. Machiel Bos, the principal researcher in the Atlas project, where I have a research fellow scholarship founded by the FCT (Fundação de Ciencias e Tecnologia), and Dr. Pedro Terrinha head of the Division of Marine Geology in IPMA (Instituto Português de Mar e Atmosfera), the host institute of my scholarship.

Thanks to my mom, dad and sister that even being far away in Brazil, are always present in my daily life and supported me throughout all this past 5 years since I moved to Portugal.

And a special thanks to my friends, and all the people that helped me in any way to complete this chapter of my life.

Thank you all.

Abstract

The Monchique alkaline complex (MAC) crops out in southern Portugal with a roughly elliptical shape of about 80 km^2 elongated along the ENE-WSW direction. The MAC dates to the Late Cretaceous (69-72 Ma) and intrudes the Carboniferous Flysh formation of the South Portuguese Zone. At the surface, it comprises two main types of syenites: a central homogeneous nepheline syenite surrounded by a heterogeneous syenite unit, and some less expressive outcrops of mafic rocks (gabbros, hornfels, breccia and basalts). This igneous complex was formed during the Upper Cretaceous West Iberia alkaline magmatic event, which is characterized by alkaline magmatism of sublithospheric origin and was active from approximately 100 Ma to 69 Ma.

The Monchique region hosts the most active seismic cluster of mainland Portugal, with low magnitude earthquakes (M < 4) that occur along two lineations with NNE–SSW and WNW–ESE preferred orientations.

In this work we study the Monchique region through gravimetric and magnetic methods in order to: 1) better understand how the MAC influences the geomagnetic and gravimetric field in the region; 2) to create new and consistent 2D and 3D models for the intrusion; and 3) to help constrain the origin of the observed seismicity and its possible relationship with the existence of sub cropping magmatic bodies.

We process recently acquired data - ground gravity survey (49 points) and drone-borne aeromagnetic survey – and integrate it with existing data. The interpretation of the gravimetric results is complemented by a density analysis of the magmatic and host rocks. We perform 3D magnetic and gravity inversion to model the geometry of gravity and magnetic sources, and 2D magnetic forward modeling along a representative profile.

The calculated Bouguer gravity anomaly shows a positive gradient towards the southwest with a negative peak in the center of the Monchique Mountain. However, after applying the terrain correction (complete Bouguer anomaly), this peak vanishes. This is justified by the similar mean density values for the syenite and host rocks, respectively 2560 kg/m^3 and 2529 kg/m^3.

The gravity field shows a significant positive anomaly (both free-air and Bouguer) in the SW part of the study region, close to Ponta de Sagres. This anomaly and its associated gradient, complemented by results from our 3D density inversion model, imply the presence of high density rocks in this region suggesting a decrease in the crustal thickness and consequent shallowing of mantle materials.

The new aeromagnetic data allows to map the Monchique magnetic anomaly with unprecedented detail and reveal a 10 km elongated anomaly with 3 km wavelength and maximum 1707 nT amplitude. 3D magnetic susceptibility inversion models show a 15 km long body with maximum depth between 5-10 km, and susceptibility >0.02 SI, in agreement with previous susceptibility analysis of Monchique samples. The highest magnetic anomaly is found at Picota hill (east), but the deepest parts of the intrusion seem to be bellow Fóia hill (west). It is noteworthy that earthquake hypocenters concentrate at depths of 5-20 km, thus mostly below the modeled magmatic intrusion, indicating a fracture zone oriented preferentially ENE-WSW with hydrothermal activity.

Keywords

Monchique Alkaline Complex; Gravimetry; Geomagnetism; Oasis Montaj; 3D modeling.

Resumo

O complexo alcalino de Monchique (MAC) aflora no sul de Portugal com uma forma aproximadamente elíptica com cerca de 80 km^2 alongada na direção ENE-WSW. O MAC data do Cretáceo Superior (69-72 Ma) e intrui na formação do Flysh da Zona Sul Portuguesa, do Carbonífero. Na superfície, apresenta dois tipos principais de sienitos: um sienito nefelino homogêneo central cercado por uma unidade de sienito heterogênea, e alguns afloramentos menos expressivos de rochas máficas (gabros, corneanas, brechas e basaltos). Este complexo ígneo pertence ao evento magmático alcalino do Cretáceo Superior na Península Ibérica, caracterizado por magmatismo alcalino de origem sublitosférica e ativo de 100 Ma a 69 Ma, aproximadamente.

A região de Monchique alberga o aglomerado sísmico mais ativo de Portugal continental, com sismos de baixa magnitude (M < 4) que ocorrem ao longo de lineamentos com orientação preferencial NNE–SSW e WNW–ESE.

Neste trabalho estudamos a região de Monchique através de métodos gravimétricos e magnéticos com o objetivo de: 1) compreender melhor como o MAC influencia o campo geomagnético e gravimétrico na região; 2) criar modelos 2D e 3D novos e consistentes para a intrusão; e 3) ajudar a clarificar a origem da sismicidade observada e sua possível relação com a existência de corpos magmáticos sub aflorantes.

Neste trabalho, processamos dados recentemente adquiridos - levantamento gravimétrico terrestre (49 pontos) e levantamento aeromagnético realizado por drones - e os integramos aos dados previamente existentes. A interpretação dos resultados gravimétricos é complementada pela análise de densidade de rochas magmáticas e hospedeiras. Realizamos inversão magnética e gravítica 3D para modelar a geometria das fontes gravitacionais e magnéticas, e também fizemos modelagem direta magnética 2D ao longo de um perfil representativo.

A anomalia gravítica de Bouguer calculada mostra um gradiente positivo para sudoeste com um pico negativo no centro da Serra de Monchique. No entanto, quando aplicada a correção do terreno (anomalia Bouguer completa), este pico desaparece. Isso é justificado pelos valores de densidade média serem semelhantes para as rochas sieníticas encaixantes, respetivamente 2.560 kg/m^3 e 2.529 kg/m^3.

O campo magnético mostra uma significante anomalia positiva (tanto em free-air como em Bouguer) na parte SW da região de estudo, próximo a Ponta de Sagres. Esta anomalia e respetivo gradiente, complementados pelos nossos resultados da modelação 3D de densidade, implicam a presença de rochas com altas densidades na região, sugerindo um adelgaçamento da crusta.

Os novos dados aeromagnéticos permitem mapear a anomalia magnética de Monchique com um detalhe sem precedentes e revelam uma anomalia com um alongamento de 10 km, com 3 km de comprimento de onda, e com amplitude máxima de 1707 nT. Os modelos de inversão de suscetibilidade magnética 3D mostram um corpo de 15 km de comprimento com profundidade máxima entre 5-10 km, e suscetibilidade >0.02 SI, em concordância com análises de suscetibilidade anteriores em amostras de Monchique. A anomalia magnética mais alta encontra-se na colina da Picota (leste), mas as partes mais profundas da intrusão parecem estar abaixo da colina da Foia (oeste). É importante notar que os hipocentros sísmicos se concentram a profundidades de 5-20 km, portanto abaixo da maior parte da intrusão magmática modelada, indicando uma zona de fracturação orientada preferencialmente ENE-WSW com atividade hidrotermal.

Palavras-Chave

Complexo Alcalino de Monchique; Gravimetria; Geomagnetismo; Oasis Montaj; Modelação 3D.

Resumo alargado

O complexo alcalino de Monchique (MAC) aflora no sul de Portugal com uma forma aproximadamente elíptica com cerca de 80 km^2 alongada na direção ENE-WSW. O MAC data do Cretáceo Superior (69-72 Ma) e intrui na formação do Flysh da Zona Sul Portuguesa, do Carbonífero. A zona Sul Portuguesa é um dos quatro blocos que compõe o maciço ibérico em Portugal continental, ela é com composta de rochas do Paleozóico afetadas por metamorfismo de baixo grau. Monchique é um dos maiores corpos conhecidos de sienito nefelino com composição miasquítica, o maciço possui três elevações, de oeste para este: Picos, Fóia e Picota. Fóia e Picota são separadas por uma depressão onde a Ribeira de Monchique se localiza. São reconhecidos dois tipos principais de sienitos: (1) sienito nefelino homogêneo central com textura intergranular e bom desenvolvimento dos cristais de feldspato e nefelina; (2) unidade de sienito heterogênea de bordo que engloba a unidade anterior em todo o maciço. Há ainda alguns afloramentos menos expressivos de rochas máficas (gabros, corneanas, brechas e basaltos).

Este complexo ígneo pertence ao terceiro evento magmático alcalino do Cretáceo Superior na Península Ibérica, caracterizado por magmatismo alcalino de origem sublitosférica e ativo de 100 Ma a 69 Ma, aproximadamente. O alinhamento das três principais intrusões (Sintra, Sines e Monchique) sugere que os complexos foram controlados por falhas profundas com orientação NNW-SSE (Bonhomme et al., 1961; Neres et al., 2018; Ramos et al., 2017; Ribeiro, 1979). E o magma original, segundo Bernard-Griffiths et al. (1997), será do tipo basalto de ilha oceânica.

A região de Monchique alberga o aglomerado sísmico mais ativo de Portugal continental, com sismos de baixa magnitude (M < 4) que ocorrem ao longo de lineamentos com orientação preferencial NNE–SSW e WNW–ESE; e com concentração latitudinal entre 37.2º e 37.4º. A maioria dos hipocentros localizam-se entre 5 e 20 km de profundidade, com intensificação a partir do 10 km indicando uma crusta frágil até sua base (31 km). Monchique também é afetado por hidrotermalismo de baixa temperatura, e a mineralização da água indica sua circulação em profundidade por dentro do maciço.

No presente trabalho estudamos a região de Monchique através de métodos geofísicos gravimétricos e magnéticos com o objetivo de: 1) compreender melhor como o MAC influencia o campo geomagnético e gravimétrico na região; 2) criar modelos 2D e 3D novos e consistentes para a intrusão; e 3) ajudar a clarificar a origem da sismicidade observada e sua possível relação com a existência de corpos magmáticos sub aflorantes.

Neste trabalho, processamos dados recentemente adquiridos - levantamento gravimétrico terrestre (49 pontos) e levantamento aeromagnético realizado por drones - e os integramos aos dados previamente existentes – dados gravimétricos do IGP (Instituto Geográfico Português) coletados em 1997 e dados de anomalia aeromagnética da Ibéria de Socias and Mezcua (2002). A interpretação dos resultados gravimétricos é complementada pela análise de densidade de rochas magmáticas e hospedeiras, as amostras do encaixantes foram coletadas para o presente trabalho e as rochas magmáticas são preferencialmente da coletânea do pesquisador Vasco Valadares. Realizamos inversão magnética e gravítica 3D para modelar a geometria das fontes gravitacionais e magnéticas, e também fizemos modelagem direta magnética 2D ao longo de um perfil representativo (NNW-SSE). O processamento inicial dos dados foi realizado por meio programa desenvolvido pelo pesquisador Dr. Machiel Bos (correções de maré e instrumental para os dados gravimétricos; e correções instrumental e de variação diária geomagnética para os dados magnéticos) e o restante com o software Oasis Montaj da Seequent (incluindo as modelações 2D e 3D).

A junção dos dados gravimétricos analisados originou mapas de anomalias gravíticas com maior resolução que os preexistentes para o sudoeste de Portugal. A anomalia gravítica de Bouguer calculada

mostra um gradiente positivo para sudoeste com um pico negativo no centro da Serra de Monchique com valores entre are 98.5 e 38.2 mGal. No entanto, quando aplicada a correção do terreno (anomalia completa de Bouguer), este pico desaparece mostando apenas a tendência regional do campo. Isso é justificado pelos valores de densidade média serem semelhantes para as rochas sieníticas encaixantes, respetivamente 2.560 kg/m^3 e 2.529 kg/m^3.

O campo magnético mostra uma significante anomalia positiva (tanto em free-air como em Bouguer) na parte SW da região de estudo, próximo a Ponta de Sagres. Esta anomalia e respetivo gradiente, complementados pelos nossos resultados da modelação 3D de densidade, implicam a presença de rochas com altas densidades na região, sugerindo um adelgaçamento da crusta. Embora os nossos dados indiquem a presença de material mais denso até 10 km de profundidade, estudos sísmicos anteriores sugerem uma subida de material mantélico somente até os 25 km de profundidade.

Os novos dados aeromagnéticos permitem mapear a anomalia magnética de Monchique com um detalhe sem precedentes e revelam uma anomalia com um alongamento de 10 km, com 3 km de comprimento de onda, e com amplitude máxima de 1707 nT. Os modelos de inversão de suscetibilidade magnética 3D (produzidos com dados reduzidos e não reduzidos ao polo) mostram um corpo de 15 km de comprimento com profundidade máxima entre 5-10 km, e suscetibilidade >0.02 SI, em concordância com análises de suscetibilidade anteriores em amostras de Monchique. A anomalia magnética mais alta encontra-se na colina da Picota (leste), mas as partes mais profundas da intrusão parecem estar abaixo da colina da Foia (oeste). O modelo 3D também aponta um segundo corpo mais profundo a partir dos 17 km de profundidade, mas é preciso dados espacialmente mais abrangentes da área para se confirmar a existência desse corpo. Os dados de anomalia magnéticos da Ibéria, por terem sido adquiridos com grande espaçamento, possuem menos dados de alta frequência, mas a longa frequência está de acordo com os dados coletados pelo drone.

A modelação 2D dos dados magnéticos adquiridos em Monchique nos permitiu considerar duas opções de morfologia para a intrusão em profundidade. Vale ressaltar que esses modelos foram baseados nos resultados 3D e nas informações geológicas disponíveis sobre a zona. O modelo A é composto por uma única intrusão gabróide que se divide em vários ramos ao ascender, originando assim os vários corpos aflorantes de gabros. Neste modelo também é representado as duas tipologias de sienitos com diferentes suscetibilidades magnéticas. O modelo B difere do anterior por considerar mais de um corpo intrusivo de gabro e o sienito com forma de lacólito a seguir modelos anteriores do maciço de Sintra por Terrinha et al. (2018). Nos dois modelos o gabro atinge aproximadamente 8 km de profundidade (a continuação dos corpos em profundidade ainda está aberta para discussão) e o corpo de maior suscetibilidade deve ter um pendor para NW no seu limite Sul.

É importante notar que os hipocentros sísmicos se concentram a profundidades de 5-20 km, portanto abaixo da maior parte da intrusão magmática modelada, indicando uma zona de fracturação entre 10-17 km de profundidade que aparenta estar relacionada com atividade hidrotermal e orientada preferencialmente ENE-WSW. Essa orientação pode indicar uma estrutura ante mesozoica de condicionamento da instalação da intrusão como já foi sugerido por Clavijo and Valadares (2003). A estrutura avançaria para sul do maciço com fraturas que permitem a existências de nascentes de água aquecida nesta zona (temperaturas entre 27º e 31.5º C). A tomografia local existente (Veludo et al., 2017) também suporta a presença da zona de fracturação em profundidade, apesar de ainda ser necessária uma tomografia com maior resolução.

Palavras-Chave

Complexo Alcalino de Monchique; Gravimetria; Geomagnetismo; Oasis Montaj; Modelação 3D.

Índice

Figure index

Table Index

List of acronyms

IGP Instituto Geográfico Português

DEM Digital Elevation Model

IGRF International geomagnetic reference field

IAM Iberian anomaly map

IAM-R Iberian anomaly map regional

IAM-L Iberian anomaly map localized

RTP Reduction to pole

MAC Monchique Alkaline Complex

WIM West Iberia Margin

SPZ South Portuguese zone

GFBA Group Flysh do Baixo Alentejo

1. Introduction

1.1. Application of geophysical methods in geology

Geophysical methods are essential in the search for minerals, oil, water, and other resources commonly used in our daily life. Examples of geophysical methods are the electromagnetic, geothermal, electrical, radiometric, gravity, seismic and magnetic methods, all of them important for inferring the underground structures and consequently the geology of the studied location. The magnetic and the gravity methods are based in the study of the Earth's magnetic and gravity potential fields and allow the identification of compositional contrasts or anomalous bodies within the crust (Schubert, 2007). The seismic method is an acoustic method that allows imaging the subsurface structure through arrival times of seismic waves generated by acoustic sources and recorded by receptors (hydrophones or geophones) after reflection or refraction on the internal layers of the earth. The electrical methods determine variations on the electrical properties of the materials, i.e., resistivity, to acquire information about the bedrocks as salinity, soil contaminants, stratigraphy, among others. The radiometric method is used to estimate concentrations of radioelements such as potassium and uranium in the surface (Gupta, 2011). The geothermal method is based on the exchanges of heat or parameters sensible to changes in the temperature, important for the exploration of geothermal energy sources. The magnetic surveys are useful on mapping geological structures and finding the location of some magnetic minerals. The gravity is useful in fault problems, groundwater inventories and basin studies. The magnetic, gravity and seismic methods are the best ones for characterization of deeper parts of the earth, the electrical methods are normally used for studies in the superficial parts of the crust. In general, the definition of methods to use, the acquisition parameters and the planning of geophysical surveys depend on the geological target and on the intended resolution.

This work consists in the application of geophysical methods for the investigation of the Monchique magmatic intrusion located in the Algarve region, south of Portugal (Figure 1.1). We study the Monchique region using gravimetric and magnetic methods in order to better understand how this body influences the geomagnetic and gravimetric fields in the region; to obtain new and consistent 2D and 3D models based on new and previous data; and to integrate our results with other geophysical data. We also performed a density analysis in rock samples to support our findings. This work was developed under a research fellowship in the framework of the ATLAS project (PTDC/CTA-GEF/31272/2017, POCI-01-0145-FEDER-031272, FEDER-COMPETE/POCI 2020) partly funded by FCT (Fundação para a Ciência e a Tecnologia), in which the Instituto Português do Mar e da Atmosfera (IPMA), is a participant institution.

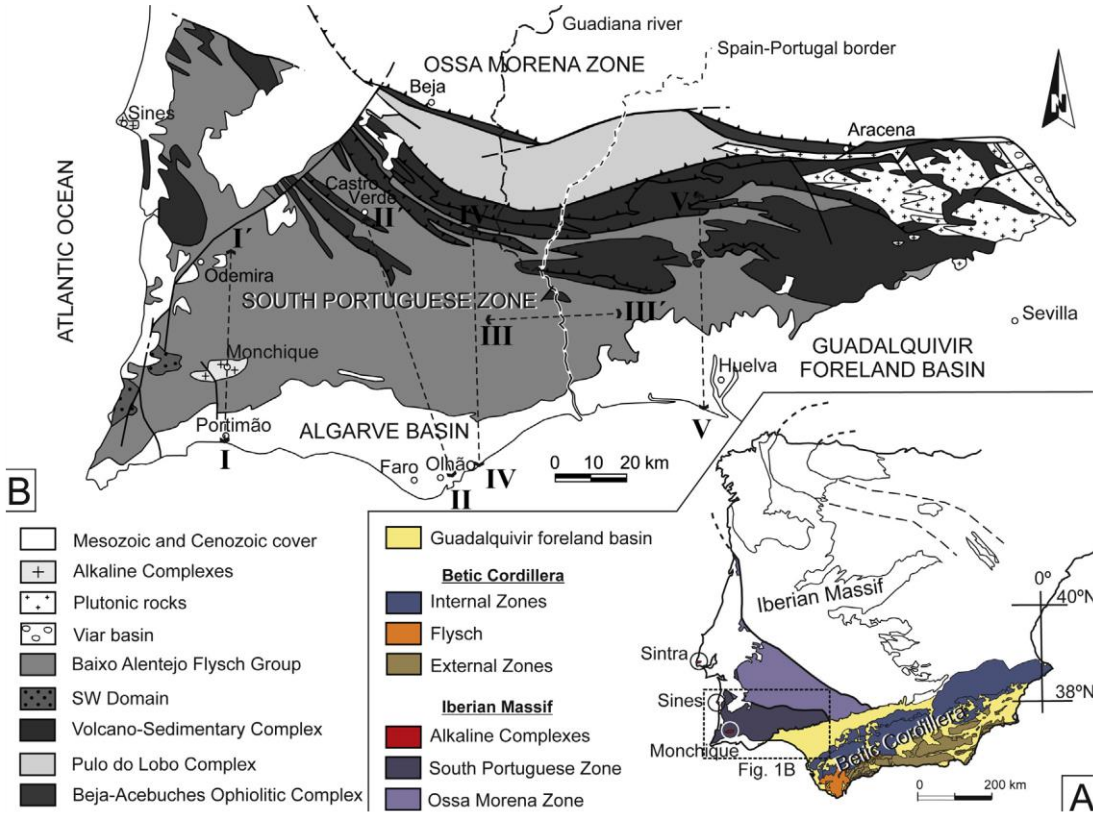

Figure 1.1 Geological setting of the study area. (A) Regional geological setting including the Sintra, Sines and Monchique massifs. (B) Geological setting of the South Portuguese Zone (that hosts the Monchique intrusion) and the Algarve Basin (from González-Castillo et al., 2013).

1.2. Theoretical background

The following theoretical background for gravity and magnetic methods is based on Blakely (1996), "Potential Theory in Gravimetry and Magnetic Applications". Both methods are based on the theory of potential fields. A field is a set of functions of space and time and is divided in two types: (1) scalar fields, describe some physical property of a material at each point and at a given time, like density, porosity, magnetization, and temperature; (2) vector fields, describe the forces that act at each point of space at a given time. The gravitational attraction of the Earth and the magnetic field induced by electrical currents are examples of vector fields.

The potential ϕ of a vector field $\boldsymbol{F}$ is defined as the work function or as its negative, depending on the convention used. The conventions of Kellogg (1953) states that: If particles of same sign attract each other (e.g., gravity fields), then $\boldsymbol{F} = \nabla\phi$ and the potential equals the work done by the field; if particles of same sign repel each other (e.g., electrostatic fields), then $\boldsymbol{F} = -\nabla\phi$, and the potential equals the work done against the field by the particle. In the last case, the potential ϕ is the potential energy of the particle; in the first case, ϕ is the negative of the particle's potential energy. The potential at a given point $\boldsymbol{P}$ is given by

$$\phi(P) = \int_{\infty}^{P} F \cdot ds \qquad (1.1)$$

An equipotential surface is a surface on which the potential remains constant, $\phi(x, y, z) = const$. It follows that field lines at any point are always perpendicular to their equipotential surfaces and, conversely, any surface that is everywhere perpendicular to all field lines must be an equipotential surface.

1.2.1. The Earth gravity field

For the application of gravity methods with the objective of studying the effect of density variations in the Earth's internal layers, measurements of the gravity field are conducted on the Earth's surface. A series of operations must then be applied to account for the mass, shape, and spin of a "normal" earth, elevation of the measurements above sea level, tidal effects of the Sun and Moon, motion of the instrument, gravitational effects of terrain in the vicinity of the measurement, and effects of isostasy. Application of these various operations, if they are successful, will leave us with a gravity anomaly field that reflects the density variations in the crust and upper mantle. Here we describe only the theory behind the procedures used to analyze our data. These operations are based on the potential field theory and its consequences, and the Newtonian potential (gravitational attraction and potential, Poisson's equation and Gauss's law for gravity fields).

An equipotential surface of particular interest for gravity measurements is the geoid, the equipotential surface described by sea level without the effects of ocean currents, weather, and tides. The shape of the geoid is influenced by underlying masses; it bulges above mass excesses and is depressed over mass deficiencies. Because the geoid is an equipotential surface, the force of gravity at any point on the geoidal surface must be perpendicular to the surface, thereby defining "vertical" and "level" at each point. Because of the complexity of internal density variations, it is customary to reference the geoid to a simpler, smoother surface. By international agreement, that equipotential surface is the spheroidal surface that would bound a rotating, uniformly dense earth. The spheroid very nearly has the shape of an ellipse of revolution and, consequently, is called the reference ellipsoid (Figure 1.2).

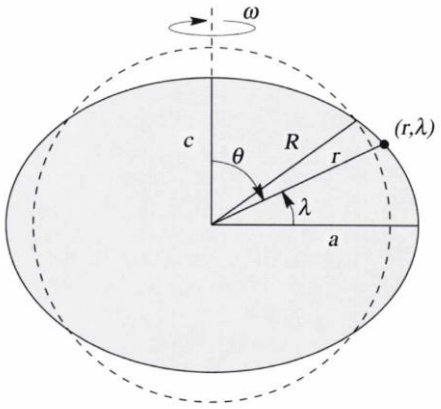

Figure 1.2 Parameters involved in describing reference ellipsoid (figure 7.2 in Blakely, 1996). Where θ is colatitude, ω is angular velocity, λ is the latitude, a is equatorial radius.

The simple relation describing the total gravitational attraction of the spheroid, can be written as

$$g_0 = g_e(1 + \alpha \sin^2 \lambda + \beta \sin^2 2\lambda) \tag{1.2}$$

where g_0 is used here to denote the total gravity of the spheroid and g_e is the gravitational attraction on the equator, and α and β are coefficients depending on ω, a and the total mass. The ellipsoid is defined and refined by international agreement through the International Association of Geodesy (IAG) and its umbrella organization, the International Union of Geodesy and Geophysics (IUGG). Most recently the IAG has adopted the Geodetic Reference System 1980, which eventually led to the current reference field, the World Geodetic System 1984 (WGS84), which is given by

$$g_0 = 9.7803267714 \frac{1 + 0.00193185138639 \sin^2 \lambda}{\sqrt{1 - 0.00669437999013 \sin^2 \lambda}} \quad (1.3)$$

This equation is commonly referred to as theoretical gravity or normal gravity. The observed gravity is a sum of various factors that include the attraction of the reference ellipsoid, the effect of elevation above sea level (free-air correction), the effect of mass above or below sea level (Bouguer and terrain corrections), the tidal and isostasy effects. The acceleration of gravity at the surface of the Earth due to its whole mass is approximately 9.8 $m.s^{-2}$ (980 Gal), whereas anomalies caused by crustal density variations are typically less than 10^{-3} $m.s^{-2}$ (100 mGal), less than 0.01 percent of the observed gravity.

Free-air correction

Gravity measurements over land must be adjusted to account for the elevation above or below sea level. Let $g(r)$ represent the attraction of gravity on the geoid. The value of gravity for a small distance h above the geoid is given by

$$g(r) = g(r+h) - \frac{2g(r)}{r}h \quad (1.4)$$
$$\frac{2g(r)}{r}h = g_{fa}$$

The last term of this equation accounts for the difference in elevation between $g(r)$ and $g(r+h)$. It is known as the free-air correction g_{fa} because it is the only elevation adjustment required if no masses were to exist between the observation point and sea level. Using values of g and r at sea level provides

$$g_{fa} = -0.3086 \times 10^{-5} h \quad (1.5)$$

where h is height above sea level. Application of the free-air correction provides the free-air anomaly given by

$$\Delta g_{fa} = g_{obs} - g_{fa} - g_0 \quad (1.6)$$

where g_{obs} is the observed gravity. The free-air correction adjusts the measured gravity for one factor not accounted for by the reference ellipsoid: the elevation of the gravity measurement above the reference ellipsoid. Although the free-air correction accounts for the elevation of the observation point, the observation point remains fixed in space with respect to all causative masses.

Tidal correction

Earth-tides caused by the gravitational interactions with the Sun and Moon are of sufficient amplitude to be detected by gravity meters as time-varying gravity. The effect is both time- and latitude-dependent; it is greatest at low latitudes and has a strong periodic component with the strongest periodicity on the order of 12 hours. The tidal effect never exceeds $3x10^{-6}$ $m.sec^{-2}$ (0.3 mGal). This problem is usually treated by reoccupying certain observation points at various times during the day, assuming that drift has been linear between the repeated measurements and subtracting the linear drift from all other readings. The tidal effect can be considered part of the instrumental drift.

Bouguer correction

The free-air correction and theoretical gravity ignore the mass that may exist between the level of observation and sea level. The Bouguer correction accounts for this additional mass. The simple Bouguer correction approximates all mass above sea level with a homogeneous, infinitely extended slab of thickness equal to the height of the observation point above sea level; this infinite slab is called the Bouguer plate. The attraction of an infinite slab is described by

$$g_{sb} = 2\pi\gamma\rho h \tag{1.7}$$

Where h is the thickness of the slab, ρ is the assumed slab density and γ is Newton's gravitational constant (6.67 x 10^{-11} $m^3.kg^{-1}.s^{-2}$ in SI units). Using a typical crustal density of 2670 $kg.m^{-3}$, the simple Bouguer correction becomes $g_{sb} = 0.1119 \times 10^{-5} h$. The simple bouguer anomaly is given by

$$\Delta g_{sb} = g_{obs} - g_{fa} - g_{sb} - g_0 \tag{1.8}$$

The Bouguer anomaly reflects "anomalous mass"; i.e., masses with density above or below 2670 $kg.m^{-3}$. The choice of 2670 $kg.m^{-3}$ as an average crustal density is appropriate for most geologic situations. Note that the anomaly now reflects the density contrast of the anomalous masses with respect to normal density, rather than their total densities.

Terrain correction (complete Bouguer correction)

By assuming an infinite slab of mass around the observation point, the simple Bouguer anomaly ignores the shape of the topography. In either case, a simple Bouguer correction tends to overcompensate measurements made near topographic features. The terrain correction g_{t} adjusts for this overcompensation and is an essential step in reducing measurements in places of moderate to extreme topographic relief. The result is the complete Bouguer anomaly:

$$\Delta g_{cb} = g_{obs} - g_{fa} - g_{sb} - g_{\mathrm{t}} - g_0 \tag{1.9}$$

Where g_{t} is always negative and is traditionally calculated by approximating the topography with a digital terrain model and calculating the gravitational attraction of the model with techniques such as those discussed in Chapters 9 and 11 of (Blakely, 1996). Bouguer anomalies typically show a strong inverse correlation with long-wavelength topography such as mountain chains. This is because although the Bouguer correction accounts for the direct effects of the topographic edifice, it does not account for the low-density root that isostatically supports the topography. Hence, the Bouguer anomaly in this scenario is strongly negative because the gravitational effects of the compensating root remain unaccounted for in the anomaly. For similar reasons, Bouguer anomalies are negative over continental areas and positive over ocean basins because of the different crustal thicknesses between the two regimes. The Bouguer correction is sometimes referred to as a stripping away of all material down to sea level. More accurately, it accounts for normal crust (i.e., density = 2670 $kg.m^{-3}$) above sea level, specifically that part of the "normal" earth not accounted for by theoretical gravity.

1.2.2. Magnetic potential, magnetic induction and magnetic field intensity

The magnetic potential results from the property of magnetic induction of the electrical loop currents, described by Lorentz force and Biot-Savart law

$$B = C_m I_b \oint \frac{(dl_b \times \hat{r})}{r^2} \tag{1.10}$$

Where the factor C_m is a proportionality constant, I_b is the current of a loop of current and dl_b is a small element of loop, and r is the distance between loops. $\boldsymbol{B}$ is called the magnetic induction, magnetic flux density, or simply the magnetic field of a loop of current. Magnetic induction is defined as follows: electric current induces a force on a moving charge; the force is the vector product of the magnetic induction field and the velocity of the charge. In the EMU (electromagnetic system), magnetic induction $\boldsymbol{B}$ is reported in units of gauss (G), and current has units of abamperes (abA). In SI (Système Internationale) units, $\boldsymbol{B}$ has units of tesla (T), and current is in units of ampere (1 ampere = 0.1 abampere).

The magnetic induction of a magnetic dipole at points other than the dipole itself is

$$\mathrm{B} = C_m \frac{m}{r^3}[3(\hat{m}\cdot\hat{r})\hat{r} - \hat{m}], \qquad r \neq 0 \tag{1.11}$$

Equation (1.11) describes the vector field of a small bar magnet. The magnitude of $\boldsymbol{B}$ is proportional to the dipole moment (m) and inversely proportional to the cube of the distance to the dipole (r). The direction of $\boldsymbol{B}$ depends on the directions of both r and m ($m = I\,\hat{n}\,\Delta s$, where Δs is the area of the loop and $\hat{n}$ is a unit normal vector). All flux lines of $\boldsymbol{B}$ emanate from the positive end of m and ultimately return to the negative end.

Magnetization

We define a vector quantity called magnetization $\boldsymbol{M}$ as follows: The magnetization of a volume V is defined as the vector sum of all the individual dipole moments m_i divided by the volume. Magnetization is reported in units of ampere-meter^{-1} in the SI and in units of gauss in EMU, where 1 gauss = 10^3 A.m^{-1}. Consider now a small element of magnetic material with magnetization $\boldsymbol{M}$ that can be considered to act like a single dipole $Mdv = m$. In general, magnetization $\boldsymbol{M}$ is a function of position, where both direction and magnitude can vary from point to point, that is, $M = M(Q)$, where Q is the position of dv. The potential of a distribution of magnetization integrated for all the elemental volumes provided is

$$V(P) = C_m \int_R M(Q)\cdot\nabla_Q \frac{1}{r} dv \tag{1.12}$$

And the magnetic induction at point P is given by

$$B(P) = -\nabla_P V(P) = -C_m \nabla_P \int_R M(Q)\cdot\nabla_Q \frac{1}{r} dv \tag{1.13}$$

Where r is the distance from point P to the dipole field. Now we consider a second kind of magnetic field which proves useful in the presence of magnetic materials, this is a part of $\boldsymbol{B}$ arising from all currents other than atomic-level currents associated with magnetization. The second Maxwell equation states that the curl of $\boldsymbol{B}$ is equal to the vector- sum of the various forms of charge moving in a region can be written as

$$\nabla \times B = 4\pi C_m (I_m + \nabla \times M) \tag{1.14}$$

From here the derivation in SI and EMU system, according to C_m values, will yield respectively

$$\begin{gathered} \nabla \times \left(\frac{B}{4\pi C_m} - M\right) = I_m, \\ \nabla \times H = I_m, \\ H = \frac{B}{\mu_0} - M. \end{gathered} \tag{1.15}$$

$$\begin{gathered} \nabla \times (B - 4\pi C_m) = 4\pi C_m I_m, \\ \nabla \times H = 4\pi C_m I_m, \\ H = B - 4\pi M \end{gathered}$$

Vector $\boldsymbol{H}$ is a new quantity called the magnetic field intensity, and as can be seen from the defining equations, it is simply magnetic induction (except for a factor μ_0, permeability of free space in SI units) minus the effects of magnetization. Field intensity has units of oersteds (Oe) in the emu system and units of ampere.meter^{-1} in SI units. These equations show that the magnetic field intensity is a hybrid vector function composed of two components with quite different physical meanings. Whereas magnetic induction $\boldsymbol{B}$ originates from all currents, both atomic and macroscopic, magnetic field intensity $\boldsymbol{H}$ arises only from true currents (again ignoring displacement currents).

Magnetic permeability and susceptibility

Materials can acquire a component of magnetization in the presence of an external magnetic field. For low-amplitude fields, on the order of the Earth´s magnetic field (between 25000-65000 nT), this induced magnetization is proportional in magnitude and is anti-parallel or parallel to the direction to the external field, that is $M = \chi H$. The proportionality constant χ is called the magnetic susceptibility. It is dimensionless in both system SI and EMU and the two differ by 4π, emu=4π SI. For the magnetic permeability μ, in emu system

$$\mu = 1 + 4\pi\chi \tag{1.16}$$

In SI

$$\mu = \mu_0(1 + \chi) \tag{1.17}$$

Three types of magnetizations may occur in materials. Diamagnetism is an inherent property of all matter, and it is caused by the disturbance of the orbital motion of electrons in a way to induce a small magnetization in the opposite sense to the applied field ($\chi < 0$). Paramagnetism is a property of solids that have atomic magnetic moments. In the presence of a magnetic field, the atomic moments partially align parallel to the applied field thereby producing a net magnetization in the direction of the applied field ($\chi > 0$). Paramagnetism vanishes in the absence of applied fields because the competing thermal effects overcome to randomly orient the atomic moments. All minerals are diamagnetic, and some are paramagnetic, but in either case the resulting magnetization is very low amplitude. Certain minerals not only have atomic moments, but in addition neighboring moments interact strongly with each other, causing a property called ferromagnetism (s.l.). Ferrmagnetic materials may express ferromagnetism *(s.s.)*, in which atomic moments are aligned parallel to one another; antiferromagnetism, where atomic moments are aligned antiparallel and cancel one another; and ferrimagnetism, in which atomic moments are antiparallel but do not cancel.

Hence, rocks can acquire a net magnetization called induced magnetization and denoted by M_i in the direction of an applied filed $\boldsymbol{H}$, where

$$M_i = \chi H \tag{1.18}$$

However, ferromagnetic minerals can retain a magnetization even in the absence of an external magnetic field. This permanent magnetization is called remanent magnetization, which is denoted by M_r. The total magnetization $\boldsymbol{M}$ of a rock is then the vector sum of its induced and remanent magnetizations:

$$M = M_i + M_r = \chi H + M_r \tag{1.19}$$

Magnetite (Fe_3O_4) is the most important magnetic mineral for geophysical studies of crustal rocks, it is a ferrimagnetic mineral found in igneous, metamorphic, and sedimentary rocks; and has an elevated magnetic susceptibility when compared to other magnetic minerals (Barbosa, 1999). Mafic rocks are more magnetic than silicic rocks. Hence, basalts are usually more magnetic than rhyolites, and gabbros are more magnetic than granites. Also, extrusive rocks generally have a higher remnant magnetization and lower susceptibility then intrusive rocks with the same chemical composition. Sedimentary and metamorphic rocks often have low remnant magnetizations and susceptibilities.

1.2.3. The geomagnetic field

The geomagnetic field comprises internal and external field components. The internal field is due to the Earth´s inner core rotation and to crustal magnetism, and the external field is caused by the interaction with the solar wind in the ionosphere and magnetosphere. Spherical harmonic analysis provides the

means to determine, from measurements of a potential field and its gradients on a sphere, whether the sources of the field lie within or outside the sphere.

The equation of the potential is commonly written as

$$V = a\sum_{n=0}^{\infty}\left[\left(\frac{r}{a}\right)^{n} \mathrm{T}_n^e + \left(\frac{r}{a}\right)^{n+1} \mathrm{T}_n^i\right] \tag{1.20}$$

Where

$$\mathrm{T}_n^i = \sum_{m=0}^{\mathrm{n}} \left(\mathrm{g}_n^{mi}\cos m\phi + \mathrm{h}_n^{mi}\sin \mathrm{m}\phi\right)\mathrm{P}_n^m(\theta) \tag{1.21}$$

$$\mathrm{T}_n^e = \sum_{m=0}^{\mathrm{n}} (\mathrm{g}_n^{me}\cos m\phi + \mathrm{h}_n^{me}\sin \mathrm{m}\phi)\mathrm{P}_n^m(\theta) \tag{1.22}$$

Where θ is colatitude, ϕ is longitude, and $\mathrm{P}_n^m(\theta)$ is an associated Legendre polynomial of degree n and order m normalized according to the convention of Schmidt, a is the radius of the Earth and r is the distance between measurements and sources. The coefficients $\mathrm{g}_n^{mi}, \mathrm{h}_n^{mi}, \mathrm{g}_n^{me}, \mathrm{h}_n^{me}$ are called Gauss coefficients, have the same dimensions as magnetic induction, and generally are expressed in units of nanotesla (or gamma).

The external sources of the geomagnetic field contribute several tens of nT (and often much more) to the total magnetic field at the Earth's surface, and that contribution is highly variable in both time and space. The magnetic field originating from inside the Earth, the internal field, is approximately dipolar (Figure 1.3). The Earth, however, is continuously bathed by the solar wind, a stream of charged plasma emitted by the sun. The region of interaction between the solar wind and the internal magnetic field is called the magnetosphere. It is this complex interaction between the earth's internal magnetic field and the solar wind, coupled with the earth's rotation, tidal forces, and thermal effects, that produces the external magnetic field.

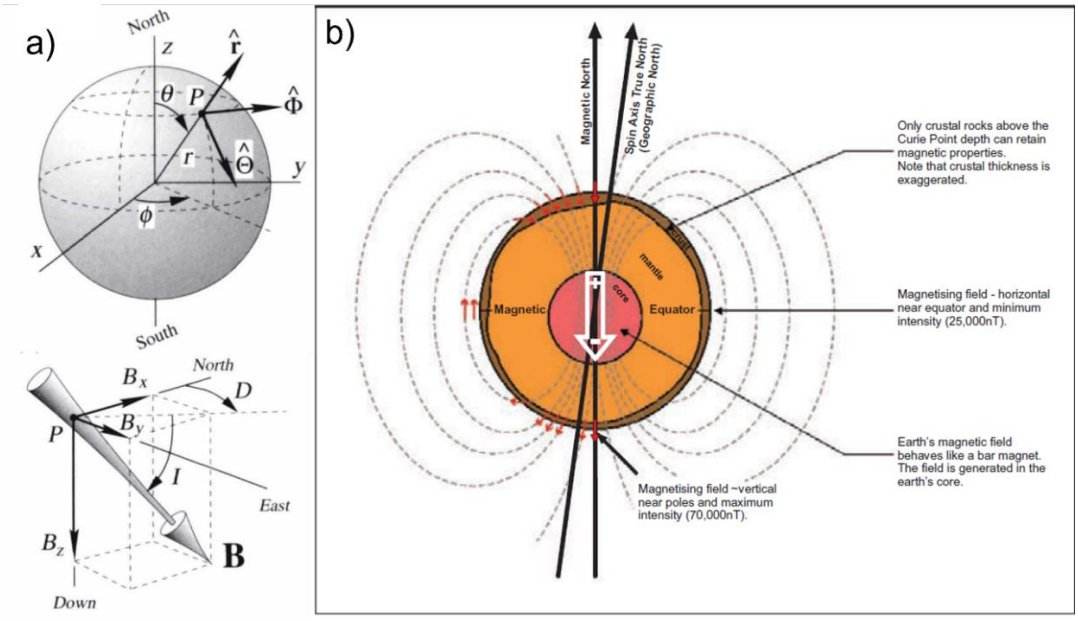

Figure 1.3 a) The spherical coordinate system and the cartesian coordinate system at point P. The three components of vector B are shown: Bx is directed north, By is east, and Bz is down. Inclination I is the angle of B below horizontal, positive

down; declination D is the azimuth of the horizontal projection of B, positive east (modified from (Blakely, 1996). b) the Schematic section through the earth showing the main features of its magnetic field (from Isles and Rankin, 2018).

The elements of the geomagnetic field

Vector quantities (e.g., $\boldsymbol{B}$, $\boldsymbol{H}$, and $\boldsymbol{M}$) in geomagnetic studies are described in a fixed reference frame with respect to observation points on the Earth's surface. The vector can be described in terms of three orthogonal components in a cartesian coordinate system, usually oriented so that *x* increases to the north, *y* is east, and *z* is down (Figure 1.3). The intensity of the horizontal component is

$$H = \sqrt{B_x^2 + B_y^2} \tag{1.23}$$

And the total intensity is

$$T = \sqrt{B_x^2 + B_y^2 + B_z^2} \tag{1.24}$$

The inclination is the vertical angle between the vector and the horizontal plane

$$I = \arctan \frac{B_z}{\sqrt{B_x^2 + B_y^2}} \tag{1.25}$$

By convention, inclination is positive when the vector is inclined below the horizontal plane and negative when above the horizontal plane. The vertical plane containing the vector is called the magnetic meridian, and declination is defined as the azimuth of the magnetic meridian (with respect to the geographic pole), positive to the east and negative to the west, that is,

$$D = \arcsin \frac{B_y}{\sqrt{B_x^2 + B_y^2}} \tag{1.26}$$

Contour maps describing these various elements of the geomagnetic field are called isomagnetic maps. Isodynamic maps indicate contours of equal field intensity, such as total intensity, vertical intensity, or horizontal intensity. Isoclinal maps show contours of equal inclination, and isogonic maps represent declination.

The international geomagnetic reference field (IGRF)

The IGRF consists of Gauss coefficients till degree/order 10 because, these low-order terms are believed to represent in large part the field of the earth's core. Subtracting these low-order terms from measured magnetic fields provides in principle the magnetic field of the crust. Because international agreement is not easily achieved on a day-to-day basis, IAGA (International Association of Geomagnetism and Aeronomy) adopts new IGRF models at five-year intervals which are intended to represent the geomagnetic field for the following five-year period, called an epoch.

The first-degree harmonic terms of the geomagnetic field describe the potential of a dipole centered at the center of the sphere, and the large amplitudes of these coefficients reflect the generally geocentric dipolar character of the main geomagnetic field. The extension of the positive end of the geocentric dipole intersects the Earth's surface at coordinates (θ, ϕ) = (169.1°, 108.9°), or at latitude 79.1°S and longitude 108.9°E; the negative end intersects the surface at (θ, ϕ)= (10.9°, 288.9°), or at latitude 79.1°N and longitude 71.1°W in the Kane Basin between Ellesmere Island and Greenland. These two points are called the south and north geomagnetic poles, respectively. The magnetic poles, on the other hand, are the points where the total field is normal to the surface of the earth, that is, the south magnetic pole is that point where the inclination is —90° and the north magnetic pole is located where the

inclination reaches +90°. If the geomagnetic field was perfect, the distinction between geomagnetic poles and magnetic poles would be unnecessary. Excluding the n = 1 harmonic from the equation of the internal sources eliminates the dipole term from the geomagnetic field, which leaves us with the nondipole field. The nondipole field comprises only about 10 percent of the main field, and thus the geomagnetic field is dipolar to a very good first approximation. The nondipole field is characterized by large-scale anomalies, eight or ten in number, with spatial dimensions comparable to continental size (although no correlation is apparent), and with magnitudes on the order of 104 nT. The various terms of a spherical harmonic expansion represent the potentials of highly idealized sources (monopoles, dipoles, quadrupoles, and so forth) situated precisely at the center of the sphere.

Crustal anomaly field

The internal sources of the geomagnetic field are located primarily in two regions of the Earth. The majority of the field is generated in the fluid outer core by way of complex magnetohydrodynamic processes and is called the core field or main field. The remainder, called the crustal field, originates primarily from a relatively thin outer shell of the Earth where temperatures are below the Curie temperatures (T_C) of important magnetic minerals, primarily magnetite (T_C=570°C) and titanomagnetite (T_C dependent on titanium content). The calculation of crustal magnetic anomalies then amounts to subtracting the components due to the core field and external field from measurements of the total magnetic field. The large difference in depth between the sources of the crustal and core field is reflected in spherical harmonic analyses.

The total field anomaly is calculated from total field measurements by subtracting the magnitude of a suitable regional field, usually the IGRF model appropriate for the date of the survey. If $\boldsymbol{T}$ represents the total field at any point, and $\boldsymbol{F}$ is the regional field at the same point, then the total field anomaly is given by

$$\Delta\mathrm{T} = |\mathrm{T}| - |\mathrm{F}| \tag{1.27}$$

It is important to establish under what conditions ΔT is harmonic. Let ΔF represent the perturbation of $\boldsymbol{F}$ due to some anomalous magnetic source. Then the total field is given by

$$T = F + \Delta F \tag{1.28}$$

Note that the total field anomaly is not equivalent to the magnitude of the anomalous field because $\Delta\mathrm{T} = |\mathrm{F} + \Delta\mathrm{F}| - |\mathrm{F}| \neq |\Delta\mathrm{F}|$. The total field anomaly is a good approximation of one component of ΔF and moreover can be considered a harmonic function. The first of these conditions is met if the anomalous field is small compared to the ambient field. If $|F| \gg |\Delta F|$, then

$$\Delta\mathrm{T} \approx \hat{F} \cdot \Delta F \tag{1.29}$$

Which is the projection of ΔF onto F. Hence, if the ambient field is much larger than the perturbing field, ΔT is approximately equal to one component of the field produced by the anomalous magnetic sources, namely the component in the direction of the regional field. The condition $|F| \gg |\Delta F|$ is usually met in studies of crustal magnetization. The total field anomaly at any point is approximately equal to the component of the anomalous field in the direction of the regional field if the anomaly field is small compared to the ambient field. In addition, the total-field anomaly is a potential and satisfies Laplace's equation if the direction of the ambient field is constant over the dimensions of the survey.

1.2.4. Inverse and forward methods

Main techniques of interpretation of potential field data can be divided into three categories:

- Forward method: An initial model for the source body is constructed based on geologic and geophysical intuition. The model's anomaly is calculated and compared with the observed anomaly, and model parameters are adjusted in order to improve the fit between the observed and modeled anomalies. This three-step process of body adjustment, anomaly calculation, and anomaly comparison is repeated iteratively until calculated and observed anomalies are deemed sufficiently alike.

- Inverse method: One or more body parameters are estimated by solving an inverse problem using as input the observed anomaly field. Simplifying assumptions are inevitable but parameter and geometrical constraints may help to improve the realism of the inversion, although the inversions results are never unique.

- Data improvement and display: No model parameters are calculated per se, but the anomaly field is processed in order to enhance certain characteristics of the source, thereby facilitating the overall interpretation. Different operations may be applied to enhance different aspects of the anomaly field.

The interpretation in any case will be inherently non-unique (Saltus and Blakely, 2011), but incorporation of independent information may reduce the infinite set of mathematical solutions to a manageable array of models, still infinite in number but at least more geologically reasonable.

1.2.4.1. Forward method

In forward modeling, crustal and upper-mantle lithology and structure can be deduced from gravity or magnetic measurements. Source parameters are estimated indirectly through trial-and-error calculations.

The gravitational potential U and gravitational acceleration g at point P due to a volume of mass with density ρ are

$$U(P) = \gamma \int_R \frac{\sigma}{r} dv \tag{1.30}$$

$$g(P) = \nabla(\mathrm{U}) = -\gamma \int_r \rho \frac{\hat{r}}{r} dv \tag{1.31}$$

Where r is the distance from P to an element of the body dv, γ is the gravitational constant and σ is the surface density with units of mass per unit area. Gravimeters measure the vertical attraction of gravity (i.e., in the direction of increasing z), here denoted by g. In cartesian coordinates, therefore,

$$g(x,y,z) = \frac{\partial U}{\partial z} = -\gamma \int_{z'} \int_{y'} \int_{x'} \rho(x',y',z') \frac{(z-z')}{r^3} dx'dy'dz' \tag{1.32}$$

The Green's function in this equation is simply the gravitational attraction at (x,y,z) of a point mass located at (x',y',z'). The forward method requires the repeated calculation of $g(x,y,z)$ using equation (1.32) for a given distribution of densities. The analytic difficulty comes in trying to approximate complicated geologic situations by geometric shapes where the shapes are sufficiently simple to compute the volume integral.

The magnetic field of a volume of magnetic material is given by

$$B = -C_m \nabla_P \int_R M \cdot \nabla_Q \frac{1}{r} dv \tag{1.33}$$

Where $\boldsymbol{M}$ is magnetization, and r is the distance from the observation point P to element dv is the body. The value of the constant $C_m$depends on the system of units. Most magnetic surveys measure the total-field anomaly or a single component of $\boldsymbol{B}$. The total-field anomaly is given approximately by

$$\Delta T = -C_m \hat{F} \cdot \nabla_P \int_R M \cdot \nabla_Q \frac{1}{r} dv \tag{1.34}$$

Where $\widehat{\boldsymbol{F}}$ is a unit vector in the direction of the regional field. Algorithms that implement equation (1.34) in order to calculate a component of $\boldsymbol{B}$ or the total-field anomaly, given a body's shape and distribution of magnetization, can be used for the forward method.

1.2.4.2. Inverse method

In the inverse method source parameters are determined directly from gravity or magnetic measurements. All three equations of vertical attraction of gravity, vertical magnetic field and total field anomaly have the same general form

$$f(P) = \int_R s(Q)\psi(P,Q)dv \tag{1.35}$$

where $f(P)$ is the potential field at *P*, *R* is the distance from point *P* to element dv, $s(Q)$ describes the physical quantity (density or magnetization) at *Q*, and $\psi(P,Q)$ is a function that depends on the geometric placement of observation point P and source point Q. Equation (1.35) is known as a Fredholm equation of the first kind (Morse and Feshbach, 1953). The inverse method inserts measurements of $f(P)$ directly into the left side of equation (1.35) and solves for some aspect of $s(Q)$ or *R*. Calculation of $s(Q)$ is known as the linear inverse problem, whereas calculation of some property of R is the nonlinear inverse problem.

Linear inverse problem

From equation (1.35), magnetic or gravity fields are linearly dependent on magnetization or density, and estimation of magnetization or density from magnetic or gravity fields is a linear inverse problem. Estimation of a single best density for a given mass is a simple example. If the shape of the body with uniform density is known, the integral term in this equation could be calculated by one of the forward techniques of Chapter 9 (Blakely, 1996). The gravity anomaly measured at *N* discrete locations is then

$$g_i = \rho\psi_i \qquad i = 1,2,\ldots,N, \tag{1.36}$$

and the constant ρ could be determined by simple linear regression. Ishihara, 1989, and Plouff, 1976, discuss this type of calculation in detail. We could complicate this procedure by dividing the body into smaller compartments and use least-squares methods to solve for the density of each compartment.

Nonlinear inverse problem

The potential field on the left side of the general form equation (1.35) is a linear function of the distribution of mass or magnetic material. Doubling the intensity of magnetization, for example, doubles the amplitude of the total-field anomaly, whereas tripling the magnetization would triple the amplitude of the anomaly. In general terms, a system is said to be linear if it satisfies the following test: If $f_1(P)$ is the field caused by source distribution $s_1(Q)$, and $f_2(P)$ is the field caused by another distribution $s_2(Q)$, then the field caused by $as_1(Q) + bs_2(Q)$ is simply $af_1(P) + bf_2(P)$, where a and b are constants. The same cannot be said for other parameters that define the source. The potential field is not a linear function of e.g., depth, thickness, or shape of the source. All these parameters are contained within $\psi(P,Q)$ and in the limits of integration implied by volume R in equation (1.35). Inverse methods that attempt to estimate these nonlinear parameters are called nonlinear methods, but in fact, many nonlinear methods entail simplifying assumptions that in effect render the problem linear.

1.2.4.3. Transformations

Potential field transformations are methods that facilitate geologic interpretations by transforming measured data into some new form. The ones applied in this work were only the upward and downward continuation, and the reduction to pole.

Upward and downward continuation

Upward continuation transforms the potential field measured on one surface to the field that would be measured on another surface farther from all sources. This transformation attenuates anomalies with respect to wavelength, i.e., the shorter the wavelength, the greater the attenuation. It is sometimes necessary to compare or merge surveys measured at different altitudes, providing a way to transform individual surveys onto a consistent surface. Upward continuation tends to accentuate anomalies caused by deep sources at the expense of anomalies caused by shallow sources.

Green's third identity shows why upward continuation should be possible. If function U is harmonic and continuous, and has continuous derivatives throughout a regular region R, then it follows from Green's third identity that the value of U at any point P within R is given by equation

$$U(P) = \frac{1}{4\pi}\int_R \left[\frac{1}{\mathrm{r}}\frac{\partial \mathrm{U}}{\partial \mathrm{n}} - U\frac{\partial}{\partial \mathrm{n}}\frac{1}{\mathrm{r}}\right] dS \tag{1.37}$$

where S denotes the boundary of R, n the outward normal direction, and r the distance from P to the point of integration on S. This illustrates the essential principle of upward continuation: a potential field can be calculated at any point within a region from the behavior of the field on a surface enclosing the region.

Downward continuation is the calculation of $U(x, y, z_0)$ from $U(x, y, z_0 - \Delta z)$, the inverse of the upward continuation integral. It is an "unsmoothing" operation, and such calculations are unstable. Small changes to $U(x, y, z_0 - \Delta z)$ can cause large and unrealistic variations in the calculated $U(x, y, z_0)$. This problem is demonstrated by writing the inverse of the equation for the Fourier convolution theorem

$$F[U] = F[U_u]F^{-1}[\psi_u] = F[U_u]e^{+|k|\Delta z} \tag{1.38}$$

In this case, $F[U_u]$ is the Fourier transform of the observed field, and $F[U]$ is the desired field continued downward by a distance Δz. Clearly the shortest wavelengths of the measured data will be greatly amplified by this procedure to a degree that depends on the value of Δz and the sample interval of the data.

Reduction to the pole

Reduction to pole (RTP) is a type of phase transformation. The phase transformations are filtering operations that transform a total field anomaly with given directions of magnetization and ambient field into a new anomaly caused by the same distribution of magnetization but with new vector directions, using Fourier transformations. Reduction to the pole removes one level of complexity from the interpretive process: it shifts anomalies laterally to be located over their respective sources and modifies their shape so that symmetrical sources cause symmetrical anomalies. In general terms, if the magnetization and ambient field are not vertical, a symmetrical distribution of magnetization (such as a uniformly magnetized sphere) will produce a "skewed" rather than a symmetrical magnetic anomaly. This added complexity can be partly eliminated from a magnetic survey by using equations for a filtering operation. The transformed anomaly in the Fourier domain is given by

$$F[\Delta T_t] = F[\psi_r]F[\Delta T] \tag{1.39}$$

Where

$$F[\psi_r] = \frac{1}{\Theta_m \Theta_f} \tag{1.40}$$

and,

$$\Theta_m = \hat{m}_z + i\frac{\hat{m}_x k_x + \hat{m}_y k_y}{|k|} \tag{1.41}$$

$$\Theta_f = \hat{f}_z + i\frac{\hat{f}_x k_x + \hat{f}_y k_y}{|k|}$$

With $\hat{m} = (\hat{m}_x, \hat{m}_y, \hat{m}_z)$ and $\hat{f} = (\hat{f}_x, \hat{f}_y, \hat{f}_z)$ being unit vectors in the direction of the magnetization and ambient field, respectively. The application of $F[\psi_r]$ is called reduction to the pole (Baranov and Naudy, 1964) because ΔT_r is the anomaly that would be measured at the north magnetic pole, where induced magnetization and ambient field both would be directed vertically down. Is important to highlight that RTP operations consider that remnant magnetization is too small compared to the induced magnetization, therefore is not considered in the calculations.

2. Geological and geophysical setting

2.1. Geological setting and geomorphology

Our site of study, the Monchique Alkaline Complex (MAC), is located close to the Portuguese Atlantic margin, west of Iberia. The MAC intrudes the Paleozoic South Potuguese Zone and belongs to the longest and most widespread magmatic event of Mesozoic ages in the region. The Atlantic Margin of Iberia encompasses three different tectonic sectors, the West Iberia Margin (WIM), the North Iberia Margin (NIM) and the SW Iberia Margin (SWIM) that formed as a result of rifting and seafloor spreading of the North Atlantic Ocean, Bay of Biscay and Western Tethys Ocean, respectively. Iberia shows widespread evidence of the Alpine orogeny both in the Paleozoic basement and in the Mesozoic rift basins, as well as major intra-oceanic compressional tectonic structures, mostly of Cenozoic age structures (Terrinha et al., 2020, 2019). Present-day active subduction in the SWIM (in relation with subducted slab beneath the Gibraltar Arc) is still a matter of discussion (Gutscher et al., 2002; Terrinha et al., 2020; Zitellini et al., 2009). Large-magnitude earthquakes and tsunamis originating near the Eurasia–Africa plate boundary have struck in the past (1755 and 1969) and thus constitute a major societal concern (Terrinha et al., 2020).

During the Mesozoic, the sectors of the Iberian Atlantic margin acted as spreading zones and, in the Cenozoic, as subduction and suture zones, giving rise to the Pyrenees and the Betic Chain. The N-S direction of the West Iberian Margin is parallel to the magnetic anomalies that characterize the ocean floor further offshore in oceanic domain (Valadares, 2004).

After the development of the Mesozoic basins and oceans, several compressive episodes took place that caused the uplifting of these basins. In the West Iberian Margin, the major compressive event is supposed to have occurred in the Miocene, being associated with the deformation that originated the Betic Chain. On the other hand, the tectonic inversion on the Algarve Basin is older, and could have started in the Upper Cretaceous/ Paleogenic (Valadares, 2004).

In mainland Portugal, the Iberian massif is composed of four major blocks with different characteristics and provenances, from NE to SW: the Galicia-Trás-os-Montes zone (GTMZ), the Central Iberian zone (CIZ), the Ossa-Morena zone (OMZ) and the South Portuguese zone (SPZ) (Custódio et al., 2015; Fernández et al., 2004; Lotze, 1950; McKerrow, 2000; Pinheiro, 1996; Quesada, 1991; Ribeiro, 1979; Simancas et al., 2001, 2003; Tait et al., 1997). The northernmost block, the GTMZ, is an exotic terrain of allochthonous unit that exhibits some high-pressure rocks and metamorphism, including ophiolitic rocks. To its south, the CIZ is thought to have belonged to Gondwana and is composed of metamorphosed Precambrian and Paleozoic rocks, intruded by large volumes of granitoids. The OMZ lays south of the CIZ and is also composed mostly of Precambrian to early Paleozoic rocks, namely metamorphosed sediments, and volcanic and plutonic rocks. The suture zone between the CIZ and the OMZ presents highly deformed and metamorphosed rocks, as well as some mafic rocks. The southernmost unit, the SPZ, is thought to have belonged to Avalonia and is composed of Paleozoic rocks, mostly sediments that were folded and thrusted, affected by low grade metamorphism. The contact between the SPZ and OMZ is a region that displays oceanic rocks (ophiolites with metabasalts, metagabbros and ultrabasic rocks), potential remnants of an accretionary prism (metasediments) and turbiditic sediments interbedded with continental volcanic rocks (Custódio et al., 2015 and references therein)

2.1.1. The South Portuguese Zone (SPZ)

The SPZ, which hosts the MAC, can be simplified into four major geological domains or sectors (Oliveira et al., 1979; Valadares, 2004): the North Sector, the Pyrite Belt, the Cercal-Mira Sector and

the Southwest Sector. The SPZ (Figure 1.1) is constituted of different Devonian and Carbonic rocks, which have two different stratigraphic sequences, one of a more local character, in the western part, and another general one for the entire area (Clavijo and Valadares, 2003). The North sector comprises the Pulo do Lobo formation (Upper Devonian and perhaps older) and the Ferreira-Ficalho group (Upper Devonian-Inferior Carbonic?) (Valadares, 2004). The Pyrite Belt is composed by the Phylite-Quartzitic formation (Upper Famennian) terrigenous sequence, and by the volcanic-sedimentary complex (Upper Devonian and Tournasian-Upper Visean) (Valadares, 2004). Cercal-Mira sector is a volcanic-sedimentary complex (Upper Devonian-Tournasian?); this is considered a lateral equivalent of the same unit of the Pyrite Belt (Valadares, 2004). The Southwest Sector is formed by the Tercenas Formation (Upper Devonian), a rhythmic alternation of gray shales, siltstones and Bioturbed sandstones; the Carrapateira Group, with the Bordalete, Murração and Quebradas Formations (Valadares, 2004).

The more general sequence is composed by different formations of the Baixo Alentejo Flysh Group (GFBA) (Clavijo and Valadares, 2003; Oliveira et al., 1979). It is a group of schists and greywackes in turbidite sequence, of Lower to Medium Carbonic (Westphalian) age, and of varisco syn-orogenic character (Clavijo and Valadares, 2003; Oliveira, 1990, 1983). The formations of Mértola (Upper Viseano), Mira (Namurian) and Brejeira (Middle Namurian-Upper Westphalian) belong to this group (Valadares, 2004). Variscan deformation manifests itself mainly through tectonic loading, with a southwestern verge in this area (Clavijo and Valadares, 2003; Silva et al., 1990). The material that constitutes the Algarve Basin is deposited in angular unconformity with the bedrock. The Mesozoic deposits in it are predominantly limestone, ranging in age from the Early Triassic to the Early Cretaceous. The Monchique massif intrudes in this sequence and dates from the Late Cretaceous, 72±4 Ma (Grange et al., 2010; Miranda et al., 2009).

2.1.2. Algarve Basin

The Algarve basin formed as a rift basin on a transtensional rifted margin, from Triassic through Early Cretaceous times. The Mesozoic sedimentary sequences lie unconformably on top of a Paleozoic thrust belt that consists mainly of Carboniferous low-grade metamorphosed flysch deposits deformed in the foreland of the Variscan orogen. The Mesozoic stratigraphic record initiates with continental siliciclastic sequences, clay and evaporite deposits in Triassic-Hettangian times, followed mostly by marine carbonates and minor siliciclastic events during Jurassic and Cretaceous. Rifting occurred in four main pulses: during the Triassic-Early Jurassic, Middle Jurassic, Late Jurassic and Early Cretaceous. Important unconformities and hiatuses are found associated with the transition between consecutive rifting events, and transient compressive events also occurred between rifting episodes (Neres et al., 2018; Terrinha et al., 2002).

In Cenomanian times (~92 Ma) Africa started rotating anticlockwise, thus departing from the previous southeastwards directed movement with respect to Eurasia. Consequently, tectonic inversion of the south Iberia rifted margin occurred in various pulses from Late Cretaceous to Miocene times. Both thin and thick-skinned thrusts formed, either as inverted normal faults or as shortcut thrusts, usually with southwards directed tectonic transport direction (Neres et al., 2018; Ramos et al., 2017, 2016; Terrinha et al., 2002; P. A. G. Terrinha, 1998).

The closure of the western Tethys and back-arc basins of the west Mediterranean reached its peak in Mid-Late Miocene times. A remnant of the Tethyan oceanic slab remained attached between Iberia and Africa and its westwards directed roll-back dragged the Gibraltar arc, the Beltics and the Rif orogens to the west towards the Atlantic Ocean realm, closing the Mediterranean basin (Gutscher et al., 2002; Martínez-Loriente et al., 2014; Neres et al., 2018; Sallarès et al., 2011). In Pliocene times, the continuation of the anticlockwise rotation of Africa with respect to Iberia implied the change from

frontal to oblique collision causing the formation of a dextral transform plate boundary accommodated by the SWIM strike-slip faults; the northernmost of them lies adjacent to the Portimão and Guadalquivir Banks (Neres et al., 2018; Zitellini et al., 2009). At present, shortening in SW Iberia is accommodated offshore by northwestwards-directed thrusts along the southwest margin of Portugal and southwards-directed thrusts along the southern boundary of the Algarve Basin (Terrinha et al., 2009; Zitellini et al., 2009), causing the uplift of the SW part of Portugal (Neres et al., 2018).

2.1.3. The Monchique Alkaline Complex (MAC)

MAC is located in the Southwest of Portugal (Figure 1.1 and Figure 2.1). The igneous complex has been dated to the Late Cretaceous, 72 ± 4 Ma (Miranda et al., 2009) and 68.8 ± 1 Ma (Grange et al., 2010); and comprises multiple intrusions ranging from ultrabasic, basic and intermediate rocks to nepheline syenites, in addition to several brechoid formations. It outcrops in southern Portugal, along about 80 km^2, with a roughly elliptical pattern, with ENE-WSW orientation of its major axis (Valadares, 2004). The 72.3±4.2 Ma age appears to reflect the real intrusion age of the nepheline syenite magma. A similar age was obtained by adding two samples from the mafic intrusives suggesting a coeval emplacement and a genetic link between all units. The amphibole separate obtained from an ultrabasic lamprophyre in the Monchique complex defines a weighed mean plateau age of 74.4±2.0 Ma (Miranda et al., 2009)

The MAC intrudes in the Flysch deposits of the Brejeira formation of Baixo Alentejo Flysh group (GFBA) (Oliveira et al., 1979; Valadares, 2004) from Vestefalian. It constitutes a unique feature because it this type of massif normally intrudes in granitic and gneissic basement rocks (Rock, 1979; Valadares, 2004). It is one of the largest known bodies of nepheline syenites of miaschitic composition (Valadares, 2004). The MAC was installed in a post-rift context of the WIM, when oceanic spreading was already well established in the western and southern continental margins of Portugal, which resulted from the fracturing of Pangea and the separation of Iberia from the American and African continents.

The MAC comprises three main elevated areas, from west to east: Picos, Fóia and Picota. The main elevations of the massif are Fóia (902 m) and Picota (774 m). Both have rounded slopes with strong deepings, with an elongated NE-SW elliptical base. The MAC is traversed by a NE-SW linear depression between Fóia and Picota, where the Ribeira de Monchique is located, but it does not coincide with the geologic contact. The genesis of this depression is not very well understood, but it could be related to a fault, epigeny or advance of a river, fracture or simply with the initial geometry of the intrusion (Feio, 1951; Valadares, 2004).

Monchique is also a region affected by low temperature hydrothermalism. Hydrological analyzes show that the mineralization of water in the region is strongly related to the presence and fracturing of the MAC (Lourenço, 1998). The flow of water in depth enables the heating of waters that emerges with temperatures between 27º and 31.5º C (Lourenço, 1998).

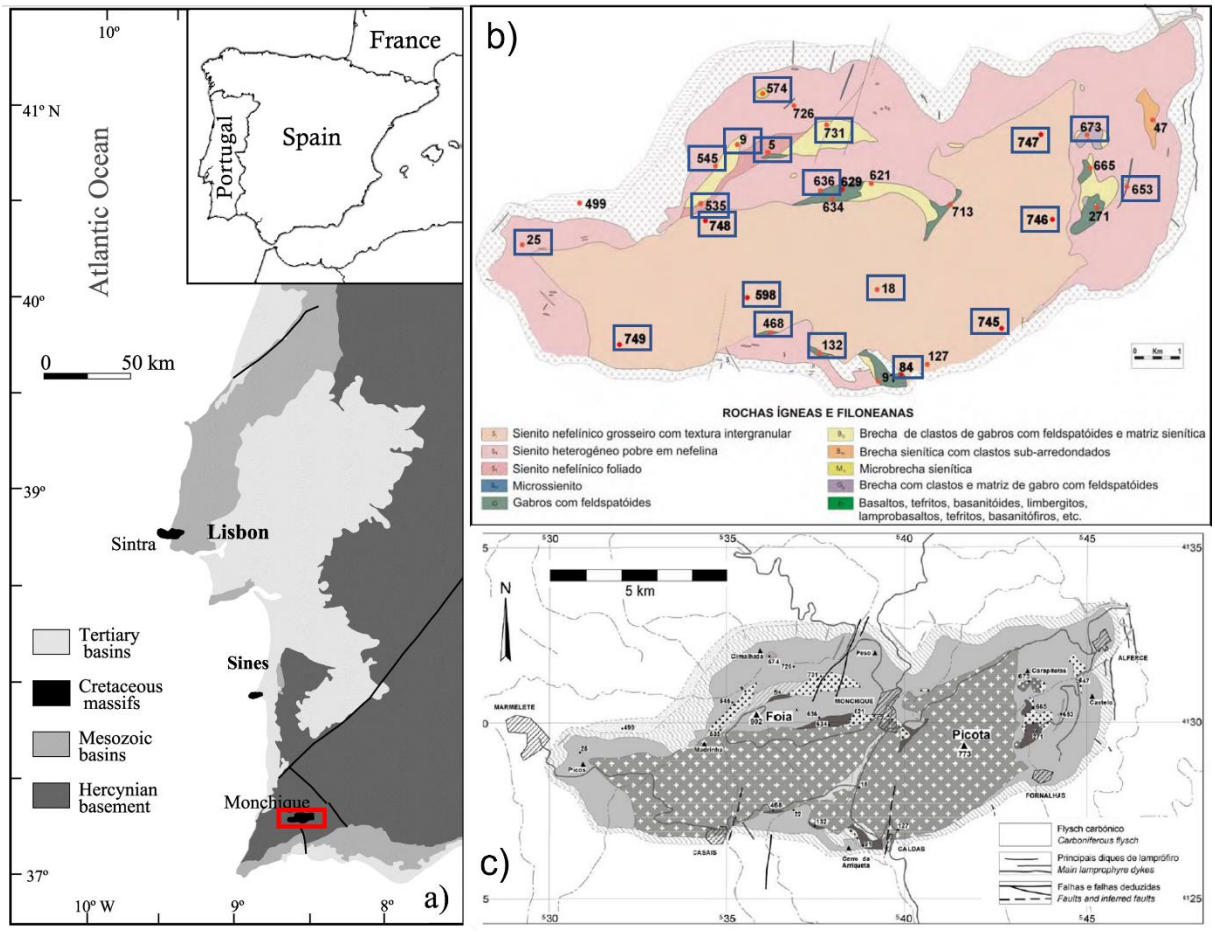

Figure 2.1 a) Simplified geological map of Portugal showing the main Late Cretaceous Alkaline massifs: Sine, Sintra and Monchique (modified from Ribeiro et al., 2013). b) Geological map of Monchique with the location of (Valadares, 2004) samples for the petrologic study; the samples marked as blues rectangles were the ones used in this work for density analysis (Modified from Valadares, 2004). c) Geological map of Monchique with scheme of Paleozoic structures of the hosting rock, and location of main elevated areas (Modified from Valadares, 2004).

According to Rodrigues et al. (2014), the MAC apatite analysis provided younger ages than those of the complex itself. These results support that uplift occurred immediately after the intrusion. Through their modeling results they conclude that after deposition, the GFBA (Baixo Alentejo Flysh Group) was subjected to maximum temperatures of 300-260ºC between 310 and 300 Ma. It was followed by gradual cooling up to temperatures between 90-120ºC between 210-200 Ma. Between 200 and 20 Ma, the temperature remained between 120 and 70ºC, showing a slight subsidence during and after the Triassic. From 20 Ma to the present, rapid cooling was observed from temperatures of 70-60°C to the surface temperature. Considering the ages of fission tracks obtained in the GFBA (between 157 and 59.9 Ma), these lithologies would already be at a temperature below 100ºC before or during the MAC intrusion. Considering a gradient of 30ºC/km, it is possible to infer that during the intrusion the host rock (Formação de Brejeira) was at ca. 2 km deep and would be under relatively cold temperature, a possibility already suggested by (Valadares, 2004). After cooling, and the temperature having reached equilibrium with the host rock, both are assumed to have had the same thermal history (Rodrigues et al., 2014).

2.1.4. Magmatic events on West Iberian Margin (WIM)

The onshore sector of the West Iberian Margin (WIM) was the locus of several cycles of magmatic activity during the Mesozoic. Occurrences related to the first two cycles display tholeiitic and transitional affinities (Martins, 1991; Martins et al., 2008) and ages around 200 Ma (e.g., Dunn et al.,

1998; Miranda et al., 2009; Verati et al., 2007) and 130–135 Ma (Ferreira and Macedo, 1979; Miranda et al., 2009), respectively. The third cycle occurred between 100-65 Ma displayed alkaline magma along the WIM.

The oldest magmatic event, 200 Ma, is present in the Algarve Basin in the form of tholeiitic basalts that belong to the Central Atlantic Magmatic Province that has been interpreted in relation with the first extensional phases of Pangea and opening of the Atlantic Ocean (Martins et al., 2008; Marzoli et al., 1999; Neres et al., 2018; Verati et al., 2007). The second event, 140–148 Ma, is restricted to small occurrences in a section of the Lusitanian Basin north of Lisbon. This second event has been attributed to melting of metasomatized lithosphere during rifting extension preceding the opening of the north Atlantic (Mata et al., 2015; Neres et al., 2018).

The third event is the longest, most widespread and remains the most intriguing. It consists of Cretaceous alkaline magmatism of sublithospheric origin that affected the West Iberia Margin from approximately 100 Ma to 65 Ma, both onshore and offshore. Due to the perfect N28°W alignment of the three onshore plutons (Sintra, Sines and Monchique), it has since long been suggested that the emplacement of the three onshore complexes was controlled by a deep-seated NNW-SSE striking fault . Merle et al. (2009) suggested that the distribution of Cretaceous magmatism results from a wide mantle plume or thermal anomaly that emitted scattered magmatic pulses during the complex motion of Iberia. Following the latter, Grange et al. (2010) justified the NNW-SSE trend and the southwards age decrease of the three main onshore plutons with a northward motion of the Iberian plate above a mantle plume. However, this plate motion is not supported by paleomagnetic data because there is no evidence for significant paleolatitude variation during this time interval (Gong et al., 2008; Neres et al., 2018, 2012). The largest occurrences of this cycle are the Mafra dike complex, Lisbon volcanic complex and the three subvolcanic massifs of Sintra, Sines and Monchique. There are also several bodies dispersed throughout the Lusitanian Basin, in the western Algarve and offshore (Pinheiro et al., 1996; Valadares, 2004).

Miranda et al. (2009) joined his age determinations with previously published data and constrained the Late Cretaceous alkaline cycle to circa 22 Ma and to define two distinct pulses of alkaline magmatic activity within the third cycle of magmatism. The first one (94–88 Ma) occurred during the opening of the Bay of Biscay and consequent rotation of Iberia (123–80 Ma; Sibuet et al., 2004) and clusters around the Lisbon area (above N38º 200) where it occurs mainly as sills (Foz da Fonte and Paço d'Ilhas). The second pulse lasted from 75 Ma to 72 Ma and occurred synchronous to the initial phase of the alpine orogeny and tectonic inversion of the Mesozoic basins that lead to the formation of the Pyrenees and Betic mountains, it corresponds to a more widespread event with scattered occurrences from the Algarve Basin in southernmost Portugal (37ºN) to the Lisbon area (N39º) and comprises both intrusive and extrusive complexes (Miranda et al., 2009; Neres et al., 2014)

The alkaline magmatic cycle, during the Late Cretaceous, was also responsible for the formation of several offshore seamounts along the Tore-Madeira Rise and some magmatic occurrences in the Gorringe Bank. The occurrence of simultaneously oceanic and continental magmatism suggests the presence of a regional mantle anomaly, that is, interaction between mantle plumes with sustained active upwelling at depth (Geldmacher et al., 2006; Merle et al., 2006; Soares, 2018).

The anomalously hot sub-lithospheric mantle required to explain the Late Cretaceous alkaline magmatism at the WIM could correspond to actively upwelling, deep anchored, mantle plumes interacting with mid-ocean ridges and other major structures invoked in order to explain the Late Cretaceous magmatism offshore of the WIM (104–65 Ma - (Geldmacher et al., 2006, 2000; Merle et al., 2006; Miranda et al., 2009). Alternatively, the existence of small passive convective diapiric instabilities in the upper mantle as suggested by several authors, either in continental or oceanic settings (e.g.,

(Granet et al., 1995; Lustrino and Wilson, 2007; Mata et al., 1998), could justify the genesis of the WIM alkaline magmatism and the existence of the widespread, long lived and yet relatively small volume Circum-Mediterranean Cenozoic Anorogenic igneous province (Miranda et al., 2009).

According to Neres et al. (2018), the alignment of the Guadalquivir-Portimão magnetic anomaly with the three onshore Upper Cretaceous alkaline magmatic intrusions (Sintra, Sines and Monchique, of sub-crustal origin) suggests that it could be assigned to the west Iberia Late Cretaceous alkaline magmatic province. The Guadalquivir- Portimão intrusion would thus constitute the fourth, southernmost and largest magmatic intrusion of this enigmatic and highly suggestive N28°W tectono-magmatic alignment, confirming previous hypotheses (Neres et al., 2018; Ribeiro, 1979; P. Terrinha, 1998). This theory is reinforced by the comparable amplitude (> 200 nT) of the magnetic anomaly of the Guadalquivir-Portimão intrusion with the other three. Although larger than each of the Sintra, Sines and Monchique alkaline intrusive complexes, the difference in size can be due to specific tectonic controls or magma availability (Neres et al., 2018).

2.1.4.1. Previous studies of the Monchique Alkaline Complex magnetic properties

The anisotropy of magnetic susceptibility (AMS) designates the dependence of magnetic susceptibility on the direction along which it is measured. It is mathematically described by a second-order symmetric tensor - magnetic susceptibility tensor - and represented by a triaxial susceptibility ellipsoid defined by its three principal orthogonal axes (k_1, k_2, k_3) and the bulk susceptibility k is the arithmetic mean of the axes (Barbosa, 1999). It translates the preferential orientation of the magnetic minerals in the magnetic fabric; being the longer axis the lineation, and the smaller axis the foliation of the mineral. The main magnetic signal enhancers are generally iron oxides, particularly magnetite and hematite. Magnetite (Fe_3O_4) has a ferrimagnetic structure, and a cubic crystal structure. Magnetite's magnetic susceptibility is very high compared to other magnetic minerals. Hematite has an antiferromagnetic structure and therefore very little magnetization, with susceptibility values less than 1% of magnetite (Barbosa, 1999). Thus, magnetite (or titanomagnetite) largely dominates the magnetic signal when present.

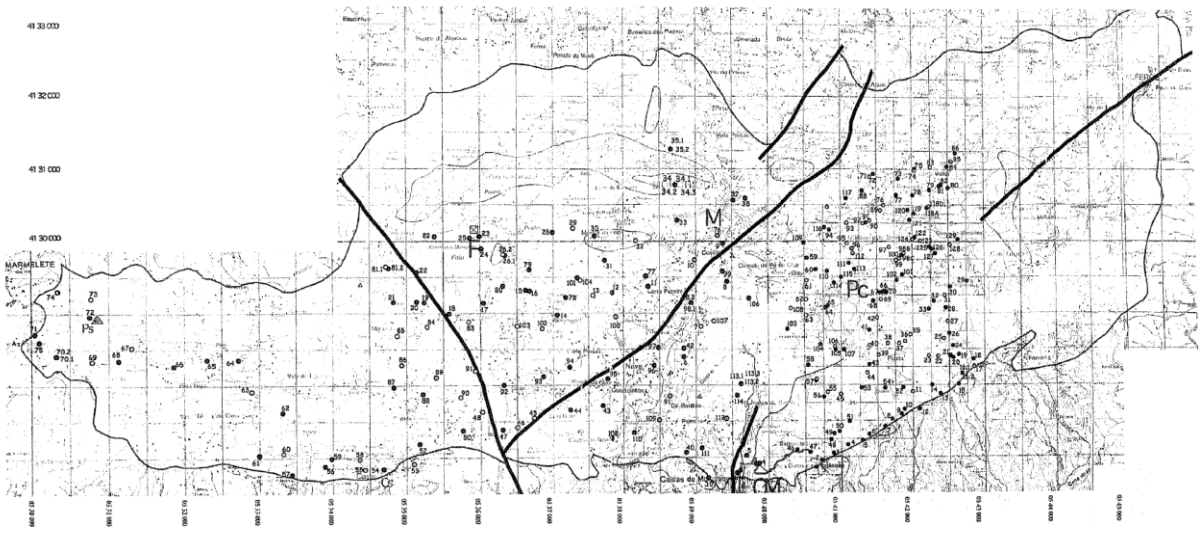

Figure 2.2 Sampling from Barbosa (1999).

Barbosa (1999) performed a rock sampling (Figure 2.2) over the massif, in two groups defined by geographic location. In the Foia group, the average susceptibility data are not uniformly distributed and are divided into the Picos, Foia-W and Foia-E regions according to their longitudes. In the Picota group the lowest k values are located near the peak of Picota and near the southeast contact. The variability of

magnetic susceptibility along the massif reflects the variability in magnetization of rocks (assuming that the geomagnetic field is uniform, which is reasonable in this geographical context). The magnetization of a rock has multiple origins: they depend on the composition and size of the grains, the magnetic minerals that make them up and their geological history. In principle differences in altitude correspond to different cooling speeds of the magmatic fluid, although with several lithologies this relation is more complex. In regions of intrusive mass where the cooling of the magma is slower, rocks have well-developed crystals and multidomain grains. On the contrary, where cooling is more sudden, the structure of the rocks is more amorphous, and the magnetic grains are essentially pseudo-monodomains and monodomains. In Monchique there is no explicit correlation between the average susceptibility values and the relief of the massif (Barbosa, 1999).

The average value of magnetic susceptibility of the Picota block ($2.7057x10^2$) is higher than that of the Foia block ($2.1529x10^2$). The maximum, mimimum, and standard deviation for Foia are $6.128x10^2$, $0.0046x10^2$, $1.0815x10^2$ respectively; and for Picota minimum of $0.0687x10^2$, maximum of $9.78x10^2$, standard deviation of $1.3218x10^2$(Barbosa, 1999).

The magma's ascent would have been quick, given that the metamorphic contact zone is well delimited and very steep. Assuming that the two blocks resulting from two different pulsations of the same magma, Barbosa (1999) suggested that Picota will be the most recent block, and with slower cooling. Picota would have risen when the material from the Foia block had not cooled yet, but it already had a high viscosity as indicated by the existence of the tectonic depression to the west of Picota. AMS results for Picota suggest that the block may have risen wedged to the west by Foia, and by previous metasedimentary formations to the southwest and southeast. As for Foia, the spatial correlation of susceptibility revealed a marked anisotropy and indicates compression and confinement of the intrusion by the two extremes (peaks and the fault separating the two Blocks) during its formation (Barbosa, 1999).

2.1.5. Petrology of the Monchique Alkaline Complex magnetic

The study of the MAC, by Valadares (2004), allowed the identification of two distinct syenite facies and the mapping of a typical cartographic pattern of zoned intrusions. The nuclear nepheline syenitic unit outcrops, in the center of the intrusive complex and is characterized by being quite homogeneous throughout its extension and generally presenting an intergranular texture, good development of alkali feldspar crystals and nepheline present in appreciable amounts. The boundary heterogeneous syenite unit surrounds the previous unit in almost the whole massif, and its heterogeneity is reflected in its facies and mineralogical composition. This unit has different contents of mafic minerals, and variations in the nepheline content. Another important feature of this unit is the presence of corneal enclaves and basic rocks in its interior; in the homogeneous unit of nepheline syenite small basic rock xenoliths are found sporadically.

Nepheline syenites are rocks with a phaneritic, granular, hypoidiomorphic texture, of medium to coarse grain, containing alkali feldspar, nepheline and sometimes sodalite as essential phases. The heterogeneous syenites is constituted by rocks of phaneritic, hypoidiomorphic and heterogranular texture with potassic ± nepheline feldspar as the main paragenetic association. The rocks that make up this second unit show a great heterogeneity in mineralogical terms. In the intrusive complex, in addition to the central and peripheral nepheline syenites, there are also eight basic rock bodies. Of these, five outcrop in the contact between the two syenitic units and the rest are present inside the boundary syenitic unit, close to the contact with the nuclear nepheline syenite unit. Each body of these rocks is characterized by a heterogeneity that manifests itself in its own lithology and granularity. The MAC

intrusion also generated in the enclosing materials an aureole of contact metamorphism, which has a width of about 200m (Valadares, 2004).

The ultramafic rocks identified by Valadares (2004) are predominantly constituted by ferromagnesian minerals and were classified as ijolites or lamprophyric rocks. The ijolite is characterized by its phaneritic, heterogranular and hypoidiomorphic texture with pyroxene, biotite, sphene, apatite and opaque crystals included in nephelines and feldspars. Lamprophyric rocks have reduced proportions of nepheline and feldspars and high content of titanium-rich ferromagnesian minerals and have a porphyroid character with fine-matrixed amphibole and pyroxene phenocrysts. Mafic and intermediate rocks are characterized by the systematic absence of olivine and have compositions ranging from nepheline gabbros (teralites), monzogabros and nepheline monzodiorites with titaniferous and titaniferous amphibole (essexites) and melanocratic nepheline syenites (malignites, intermediate rock). They correspond to teralites and/or essexites and exhibit strongly inequigranular phaneritic hypoidiomorphic textures (Valadares, 2004).

2.1.6. Geochemistry

The MAC is considered a pneumatolytic hydrothermal intrusion, an intermediate state of crystallization of low viscosity magma with a high concentration of water and silicon dioxide, which is still active (Lourenço, 1998; Lourenço and Cruz, 2005; Soares, 2018; Veludo et al., 2017).

Valadares (2004) analyzed mafic rocks from Monchique in order to study rocks from various outcropping bodies and with distinct field characteristics which, as it turned out, correspond to different evolutionary stages of the magmatic series. In general terms, the Monchique rocks seem to define coherent evolutionary trends, marked by a progressive enrichment in Na_2O, K_2O and Al_2O_3 and depletion in CaO, TiO2, Fe2O3t, MgO, MnO and P2O5, from the less differentiated terms to the more evolved ones. The presence of a reasonably continuous spectrum of compositions, as well as the strong correlations observed between silica and the remaining oxides, suggest that the felsic rocks may have derived from the basic magmas associated by fractional crystallization processes in a closed system (Valadares, 2004). The increase in Al2O3, Na2O and K2O with the degree of differentiation suggests that there was no notable fractionation of plagioclase, nepheline, sodalite and orthosis during the evolution of these magmas, or that their separation wasn´t enough to produce their impoverishment in the successive residual liquids (Valadares, 2004). It should also be noted that their multi-elementary profiles of the less evolved members (trace elements) are very similar to those of OIB basalts and that the Zr/Nb ratios obtained in these rocks fall within the range of values defined for oceanic island basalts (< 10), pointing to a derivation a from the same type of source reservoirs.

Grange et al. (2010) analyzed the most primitive rocks for each alkaline massif of Portugal, Sintra, Sines and Monchique in order to infer the sources of magma related to them, because these rocks appear to have undergone the least amount of crystal fractionation. The Sines and Sintra massif have similar concentrations Pb isotopes (negative Pb anomaly) and low to moderate Sr initial signature and are consistent with a derivation from a mantle source slightly depleted than the source of mid-ocean ridge basalt (MORB), and do not suggest contamination by upper continental crust. They conclude that the igneous rocks from Sintra and Sines can be explained by a large contribution of the subcontinental lithospheric mantle (SCLM) in the source of these rocks.

The most primitive rock from Monchique presents a high PB anomaly and highest Sr initial signature, within the range of MORB and the Tore seamounts (Merle et al., 2006). Bernard-Griffiths et al. (1997) identified the source for the Monchique and Ormonde massifs as a sub-lithospheric deep mantle source (ocean island basalt -type source). Therefore, the enriched DMM (depleted MORB mantle)-like component that Grange et al. (2010) identify in the source of the Monchique rocks could either be a

mantle plume with an enriched DMM signature or the ambient sub-lithospheric mantle (asthenosphere) enriched by a deep mantle plume.

This changes in components of magma sources in the Portuguese Alkaline massifs indicates a pathway of the deep magmas toward the surface that become better developed through time, reducing the contamination by the SCLM. From Sintra and Sines to Monchique, the isotopic signatures of the rocks change towards compositions closer to the sub-lithospheric component. These variations are induced by the northward motion of the Iberian plate, resulting in the southward migration of the alkaline magmatism (Grange et al., 2010).

2.1.7. Seismicity

Western Iberia, in the southwestern edge of the European continent, is a region of slow lithospheric deformation that lies directly north of the boundary between the Eurasian and Nubian plates. Locally, the two plates converge obliquely at a low rate of 2–5 mm yr^{-1} (Custódio et al., 2015; Fernandes et al., 2007; Neres et al., 2016; Nocquet, 2012; Serpelloni et al., 2007). Nevertheless, throughout history Portugal has been repeatedly affected by notably large and damaging earthquakes, nucleated both onshore and offshore. These include the largest earthquake in the European historical record, the 1755 Geart Lisbon Earthquake (Custódio et al., 2015).

Based on GNSS and focal mechanism observations, Serpelloni et al. (2007) identified the region offshore SW Iberia as one of the compressive belts that currently accommodates the convergence between Nubia and Eurasia. Several faults showing evidence of Cenozoic activity have been identified S and SW of Iberia (Custódio et al., 2015; Duarte et al., 2013; Gutscher et al., 2009; Terrinha et al., 2009, 2003; Zitellini et al., 2009), which together with disperse earthquake locations have led to the classification of this region as a diffuse plate boundary (Custódio et al., 2015; Neres et al., 2016; Sartori et al., 1994).

Monchique is dominated by low magnitude earthquakes (M < 4), which is not clearly justified when considering geologically mapped active faults (Soares, 2018). The concentration of instrumental earthquake epicenters located in the MAC area is a factor that increases the interest in this area, as it may imply seismic activity in structures related to the MAC installation (Valadares, 2004).

Custódio et al. (2015) finds that earthquakes in this region do not occur on a border characterized by a single long fault. Movement at the plate boundary is accommodated by segmented faults that are distributed along the boundary (Custódio et al., 2015; Sartori et al., 1994). It is possible to distinguish two privileged lines or directions of occurrence of earthquakes: one oriented NNE-SSW and the other E-W (Custódio et al., 2015). Soares (2018) also verifies the existence of a cluster of epicenters over the MAC with a lineation of NNE-SSW and another E-W epicenters; and depth cuts as a function of latitude and longitude show that almost all hypocenters are above 20 km and that there is a latitudinal concentration between 37.2º and 37.4º. Although this cluster represents a very small area, it is the most active seismic cluster in Portugal.

Both onshore and offshore, clusters and lineations of epicentres are preferentially oriented NNE–SSW and WNW–ESE (Custódio et al., 2015). GPS data indicates that WIberia is undergoing oblique convergence, oriented NW-SE to WNW–ESE, with respect to Nubia (Custódio et al., 2015; Fernandes et al., 2007; Neres et al., 2016; Nocquet, 2012; Serpelloni et al., 2007). According to available focal mechanisms this convergence is accommodated by a mix of strike-slip and reverse earthquakes (e.g. (Borges et al., 2001; Custódio et al., 2015; Domingues et al., 2013; Stich et al., 2010, 2003). It is plausible that NNE–SSW lineations, which are perpendicular to plate convergence, accommodate mostly reverse faulting and that WNW–ESE lineations, parallel to plate convergence, accommodate

mostly strike-slip faulting (Custódio et al., 2015). Jointly, the two types of lineations would account for the transpressive plate boundary deformation (Custódio et al., 2015).

In the longitudinal section of Monchique, a more dispersed accumulation of hypocenters is observed, with an NNE-SSW direction approximately and also perpendicular to this direction, between -8.7 and -8.4 degrees (Soares, 2018). Most of the seismic hypocenters in the region are located between 5 km and 20 km, which indicates that the lithosphere of this location has a fragile behavior until the base of the crust, which in Monchique is estimated as 31 km based on teleseismic P-wave functions (Dündar et al., 2016; Soares, 2018). The fact that a large number of earthquakes is observed between the surface and 20 km, with an intensification between 10 and 20 km, leads to a characterization of "brittle" crust up to 25 km if it is constituted by hydrated feldspar.

2.1.8. Seismic Tomography

In the Monchique massif, at the surface, the observed seismic cluster is not evidently associated with any kind of alignments or long fault systems. From Pliocene ages to the present day, geomorphological observations display an uplift of 300-350 m, with paleoseismites justifying intense seismic vibration and sedimentary liquefaction and fluidized material in the Quaternary (Dias and Cabral, 2002; Veludo et al., 2017).

The Monchique massif presents a strong signature in the tomographic models and a high seismicity rate cluster, centered on the massif. Veludo et al. (2017) profiles across the massif show: in the upper 5 km, a high-Vp anomaly, temptatively related to the presence of the main syenitic body of the massif, lying above a low-Vp anomaly where the majority of the earthquakes are located (Veludo et al., 2017), probably related to the hydrothemalism and/or a fracture zone. To the SW of the massif, there is evidence of significant anomalies in the Vp and Vp/Vs ratios (Dündar et al., 2016; el Moudnib et al., 2015; González et al., 1996; González-Fernández et al., 2001; Matias, 1996; Rocha et al., 2010; Salah, 2014; Veludo et al., 2017).

3. Data and methods

3.1. Gravity data

For the gravimetric analysis of the Monchique intrusion, we used two sets of gravimetric data preexistent from other projects/databases. The principal dataset used in the gravimetric analysis of Monchique comes from the gravity campaign performed from 21 to 25 of February 2019 in the framework of the SPIDER project. Two gravimeters were used: a SCINTREX CG3-M and a LaCoste & Romberg G-664, and measurements were conducted for 49 points in the Monchique area (Figure 3.1). The GPS observations were performed in Real-Time Kinematic mode using the reference stations of the Portuguese CORS network (ReNEP). The absolute gravity values were measured before and after the campaign in Sines and Santa Clara for calibration. The other set of data is from IGP (Instituto Geográfico Português, https://snig.dgterritorio.gov.pt/) collected in April 1997. The data contain the free-air anomalies adjusted to the IGSN-71 (International Gravity Standardization Net 1971). For this work we only used 276 data points of these records, the ones surrounding the Monchique area (Figure 3.1).

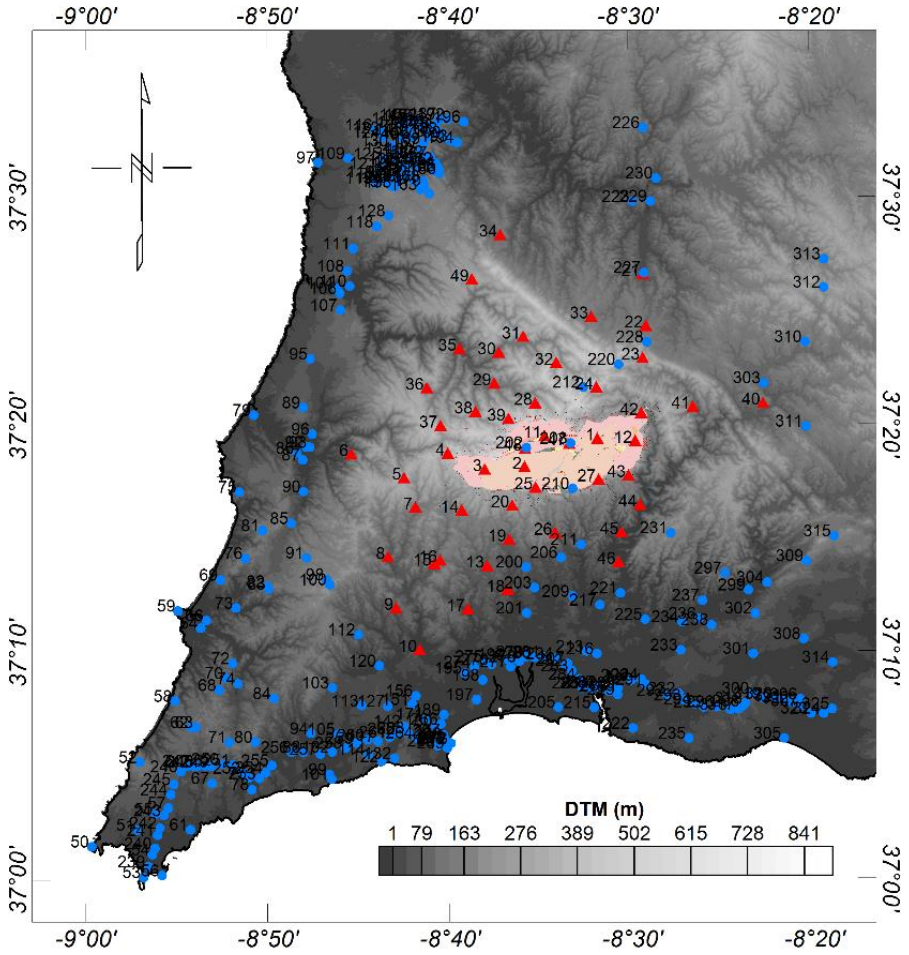

Figure 3.1 Map with the location of gravity measurements with the Monchique intrusion geological map. The red triangles are the points of the SPIDER project, and the blue circles the points from IGP data.

3.2. Magnetic data

Magnetic data were collected in the framework of ATLAS project during two campaigns in August of 2020 and in May of 2021, using a triaxial magnetometer SENSYS MagDrone R3 attached to a drone. The sensibility of the magnetometer is around 0.15 nT for all three axes, however, due to calibration errors in the scale and non-orthogonality of the sensors, the real accuracy is around 5-10 nT. On the

first campaign the drone was flying at 30 m above terrain following the topography, and on the last campaign the altitude was constant 30 m, not following the terrain. The drone paths above Monchique hill can be seen in Figure 3.2a.

A magnetic set of data from Socias and Mezcua (2002) magnetic anomaly map of Iberian Peninsula was also used. This map is a compilation of the aeromagnetic data collected for Portugal in 1980 (Miranda et al 1989) and Spain 1987. In Portugal data were collected with a proton's magnetometer (Geometrics G803) and in Spain with a double nuclear resonance, Overhauser effect, with a sensitivity of 0.01nT. This data was acquired at an altitude of 3000 m with spatial resolution (line spacing) of 4000 m. For this work we cut the total grid data to contain only the surroundings of Monchique and SW Portugal (Figure 3.2b).

The remaining processing of the magnetic and gravimetric data, explained in the processing section of this work, was carried out using the Oasis Montaj software (Seequent). The inverse 3D models for the gravimetric and magnetic data were made using the VOXI Earth Modeling extension for the geophysical inversion and the 2D forward modeling was performed with GM-SYS modeling application of Oasis Montaj.

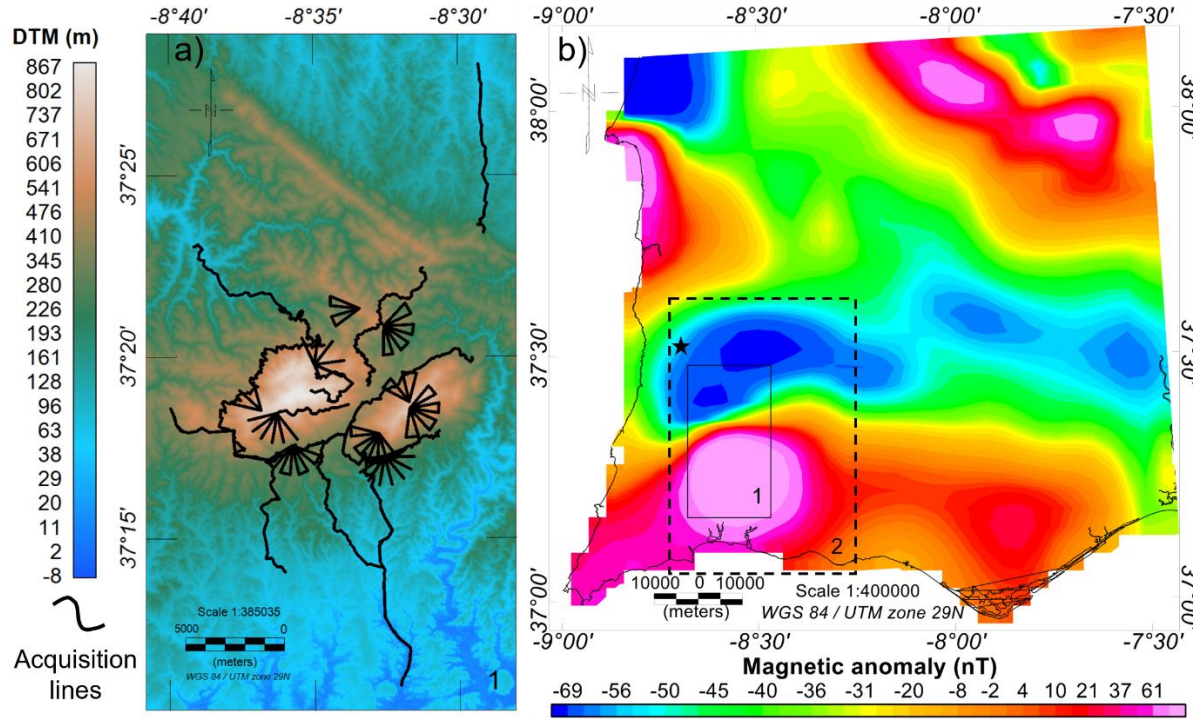

Figure 3.2 Raw magnetic data of Monchique. a) Acquisition lines with drone in ATLAS project campaigns. b) Aeromagnetic anomaly map cut from (Socias and Mezcua, 2002) magnetic anomaly map of Iberian Peninsula; Portugal area corresponds to (Miranda et al., 1989); Area 1 (full black rectangle): location of map shown in a); Area 2 (dashed black rectangle): location of map for ATLAS sample's location in Figure 3.3. The black star indicates the location of the São Teotónio magnetic base station.

3.3. Density analysis

The rock samples used in the density analyses came from two different sets. The first one focused on the intrusion itself, was collected by the researcher Vasco Valadares in 2004 and gently provided for this study. The second set of rocks was collected in the scope of ATLAS project, in March 2021, for this study. Figure 2.1 and Figure 3.3 shows the location of the samples from Valadares (2004) and from this study, respectively. In the ATLAS sample campaign, we mainly collected samples at outcrops on the side of roads. These rock samples were more weathered, because they were collected from exposed

rocks (although fresher samples were always chosen), while V. Valadares samples were collected from fresher rocks.

A total of 73 samples were analyzed, 50 from ATLAS and 23 from V. Valadares. For the magmatic intrusion we sampled gabbros (5), syenites (18) and breccia (5); and for the surroundings slate (14), graywacke (22), hornfels (1), shales (2) and quartz (4). The ATLAS sample campaign also collected some rocks from syenites. Examples of the rock types can be seen in Figure 3.3.

The density measurement was performed in the Petrology Laboratory of the Geology department of the University of Lisbon. First the mass of the sample is measured through a nylon line attached to a hook connected to the balance, it will give us the dry mass of the sample, m_d. The nylon tied in the rock is supposed to not influence the measured mass. Then this same sample is put under water to measure the apparent mass of the sample. This apparent mass , m_a, will give us the apparent weight, $P_a = (m_a * g)$. Then, we can calculate the buoyancy force, F_b:

$$F_b = P - P_a \tag{3.1}$$

Where $P = (m_d * g)$. The volume of the rock is calculated through the formula of the buoyancy force:

$$F_b = \rho_f * V_f * g \tag{3.2}$$

Where ρ_f is the density of the fluid, V_f is the volume of fluid dislocated in the recipient which will be the same as the rock volume, and g is the gravity acceleration (9.8 m/s^2). The fluid used was water, approximated density of 997 Kg/m^3. After the volume calculation of the rock sample, the density, ρ , is given by:

$$\rho = m_d/V \tag{3.3}$$

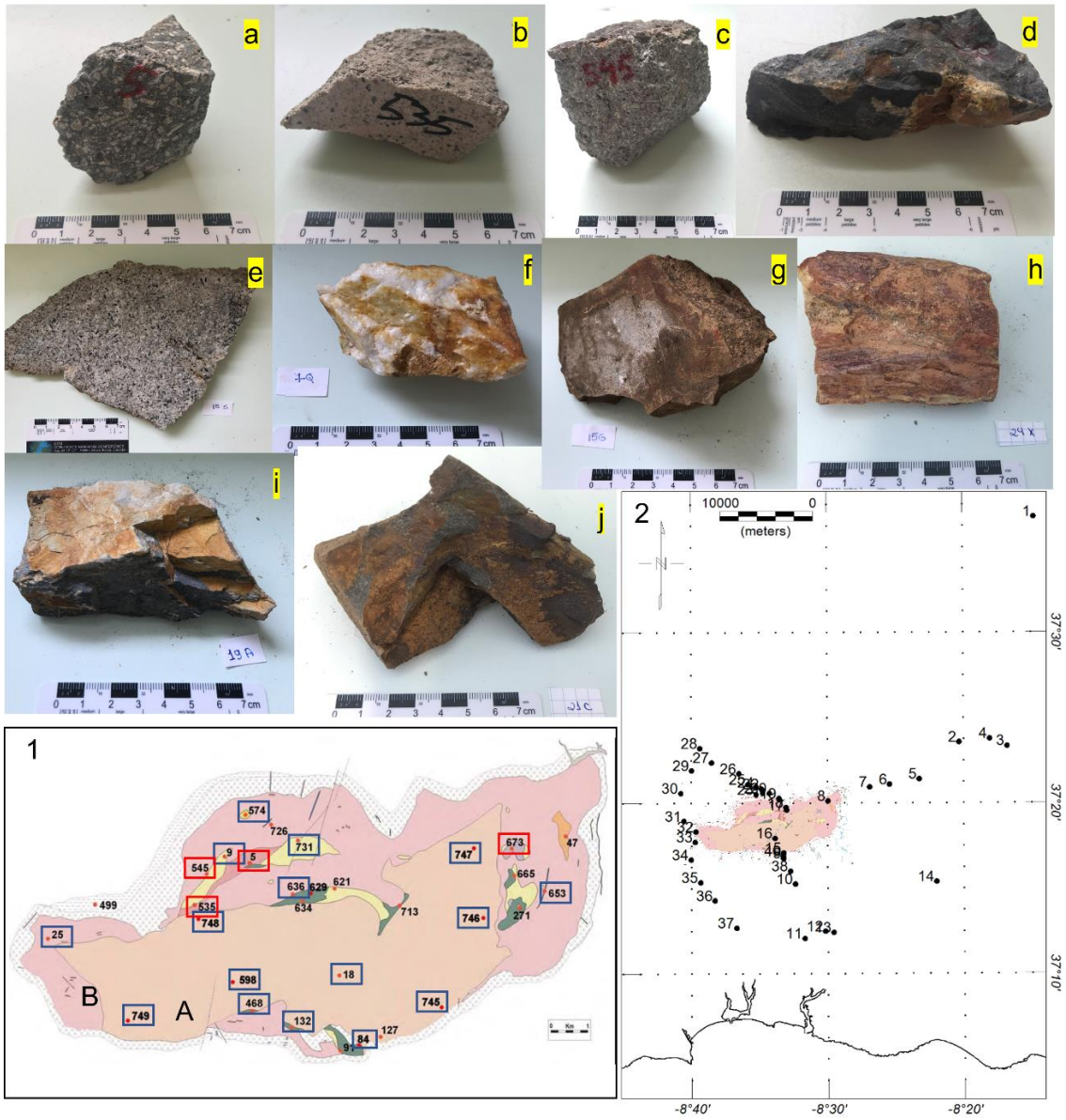

Figure 3.3 Rocks from the Valadares (2004) set: a) gabbro, b) syenite, c) breccia of gabbro and feldspar clasts with syenitic matrix and d) breccia of clasts and matrix from gabbros and feldspars. Rocks from the ATLAS sample campaign: e) syenite, f) quartz, g) graywacke, h) shale, i) slate, and j) hornfel.1) Geological map of Monchique with Valadares (2004) samples, the red rectangle indicates the samples presented in the photos. 2) Location of ATLAS samples, 2021 (this study), with the geological map of the Monchique Hill (map location in Figure 3.2).

4. Data processing and analysis

4.1. Gravity data processing

SPIDER Project data

Collected data were processed using an in-house-programmed software developed by Dr. Machiel Bos (Baker and Bos, 2003), and the Oasis Montaj software (Seequent). The correction for scale factors, earth tides and instrumental drift were made through the in-house-programmed software. Further corrections and analysis were conducted using Oasis Montaj.

The height measured by the GPS (ellipsoidal height) was converted into orthometric height using the EGM96 15´ (Earth gravitational model of 1996, 15´x15´ resolution). The latitude correction was applied using the 1984 Blakely formula (1.3). The free-air correction was calculated considering a constant gradient of 0.3086 mGal/m, from Blakely 1984 (1.5). For the calculation of the Bouguer anomaly we used a correction density of 2670 kg/m^3, usually assumed as the average density of crustal materials (Blakely, 1996).

For the calculation of the terrain correction and the resulting complete Bouguer anomaly, we first followed the Oasis Montaj information: "*A regional terrain correction grid (RTCG) is calculated over a survey area based on a regional Digital Elevation Model (DEM) and at the resolution of a local, more detailed DEM. Note the calculation of the regional correction grid is optional, not required for the terrain correction*", and used only a general DEM as input. However, attempts to calculate the terrain correction without a RTCG were not successful (the correction values were always zero), but when a RTCG was given as input correction results were obtained. As input regional DEM grid we used a topography grid comprising the area of the Monchique intrusion and surroundings, with 1km resolution. As local grid we used data obtained from the Advanced Spaceborne Thermal Emission and Reflection Radiometer (ASTER), Global Digital Model (GDEM) version 2, October 2011 (https://terra.nasa.gov/about/terra-instruments/aster), with 30 m resolution. The RTCG was used to calculate the terrain correction joining with the local GDEM grid from ASTER. The software uses a combination of the method described by Nagy (1966) and Kanet (1962). The correction density used was also 2670 kg/m^3.

IGP data

The downloaded IGP data already included calculated free-air anomaly; i.e. previous necessary corrections had already been applied. We then calculated the Bouguer anomaly using the free-air anomaly as base considering the average density value of 2670 kg/m^3 for the crustal materials. The terrain correction for the IGP data was made in the same way as the SPIDER data, using the same regional grid and local DEM grid and correction density value of 2670 kg/m^3. Because we do not have the observed values of the gravity anomaly, the complete Bouguer anomaly was calculated as the sum of the Bouguer anomaly and the terrain correction as indicated by the Oasis Montaj information.

Merging of datasets

To merge the two datasets, we searched for spatially coincident measurements that could serve as "tie points". We verified that 3 data points closely coincided in both datasets, as shown in Figure 4.1. We assumed a constant difference to exist between the two datasets and applied a correction of 17 mGal for the free-air and 10.4 mGal for the Bouguer in the IGP data to put the two datasets in the same reference. Each dataset of free-air, Bouguer and complete Bouguer anomalies and terrain correction values was gridded using minimum curvature algorithm using 200m cell size with 10 cells extended beyond data

(Figure 5.2). The minimum curvature gridding method fits a minimum curvature surface, which is the smoothest possible surface that will fit the given data values (Oasis Montaj information).

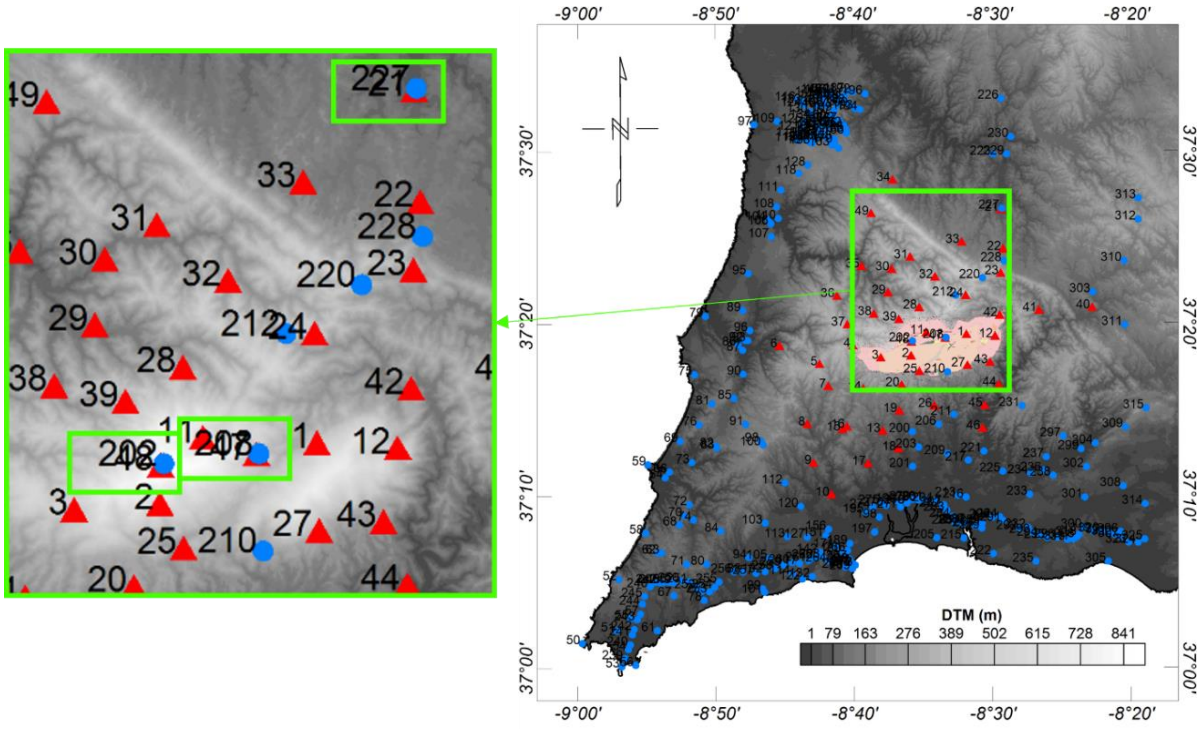

Figure 4.1 Map with the location of gravity measurements. The red triangles are the points of SPIDER project, and the blue circles the points from IGP data. With zoom in the coincident points in both datasets, circled in green.

4.2. Magnetic data processing

The drone magnetic data was corrected for instrumental drift and for geomagnetic diurnal variations using data from the São Teotónio base station (Figure 3.2). The total field considered was 43658 nT, with inclination of 50.8º and declination of -1.4º (27/05/2021), this IRGF was removed from the total field measurements to obtain the anomaly field grid in the region.

For the Iberian anomaly map, we performed a downward continuation of 2 km (thus to 1 km height) to put the data in an approximated altitude with respect to the drone data, considering that the highest point of Monchique hill is ~1 km. We also did an upward continuation of the drone data to compare with the Iberian anomaly map. In both cases, it was concluded that the maps weren't sufficiently compatible to perform a merge of the data (i.e., continuation transformations did not led to compatible maps, in either case). We attribute this to the great difference in resolution between them: the cell size of the Iberian anomaly map is 4 km (which is the flight line separation distance) and the drone data is 30 m (compare Figure 3.2 and Figure 4.2; further discussed below). To have a better spatial understanding of the anomaly, by translating the anomaly maximum over the magnetic source, we also performed a reduction to the pole in both data sets.

4.3. 3D inverse Modeling

3D inverse modeling was performed for gravity and magnetic anomaly data to obtain 3D models of density and susceptibility distribution, respectively. In order to optimize the software algorithm, the input grids are resampled for 1 sample per cell, that is, to have one data value for each 3D cell according to the model resolution.

For the gravity inversion, input data was the Complete Bouguer anomaly grid of Monchique and surrounding region, including Ponta de Sagres (Figure 3.1), with 200 m of cell size and 10 cells extended beyond data; and the elevation local grid DEM, from ASTER, GDEM. The model has dimensions of 236×243×72 m, and maximum depth of 40 km, and no linear background was removed from the data. The upper and lower boundaries for density values were 600 to -400 kg/m^3 respectively, which correspond to variations centered on the correction density used for Bouguer calculations (2670 kg/m^3) i.e., density is constrained to values between 3270 and 2270 kg/m^3.

Magnetic inversion was performed for several datasets: (i) drone data; (ii) Iberian aeromagnetic map (IAM-R) cropped to the area shown in Figure 3.2; (iii) IAM cropped to a smaller area (IAM-L) (Figure 4.1); (iv) IAM reduced to pole (IAM-RTP); (v) IAM downward continuation for 2km (IAM-DC); and (vi) drone data reduced to pole (RTP). The susceptibility models all had linear background removal and susceptibility values between 0 and 0.1 SI. The specifications for each model are presented in Table 4.1.

Table 4.1 Susceptibility models processing parameters, with specifications of input grid (type of grid, gridding cell size, extended cell beyond data), IGRF assumed as inducing field (total field strength, inclination and declination), elevation of data constant above terrain (m), model cell dimensions (m), and model maximum depth (km). The symbol (-) refers to not applicable parameters.

	Input grid			**IGRF**					
Model	type	Cell size (m)	Extended cells beyond data	Total Field (nT)	Inc. (º)	Dec. (º)	Elev. (m)	Cell dimensions (m)	Depth (km)
Drone data	Total magnetic field	30	30	43658	50.8	-1.4	30	154x221x72	40
Drone data RTP	RTP anomaly field	30	30	43740	90	0	30	154x221x72	40
IAM-R	Magnetic anomaly field	4000	-	43484	52	-6	3000	240x227x58	40
IAM-RTP	Magnetic anomaly field	4000	-	43484	90	0	3000	240x227x58	40
IAM-DC	Magnetic anomaly field	4000	-	43484	52	-6	1000	240x227x58	40
IAM-L	Magnetic anomaly field	4000	-	43484	52	-6	3000	231x243x55	40

4.4. 2D forward modeling

2D forward modeling was further developed for a representative NNW-SSE profile (Figure 4.2). This profile was defined in order to cross the maximum and minimum peaks of the magnetic anomaly in regions most possibly constrained by acquired drone data, and not affected by data interpolation. Input magnetic data was the drone anomaly data (not RTP) with elevation of 30 m above terrain. As inducing field we considered for each model the respective IGRF as referred above (IAM or drone IGRF specified before). We then created two models with vertical sections cut across the 3D inversion models as initial constrains, followed by geological constraints as the outcropping lithologies and its borders. We followed the three major peaks of the magnetic signal that coincides with some of the peaks of susceptibility in the 3D model in that profile, including one outcrop of gabbro in the geological map. A

main observation from our modeling efforts is that the high susceptibility volume must have a NW-dipping border at its southern side in order to fit the anomaly gradient.

We initially produced 2 extra models to compare the drone data inversions with the IAM inversion on the 2D profile. First, we used as input the drone data and created a body similar to the IAM model (following a 3D vertical section). Then we created another model with the IAM data as input but following the 3D body for the drone data inversion. Both of them agree in the long wavelength signal. We also studied the density effects of those models in the gravity field (complete Bouguer anomaly), but the results are unclear and will not be presented in this work.

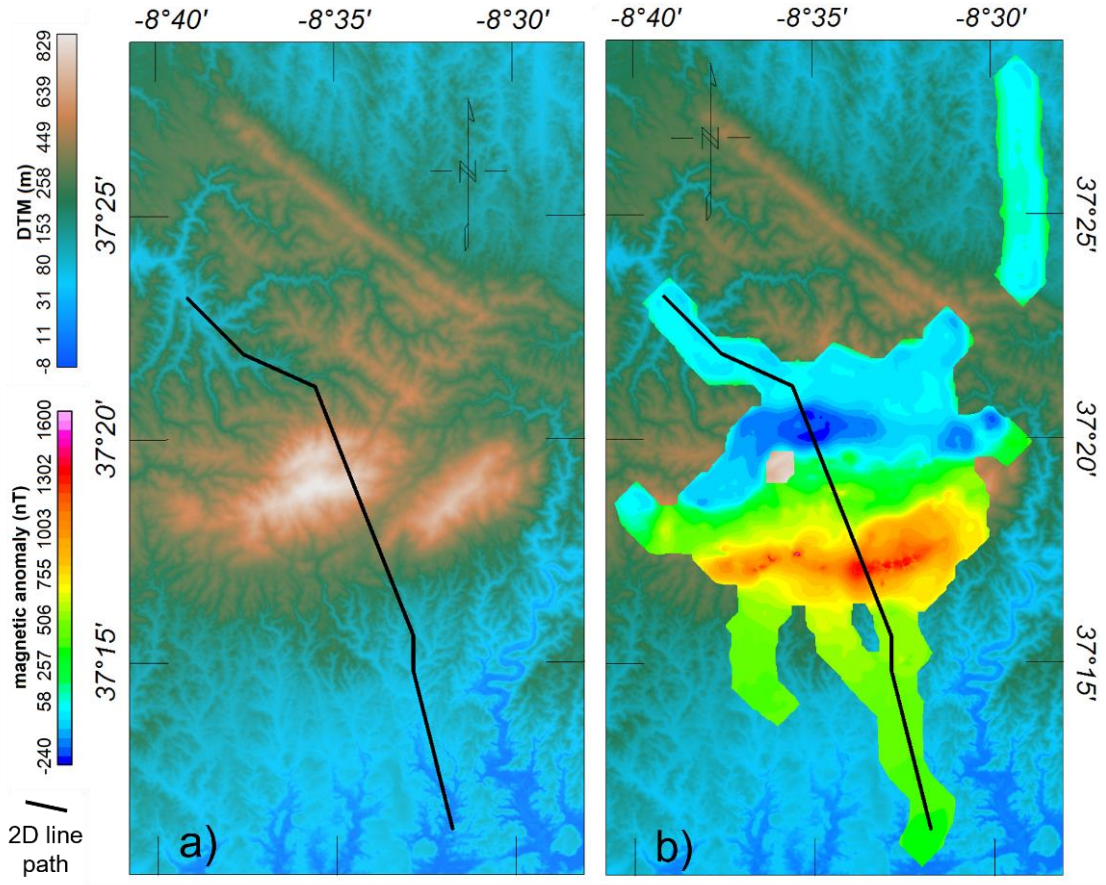

Figure 4.2 Location of the 2D modeled profile overlaying (a) the topography and (b) the input magnetic anomaly field data grid (with 30m of cell size and 30 extended cells beyond data.) See Figure 3.2 for location.

5. Results

In this section we present the results obtained with the analysis and processing of the data described in sections 3 and 4.

5.1. Gravity field

Figure 5.1 shows the gravity sample points color-scaled for the several processing and analysis steps (free-air anomaly, Bouguer anomaly, terrain correction and complete Bouguer anomaly). Figure 5.2 shows the respective gridded datasets. The final dataset is very consistent, showing that a good merging of the two datasets (SPIDER project and IGP) was achieved.

The calculated free-air anomaly grid has mean value of 68.4 mGal and standard deviation of 17.7 mGal. The highest free-air anomaly values are observed in the center of the Monchique outcropping intrusion, clearly correlating with the topography, with maximum value of 141.9 mGal at Fóia peak. Minimum values of 38.1 mGal are observed in the southeast part of the area, near Armação de Pêra.

The most outstanding feature in the Bouguer anomaly grid is the positive gradient towards the southwest. In Monchique, the Bouguer anomaly is almost insignificant, only showing a little negative peak in the center of the Monchique hill. Maximum, minimum, mean and standard deviation of Bouguer anomaly are 98.5, 38.2, 62.5 and 15.5 mGal, respectively.

The terrain correction is more significant in the center of the Monchique hill, as expected, because is the part where altitudes are higher. Terrain corrections vary between 0 and 9.9 mGal (at the 900 m high Fóia hill), with mean of 0.3 mGal and standard deviation of 0.9 mGal. The final maps of terrain correction, free-air and Bouguer anomaly are represented in Figure 5.1.

In the complete Bouguer anomaly map (after terrain correction) we can see that the small negative Bouguer anomaly in the center of Monchique hill disappears, showing only the regional trend of the gravity field for the region. The complete Bouguer anomaly grid has maximum, minimum, mean, and standard deviation values of 98.3, 39.3, 62.6 and 14.4 mGal, respectively. The two survey datasets complement each other, allowing for a much denser mapping of the gravity field in the Monchique region that can be seen in the grids in Figure 5.2.

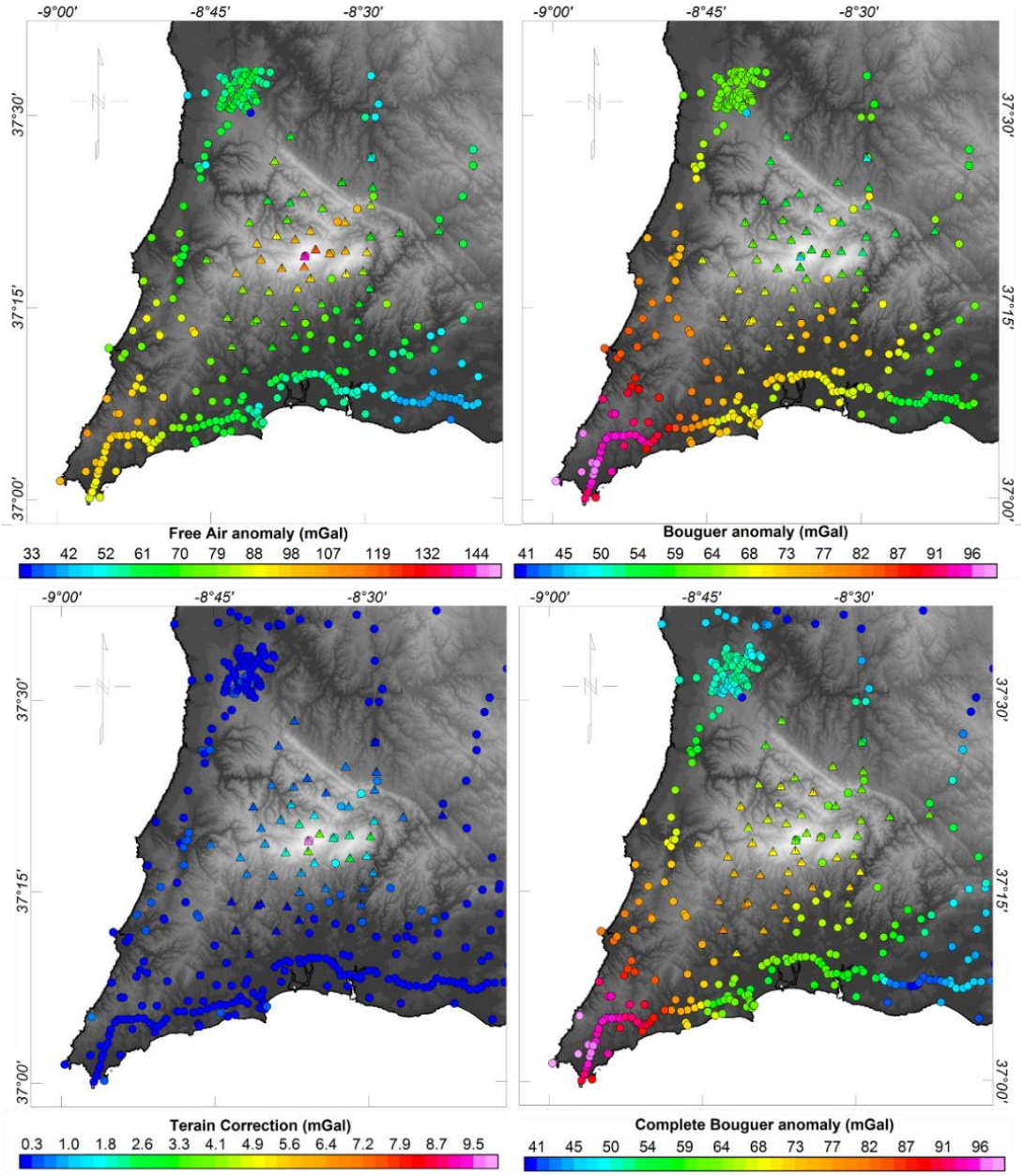

Figure 5.1 Map of color-scaled data points for free-air, Bouguer and Complete Bouguer anomaly; and terrain correction in Monchique region, resulting from the merge of the two SPIDER and IGP databases. The triangles are the points from SPIDER project, and the circles from the IGP.

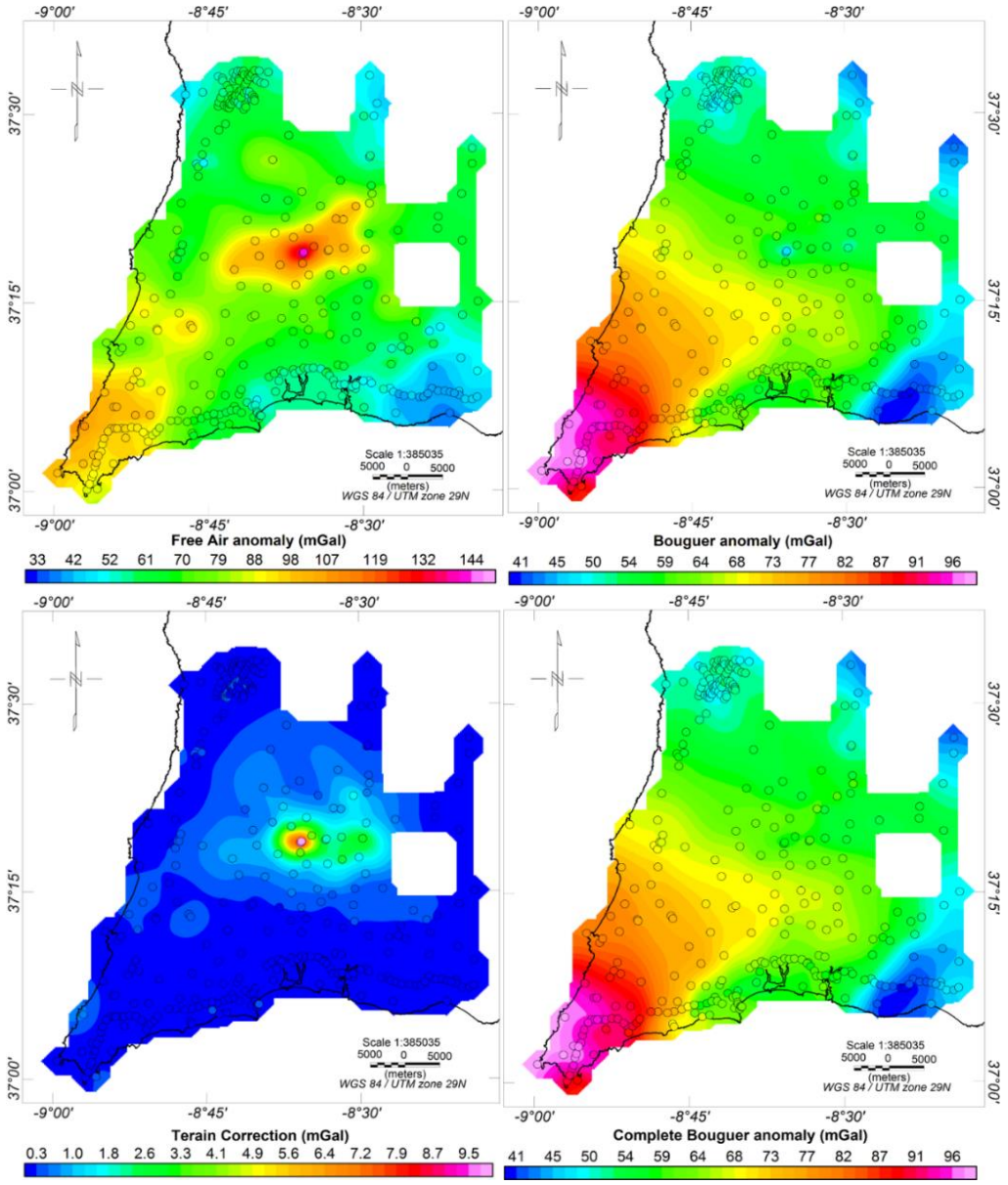

Figure 5.2 Regional maps of Free-air, Bouguer and Complete Bouguer anomaly, and terrain correction in Monchique region. Result of the merging datasets.

5.2. Density analysis for the Monchique alkaline complex and surroundings

To better understand the gravity field associated with the Monchique intrusion, we decided to analyze the densities of the rocks in Monchique. Although the Bouguer anomaly presents a slight negative peak in the top of the hill, when applied the terrain correction this peak disappears showing only the regional variation of the gravimetric field for this region. As this field depends on the densities of the rocks below the surface, the study of the density values can help understanding why there is no significant local change in gravity field, associated with the Monchique intrusion.

The density values of the rocks samples by type of rock can be seen in Table 5.1. Among the analyzed rocks the type with higher density values were the gabbros collected by Valadares (2004), which reach 3310 kg/m^3. Gabbros outcrop mainly at the border of the syenite in small sites at north, south, and east of the intrusion (Figure 2.1). We analyzed 11 samples of syenites from Valadares (2004) set, they yield a mean value of 2616 kg/m^3, with maximum of 2975 kg/m^3 and minimum of 2519 kg/m^3. Syenites

collected during the ATLAS sampling present a larger variation in the density values (see the maximum and minimum values in Table 5.1, Figure 5.3 and Figure 5.4) than for Valadares samples; however, the difference between Valadares (2004) and ATLAS samples is not significant in terms of mean values for the syenites (~160 kg/m^3). The breccia samples have similar values to the syenites, with mean of 2683 kg/m^3, minimum of 2517 kg/m^3, and maximum of 2973 kg/m^3.

All samples collected during the ATLAS campaign (that focused on host rock sampling) have density lower than 2700 kg/m^3. The most common rock types were slate ("A", 14 samples) and greywacke ("G", 22 samples), both with mean values of density around 2500 kg/m^3, minimum around 2300 kg/m^3 and maximum around 2600 kg/m^3 (Figure 5.3). Some hornfels, quartz and shale were also collected but in minority. The hornfels were found only in one site, and quartz is typically found filling fractures.

The total mean value of the hosting rocks density is 2530 kg/m^3 and for the intrusion rocks is 2665 kg/m^3 (Table 5.1). With a difference of only 135 kg/m^3, the intrusion and hosting rocks have very similar values of densities, the histogram in Figure 5.5 shows that in both of them the predominant value of densities lays around 2600 kg/m^3.

Table 5.1 Mean, maximum and minimum (kg/m^3) density values for each rock type in each group of samples, ATLAS (magmatic and host rocks) and V.Valadares (only magmatic rocks) and the total for intrusion and hosting rocks.

ATLAS				
Rock type	Mean	Maximum	Minimum	Nº of samples
Syenites	2455	2565	2299	6
Slate	2502	2623	2320	14
Graywacke	2546	2694	2269	22
Hornfels	2673	2673	2673	1
Shales	2356	2415	2297	2
Quartz	2562	2603	2528	4
Valadares (2004)				
Rock type	Mean	Maximum	Minimum	
Syenites	2616	2975	2519	11
Breccia	2683	2973	2517	5
Gabbros	2966	3310	2583	6
Total				
Rock type	Mean	Maximum	Minimum	
Hosting rocks	2530	2694	2269	43
Intrusion rocks	2665	3310	2299	28
Syenites	2560	2975	2299	17

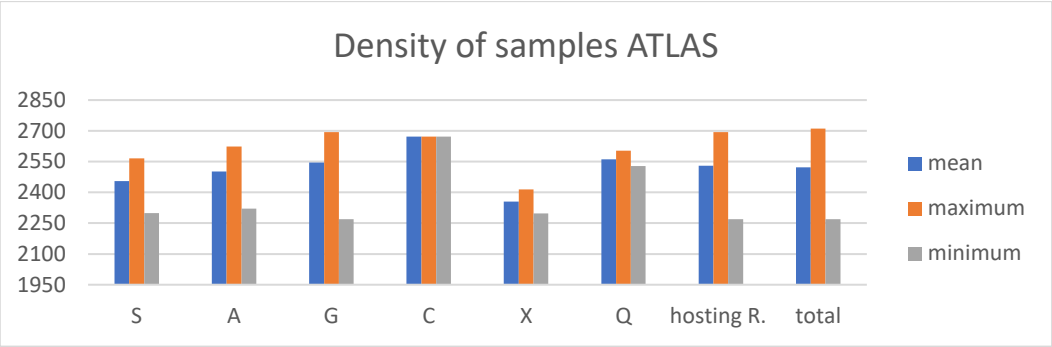

Figure 5.3 Comparison between different type of rocks in the ATLAS sampling. Syenites (S), slate (A), graywacke (G), hornfels (C), shales (X) and quartz (Q).

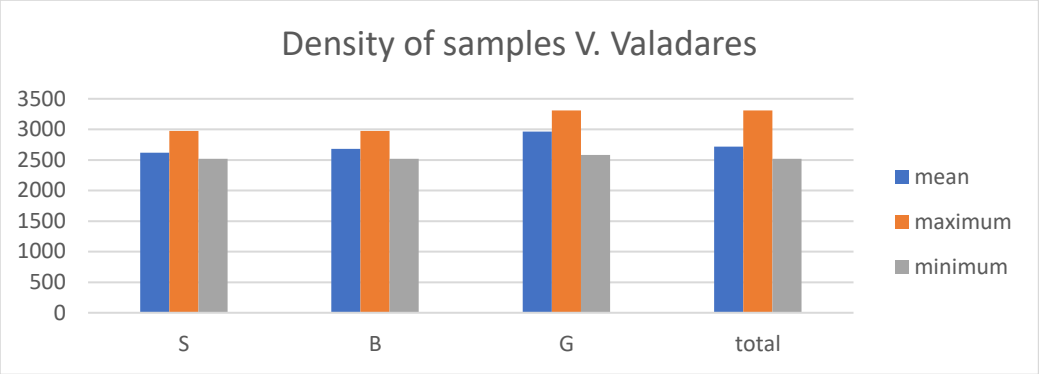

Figure 5.4 Comparison between different type of rocks in the Valadares (2004) sampling. Gabbros (G), syenites (S) and breccia (B).

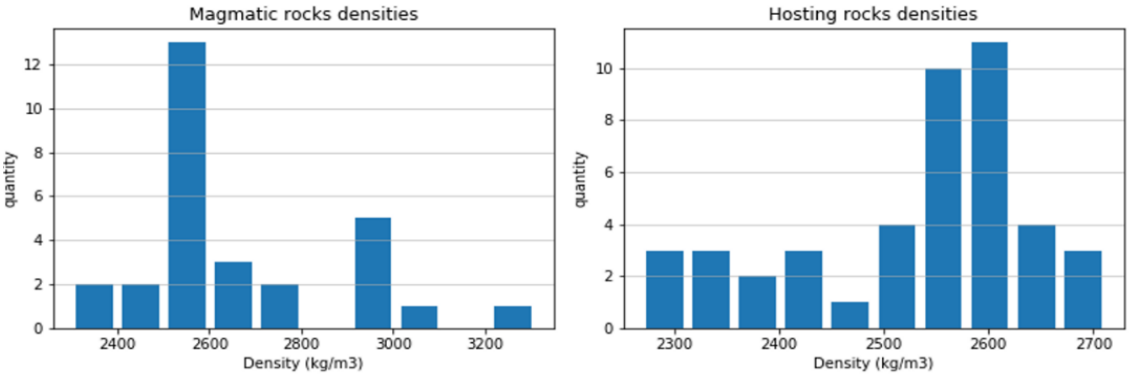

Figure 5.5 Histograms of densities values in the intrusion/magmatic type rocks (gabbros, syenites and breccia) and hosting type rocks (slate, graywacke, hornfels, shales and quartz).

5.3. Magnetic anomaly field

The magnetic dipole caused by the Monchique magmatic intrusion is identified in both the drone and IAM (non-RTP) data grids (Figure 5.6a, b and c), showing the negative branch of the dipole at north and the positive at south (as expected for normal polarity magnetized bodies in the northern hemisphere). However, the anomaly is better defined in the drone data as the acquisition had more resolution, and it reaches values of 1700 nT as positive peak and -700 nT as negative peak, i.e., 2400 nT of peak-to-peak amplitude. Meanwhile, in the IAM data, the positive dipole has the higher values around 500 nT, and the lowest around -70 nT, i.e., 570 nT peak-to-peak amplitude.

The map in Figure 5.6b shows the downward continuation of 2 km of IAM data (surveyed at 3 km height) to put it on the same reference level as the drone data (1 km height). The dipole is slightly more

defined, with steepest gradient, but the anomaly is still very different from the drone data and doesn't represent the local variations of the anomaly field (Figure 5.6a, b, and c). To relocate the anomaly over the source, we performed reduction to pole in both datasets (IAM and drone), as shown in Figure 5.6d, e and f. From "d" to "e", was performed a downward continuation of 2 km of the reduced to pole grid, again showing the anomaly more defined and with slightly higher values in the center. The drone data reduced to pole puts the anomaly right below the Monchique Hill, the limits are well defined and close to the syenites borders from the geological map (Figure 5.6f). The maps in Figure 5.6 are in a linear color scale based in the drone data values interval.

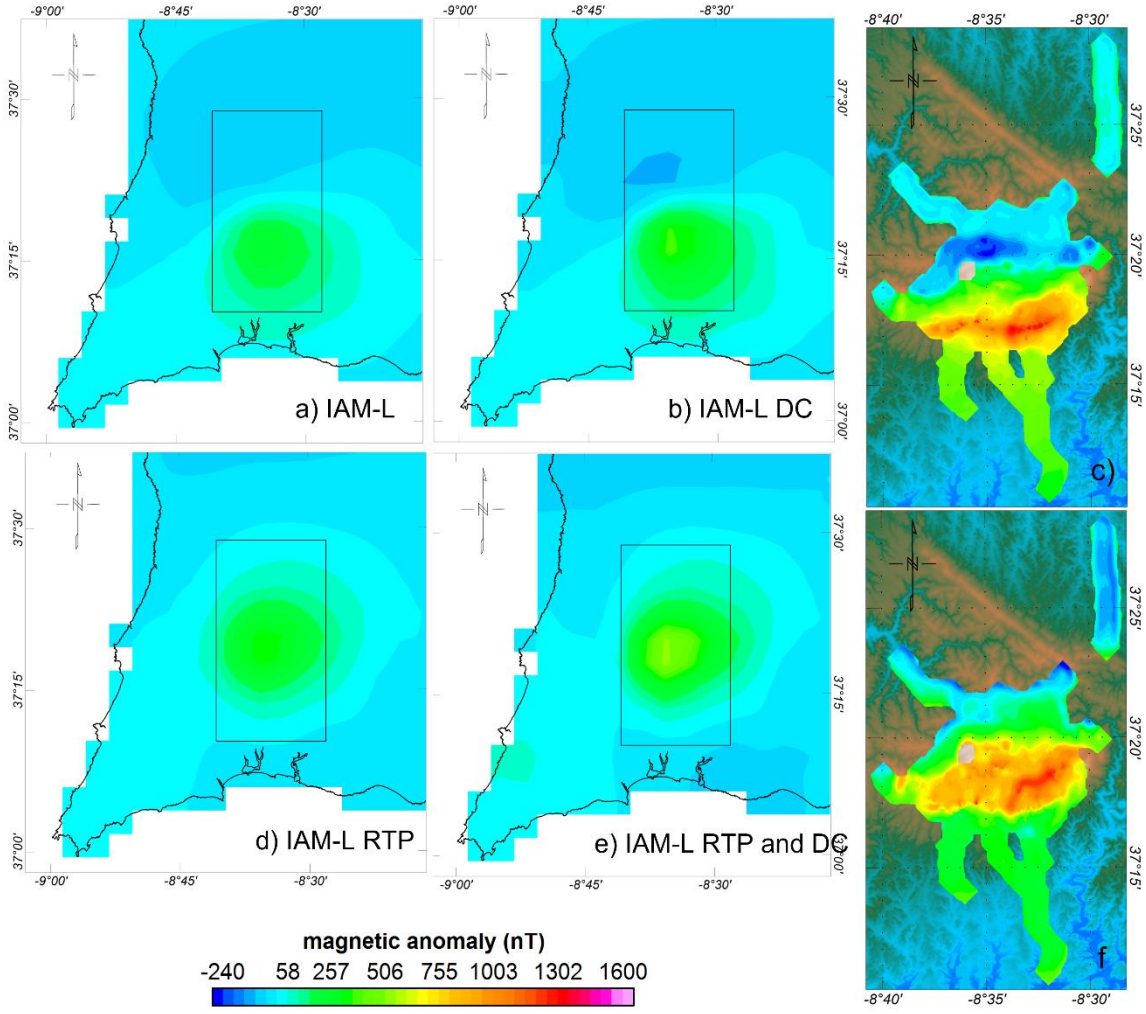

Figure 5.6 Magnetic anomaly grids: a) IAM-L grid for Monchique´s magnetic anomaly; b) IAM-L grid downward continued in 2km (thus, at 1 km height); c) magnetic anomaly field for drone data; d) IAM-L grid reduced to pole; and e) IAM-L grid downward continued for 2 km and reduced to pole; f) Magnetic anomaly field reduced to pole, drone data. All plots in the same color scale.

5.4. 3D and 2D models

Inverse and forward modeling provide us new valuable insights to discuss the shape and extension of the magmatic intrusion. Results obtained from inversion of gravity and magnetic data are very distinct and show that the density and susceptibility contrasts do not necessarily correlate.

5.4.1. 3D gravity modeling

Focusing on the Monchique area, the 3D gravity and magnetic models have some similar characteristics but are very different in morphology from each other. Following the complete Bouguer anomaly map from Figure 5.2, we expected no positive anomaly close to the Monchique area because they only appear

in the SW part of the map, therefore we concentrate in the negative anomalies that could appear in the model. The density model is probably not too viable considering that the gravity field of the region shows no significant anomalies and even the negative peak in Monchique vanishes when the terrain correction is applied. Anyway, the model supports a negative body underneath Monchique that extends to east, with slightly decrease in density, around 70 kg/m^3 (not relevant for the regional trend). Figure 5.7 shows map views and 3D crosscuts of the bodies defined by isosurfaces of density. The bodies of isosurfaces ρ<2600 kg/m^3 and ρ<2650 kg/m^3 are interpreted as related to the magmatic intrusion because the fracturing that may occur in this scenario could lead to a decrease of density (Figure 5.7b and c), with ~20 km length divided in two sections. The west part below Fóia is the smaller one, with depth ~6 km, and length of ~9 km. The eastern part below Picota has ~11 km of length and depth around 10 km.

Figure 5.7d also shows the positive density anomaly isosurfaces, in which outstands a high-density body shallowing towards Ponta de Sagres where it reaches 10km bellow surface. This density anomaly shows a steep vertical gradient, from 2800 kg/m^3 to 3000 kg/m^3 in less than 4 km in depth. These higher densities are in agreement with the complete Bouguer anomaly map justifying the positive trend towards SW.

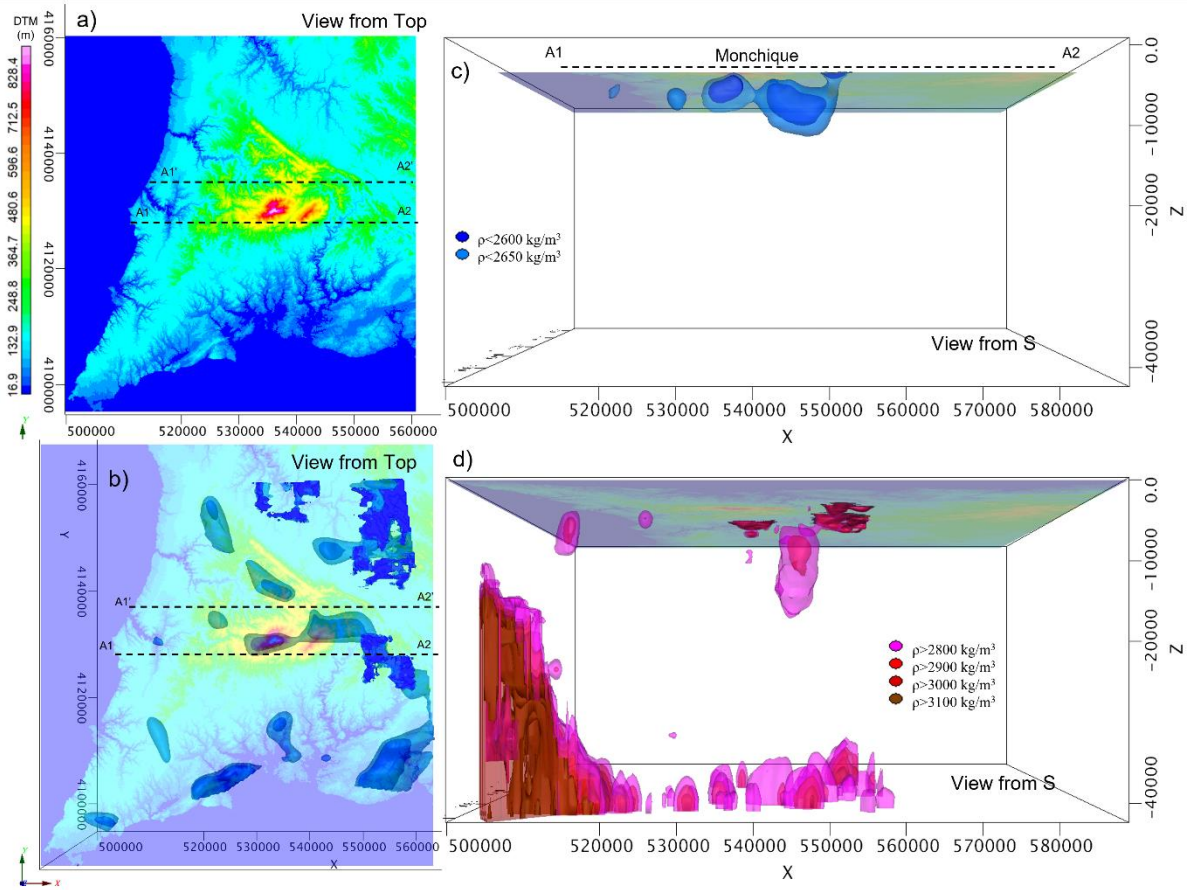

Figure 5.7 Results of 3D gravimetric inversion: modeled density bodies. (a)Topography map view of analyzed area with area A1-A2-A1'-A2' (W-E); (b) Top view of isosurfaces ρ<2600 kg/m^3 and ρ<2650 kg/m^3; (c) South view of isosurfaces of ρ<2600, 2650 kg/m^3, section A1-A2; (d) South view of isosurfaces ρ>2800, 2900, 3000 and 3100 kg/m^3, bodies modeled for Ponta de Sagres;

5.4.2. 3D magnetic models

In Figure 5.8 we present results from two inversion models, using RTP and non-RTP magnetic data.

The susceptibility models obtained from magnetic inversion present a main shallower body of 15 km of length right below the Monchique Hill that reaches 10 km of depth in the east part. A second high

susceptibility body is modeled from 15 to 27 km of depth (Figure 5.8b). We note that for model 2 (RTP input data) the shallower body is more concentrated close to the surface mostly above 5 km of depth, and the second deeper body is smaller and more localized, between depths of 17-25 km. In both models, the deeper body may be just an inversion artifact, as our data is very restricted to Monchique and doesn't cover the surroundings, which would be necessary to better constrain the deeper susceptibility distribution. Figure 5.8 also shows the topography and the location of the NS and EW crosscuts presented in Figure 5.9.

Figure 5.9 shows a closer and more detailed view of the shallow high susceptibility body. Isosurfaces of magnetic susceptibility are defined for >0.01, >0.02, >0.05 and >0.08 SI. The A1-A2 cut shows the deepest parts of the body, the A3-A4 the larger EW part, the B1-B2 the body bellow Fóia, and the B3-B4 the body bellow Picota.

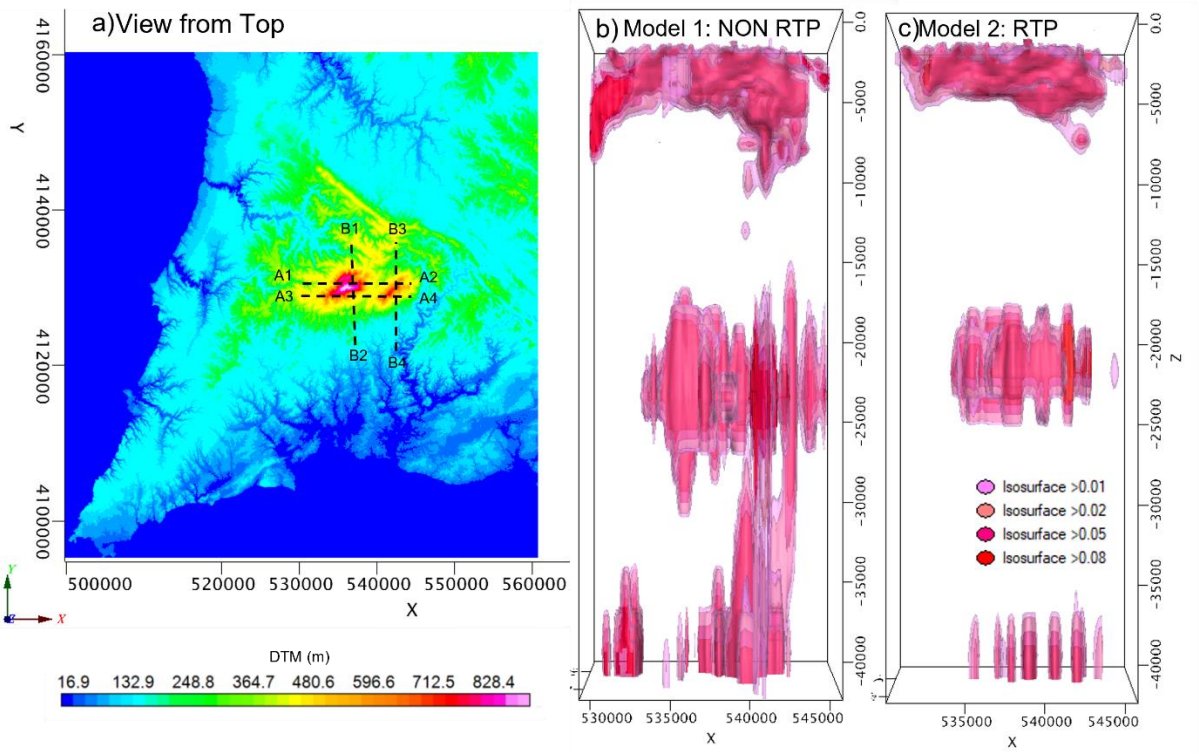

Figure 5.8 3D susceptibility distribution models obtained from inversion of drone magnetic data: a) map view with topography and location of crosscuts; b) Model 1: input data is total field anomaly and c) Model 2: input data is total field anomaly reduced to pole (RTP). Isosurfaces are shown for >0.01 SI values.

The other susceptibility models that were made using the Iberian Anomaly Map as input data are presented in the appendix. The 3D models are represented as isosurfaces of >0.01, >0.02, >0.05 and >0.08 SI in view from the south with inclination of 15° (Figure A.1, Appendix). The models are very similar between them, they all have one big body modeled below Monchique that leans to east. Considering the values of >0.01 SI, the bodies reach lengths of 30 km and depths around 30 km (except on the IAM-L model, Figure A.1d, where the depth is around 15 km). In west view (appendix Figure A.2), we can notice a tail on the Monchique intrusion that extends towards north in all models making the body have ~20 km of length in that direction. In Figure A.3 are represented simultaneously all susceptibility and density models in view from south.

5.4.3. 2D forward models

We have achieved two different models as the most likely to reflect the morphology of the Monchique intrusion. As initial constraints to build the 2D models we used vertical sections cut across the 3D

inversion models. Then we used geological constraints to refine the proposed body, as the outcropping lithologies and its borders. We followed the three major peaks of the magnetic signal that coincides with some of the peaks of susceptibility in the 3D model in that profile, including one outcrop of gabbro in the geological map. A main observation from our modeling efforts is that the high susceptibility volume must have a NW-dipping border at its southern side in order to fit the anomaly gradient. This southern limit may represent a major fault structure or zone of fracturing that constrained the ascending of the material.

Model A has a "fork-like" morphology, in comprising a single gabbro intrusion with s=0.076 SI, that divides first into two branches (around 2km of depth) and then one of these branches divides again in two thin ones. The principal larger branch causes the higher magnetic signal in the recording (~1200 nT). One of the thinner branches reaches the surface in the exact location where a gabbro body crops out, and is the magnetic source attributed to a short wavelength observed anomaly. Following the geological map, we verified in our profile the outcropping location of the different syenite units and defined two distinct bodies: nuclear syenite (S=0.020 SI) and boundary syenite (S=0.025 SI). This is the model that follows the most the shape of the 3D inversion modeled body as indicated by the S=0.02 SI isosurface.

The second model, model B, is inspired in the Terrinha et al. (2018) models for the Sintra intrusion. Both Monchique and Sintra magmatic complexes belong to the same magmatic event and have some similar characteristics. This model has two separated gabbro plugs (S=0.095 SI and S=0.068 SI) and the syenite (S=0.02) body was modeled with a laccolith morphology. In both models the base of the intrusion reaches depths around 7 km. Both models fit satisfactorily the observed data in its main features, and the fit could be improved by further refining the geometry of the magnetic sources. (Figure 5.10).

In both models we attempted to include the deeper second body revealed in the 3D modeling, but as it shows little (almost none) influence in the 2D profile anomaly, it's not included in the 2D models presented here.

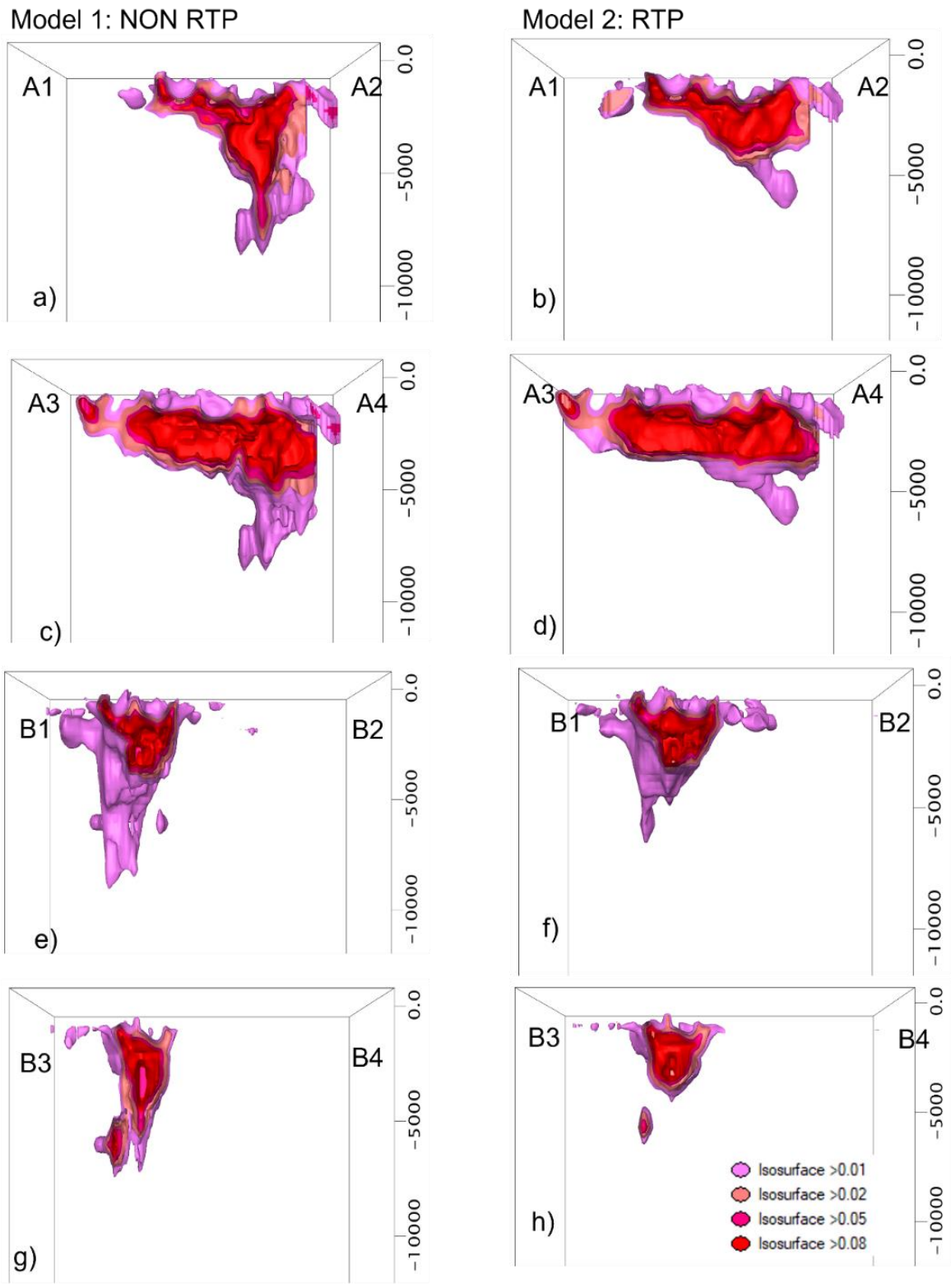

Figure 5.9 Vertical sections across the 3D magnetic Susceptibility models (Figure 5.8) focusing on their top part (down to 10 km depth). Model 1: non RTP drone data as input. Model 2: RTP drone data as input as input. a) and b) cut A1-A2 (WE)

viewed from south. c) and d) cut A3-A4 (WE) viewed from south. e) and f) cut B1-B2 (NS) viewed from west. g) and h) cut B3-B4 (NS) viewed from west. Shown as isosurfaces wrapped around areas of >0.01, >0.02, >0.05 and >0.08 SI.

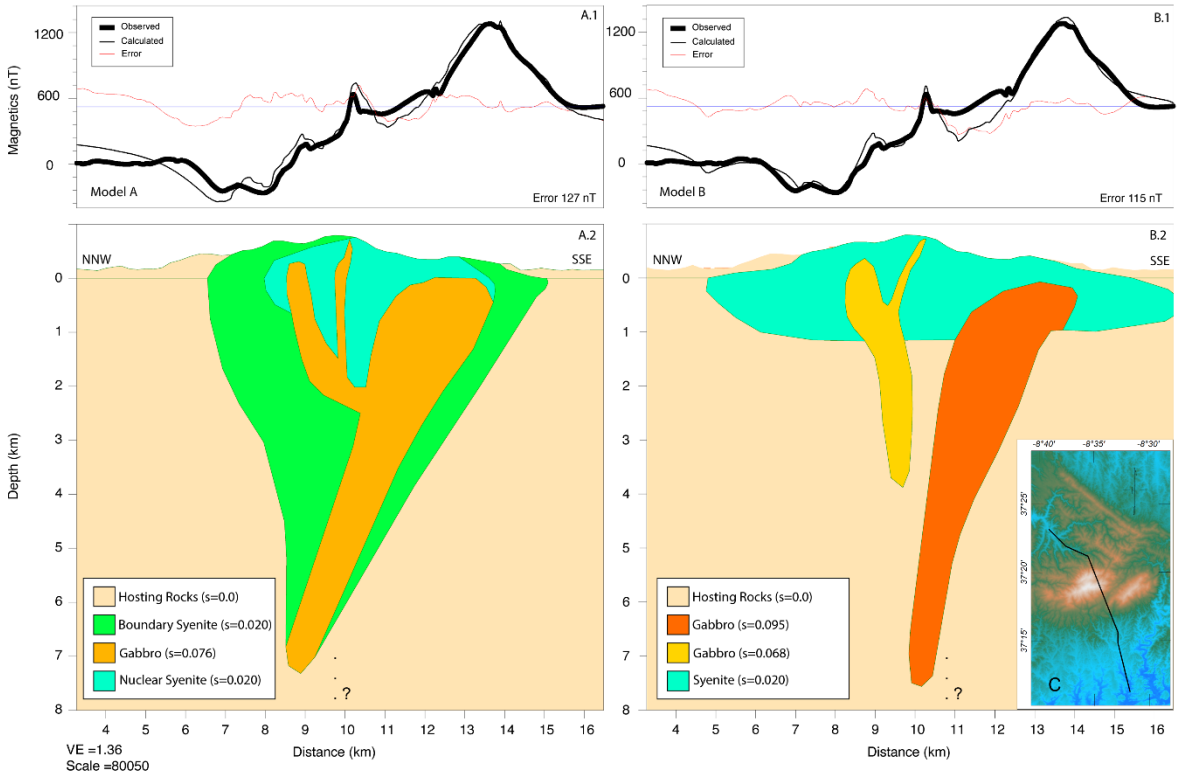

Figure 5.10 Two alternative 2D forward magnetic models for the Monchique intrusion that fit the observed magnetic anomaly (see Figure 4.2 for profile location. a.1; b.1) observed magnetic anomaly (thick black) and model magnetic response (thin black) and error (red), in nT a.2; b.2) Susceptibility models and interpreted lithologies. Vertical exaggeration of 1.36.

6. Discussion

6.1. New gravity anomaly map for Southwest Portugal.

The density of the MAC intrusive rocks can be divided in two groups: (1) the first group comprises the denser type of rocks (gabbros), which have higher values of density (ρ_{mean}=2966 kg/m^3) and represent, in the geological map (Figure 2.1), the minority of the complex with only a few outcrops mapped; (2) the second group comprises the syenites (ρ_{mean}= 2455 kg/m^3 or ρ_{mean} =2616 kg/m^3) and breccia (ρ_{mean}= 2683 kg/m^3). The syenites are the dominant type of rock in the intrusion, the ones collected from fragments of exposed rocks on the surface (ATLAS sampling), probably suffer weathering and have lower density than the fresher ones collected by Valadares.

The gravity anomaly field is influenced by the density variation of the crustal materials. In case of intrusions, to exist a gravimetric anomaly the densities of the material underneath the surface need to have a significant difference between them, or the thickness of the intrusion material must be greater than the ones around creating a root on the crustal layer. Our density analysis (Figure 5.5) shows that the majority of the rocks of both intrusion and hosting type have densities around 2600 kg/m^3, supporting the idea that the difference between them is not significant to be observed in the gravity field with complete Bouguer correction applied (Figure 5.2). The evidence of existence of a root bellow the Monchique alkaline complex was already suggested by Matias (1996) based on the analysis of seismic data. In Matias (1996) the Monchique intrusion implies a strong contrast of seismic velocities in relation to the hosting rocks, being a strong source of diffractions. The increase of the seismic velocity below the Monchique hill led him to assume a block of higher velocity (5. 9 km/s) at the surface (till around 3km of depth) and raise the possibility of a crustal root related to the intrusion. If we consider our susceptibility RTP model (Figure 5.8) the concentration of material in the intrusion is <5 km of depth. On the other hand, the inversion models derived of the IAM data (appendix Figure A.1) are more consistent with the suggestion of the crustal root underneath Monchique because they are modeled by a body that reaches 30 km of depth, same depth as the crustal base.

Anyways our 3D density inversion models show a slight decrease of the densities right underneath the outcropping of the intrusion, around 70 kg/m^3 (Figure 5.7), but the morphology of the body modelled is not in agreement with our other models based in the susceptibility. So, we are considering the model not viable, due to the not small variation in the gravity anomaly. One of the reasons for the little decrease of density may be the hydrothermalism of the area that may decrease the densities of the rocks involved and thus the measurements of gravity.

The most noticeable pattern in this new gravity field map of the southwest Portugal is the high positive anomaly towards Ponta de Sagres, with densities higher than 2800 kg/m^3 ascending from the Moho (>31km Matias, 1996) till 10 km of depth. This suggests a reduction of the thickness of the continental crust. The tomography of the area (Veludo et al., 2017) shows a high vp/vs ratio at depths bellow 12 km. The vp/vs ratio has a direct proportionality with the density: if the material has a higher density the ratio is going to be higher because the velocity of the P waves, or compressional waves, will increase. This supports the idea of a high-density area in Ponta de Sagres at shallower depths.

6.2. Implications for the morphology of the intrusion

Our results on inverse and forward modeling provide new valuable insights for discussing the shape and extension of the magmatic intrusion.

Our two sets of magnetic data, IAM and drone, are not comparable due to the scale of the acquisitions. The IAM grid has a spacing of 4 km between points, and our drone data grid has only 30 m. In

aeromagnetic acquisitions the high frequency data is normally lost due to the high altitude, that tends to attenuate the small wavelengths anomalies. The IAM data captures only the longer wavelength anomaly, and it doesn't cross the magnetic maximum and/or minimum generated by the Monchique intrusion (Figure 6.1). For these reasons, a direct comparison between them by merging of the anomaly maps was not possible. However, the long wavelength anomaly is in agreement in both datasets for our 2D profile (Figure 6.2).

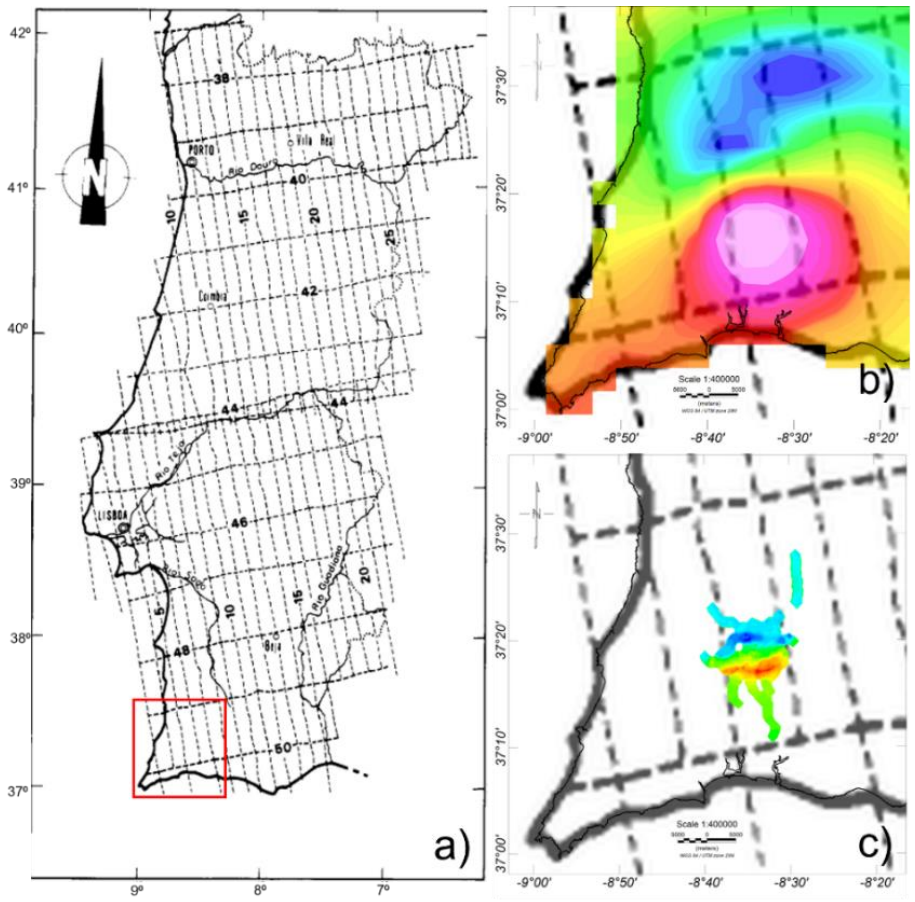

Figure 6.1 a) Acquisition lines of the Iberian Anomaly Map from (Miranda et al., 1989) with b) anomaly map from IAM and c) magnetic anomaly from drone data.

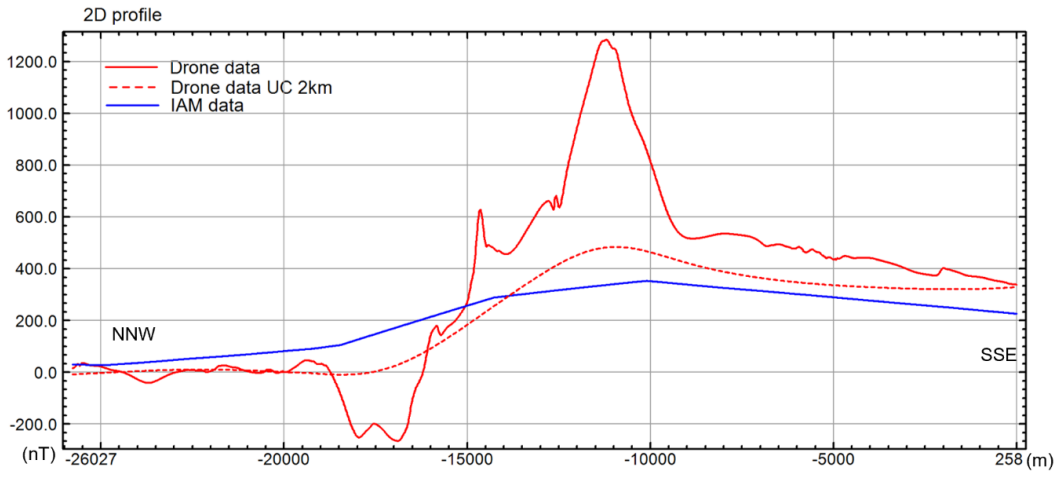

Figure 6.2 Comparison for the 2D profile between the IAM and drone data.

The magnetic susceptibility values for Monchique rocks by Barbosa (1999), 0.020-0.025 SI, and the field measurements of magnetic susceptibility in Monchique sienites by González-Castillo et al. (2014), 0.029 SI, are in agreement with our main body in the 3D-2D modeling (0.02 SI).

The 3D models for density (Figure 5.7), even if not reliable, and for susceptibility (Figure 5.9) both agree that the larger part of the intrusion lays on the east part, below Picota hill, limited to depths of less than 10 km. The low-density body may represent a zone of fracturing, however its extension east of Picota and its morphology is not supported.

The magnetic anomaly that we acquired on the drone campaigns agrees with the González-Castillo et al. (2013) (Figure 6.3). González-Castillo et al. (2013) used this profile to create a 2D model for the Monchique massif and surroundings, they proposed a roughly 35 km long lenticular and asymmetrical section extending in depth toward the north. Their model of the magnetic anomalies constrains the geometry of the sienite as a laccolith with depths <5 km. This geometry is typical of large laccolith plutons emplaced in the upper crust (González-Castillo et al., 2013). Our 2D and 3D models do not support an extension of the laccolith towards east, but the IAM inversion model (appendix Figure A.2) shows a tail in that direction with less than 15 km long at depths around 10-20 km that creates a link between our results and the González-Castillo et al. (2013).

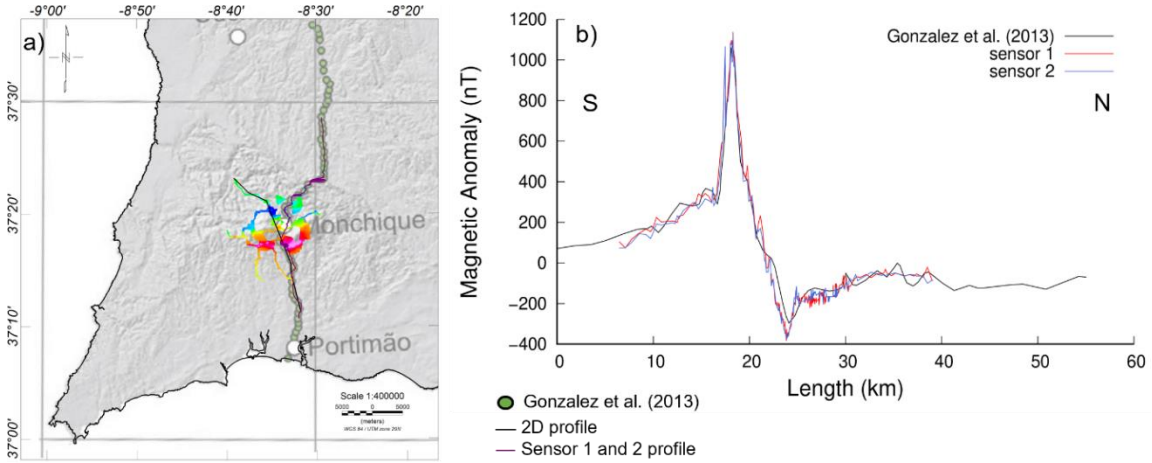

Figure 6.3 Comparison between our data and the González-Castillo et al. (2014): a) Monchique map with our 2D profile (black line), the González-Castillo et al. (2014) profile (green circles) and our correspondent data (purple line), and the drone magnetic anomaly field (the figure behind the map is from González-Castillo et al. (2014); b) Overlap of the two magnetic anomaly profiles (nT). Sensors 1 and 2 are the two drone magnetometers Comparison figure provided by Dr. Machiel Bos, researcher in the ATLAS project.

Both Sintra and Monchique magmatic complexes belong to the same magmatic event. Our forward model B (Figure 5.10) is based on the Sintra models presented by Terrinha et al. (2018), where several plugs of gabbro are revealed by younger laccolith granites at the surface. The granite displays medium-to-low susceptibility values, partially falling within the "nonmagnetic" field, with the exception of a few sites close to the gabbro–syenite (Terrinha et al., 2018). In Monchique we propose that the syenite may assume the laccolith form around the plugs of gabbro, being responsible for the medium-to-low susceptibility. The plugs of gabbro may or not be connected between them, that is, could be just one main body of gabbro that ascended from the magmatic chamber dividing into other branches probably due to existing fault structures, or, alternatively, several independent plugs of gabbros. A depth extension of the intrusion of >8 km is supported by our analysis, but not definitive. The second deeper body modeled in the 3D susceptibility model can be a model artifact; in fact, our data doesn't have a sufficient coverage of the area around Monchique hill, and thus may not be enough to define longer wavelength anomalies due to deeper sources. On other hand, the IAM models have low resolution due to large scale

sampling (note that the main Monchique anomaly was not measured by the aeromagnetic survey). We tested the inclusion of this second and deeper body in the 2D forward modeling and verified that its presence is irrelevant for the calculated magnetic response.

6.3. Relating to the seismicity and hydrothermalism

Barbosa (1999) suggested that the two main blocks of MAC were originated from the same magmatic camara, but the Picota side probably had a slower cooler and more perfect crystallization. The ascending of the magma would have been fast given that the contact zone is well defined and inclined. It was also suggested that Picota is likely to be the younger block, and it ascended when the Fóia material was not fully cold but with elevated viscosity, as it indicates the tectonic depression west of Picota. Rock (1982b, 1978) and Sousa (1926) had already proposed the division of the complex in several magmatic pulses that evolved separately from deeper levels. Clavijo and Valadares (2003) believed that this fact suggests the existence of an extensional ante-Mesozoic structure ENE-WSW that have conditioned the installation of the intrusion in a superficial level of the crust. Our results 2D-3D support the idea of ENE-WSW structures constraining the intrusion (Figure 6.4), and in Figure 5.10 for the 2D NNW-SSE where the model seems to have a perpendicular structure (ENE-WSW) delimitating the body.

Monchique is the most active seismic cluster in Portugal (Carrilho et al., 2004; Custódio et al., 2015). It also presents active hydrothermal activity. Most of the hypocenters are located between 5 and 20 km in the mid-crust, considering that the base of crust in this region is around 31km (Dündar et al., 2016; Soares, 2018), usually with magnitude <4. The seismicity itself is not diffuse but clusters along two lineations, one oriented NNE–SSW and another oriented EW (Custódio et al., 2015; Soares, 2018). These lineaments also roughly reflect the rheological boundaries observed at the surface, and Soares (2018) suggests that they can define existing active faults. Another hypothesis would be that the earthquakes would originate in small fractures indicating the presence of a zone of fracture, shear zone (Soares, 2018). GPS data indicates that Western Iberia is undergoing oblique convergence, oriented NW-SE to WNW–ESE, with respect to Nubia (Fernandes et al., 2007; Neres et al., 2016; Nocquet, 2012; Serpelloni et al., 2007). The NNE-SSW lineations which are perpendicular to the plate convergence and the WNW-ESE lineations, parallel to the plate convergence, accommodates mostly strike-slip faulting in mainland Portugal (Custódio et al., 2015).

In Figure 6.4, we propose a fracture zone (FZ) with direction ENE-WSW and inclination toward north that may represent one of or part of an ante-Mesozoic structure that controlled the installation of the massif. Right underneath the modeled shallower body, around 10 km of depth, starts a zone of high seismicity area were hypocenters aligned along directions NNE/NE concentrates (Soares, 2018). Underneath this high seismicity region zone there may be another high susceptibility body >0.01 SI, where some sparse hypocenters are located, although the existence of this body needs to be confirmed. The area between 10-17 km of depth appears to be a fractured zone, maybe shear zone, that can relate to hydrothermalism where the seismicity concentrates below the shallow intrusion. The seismicity may also indicate a change in the rheology, a transition to a more brittle material.

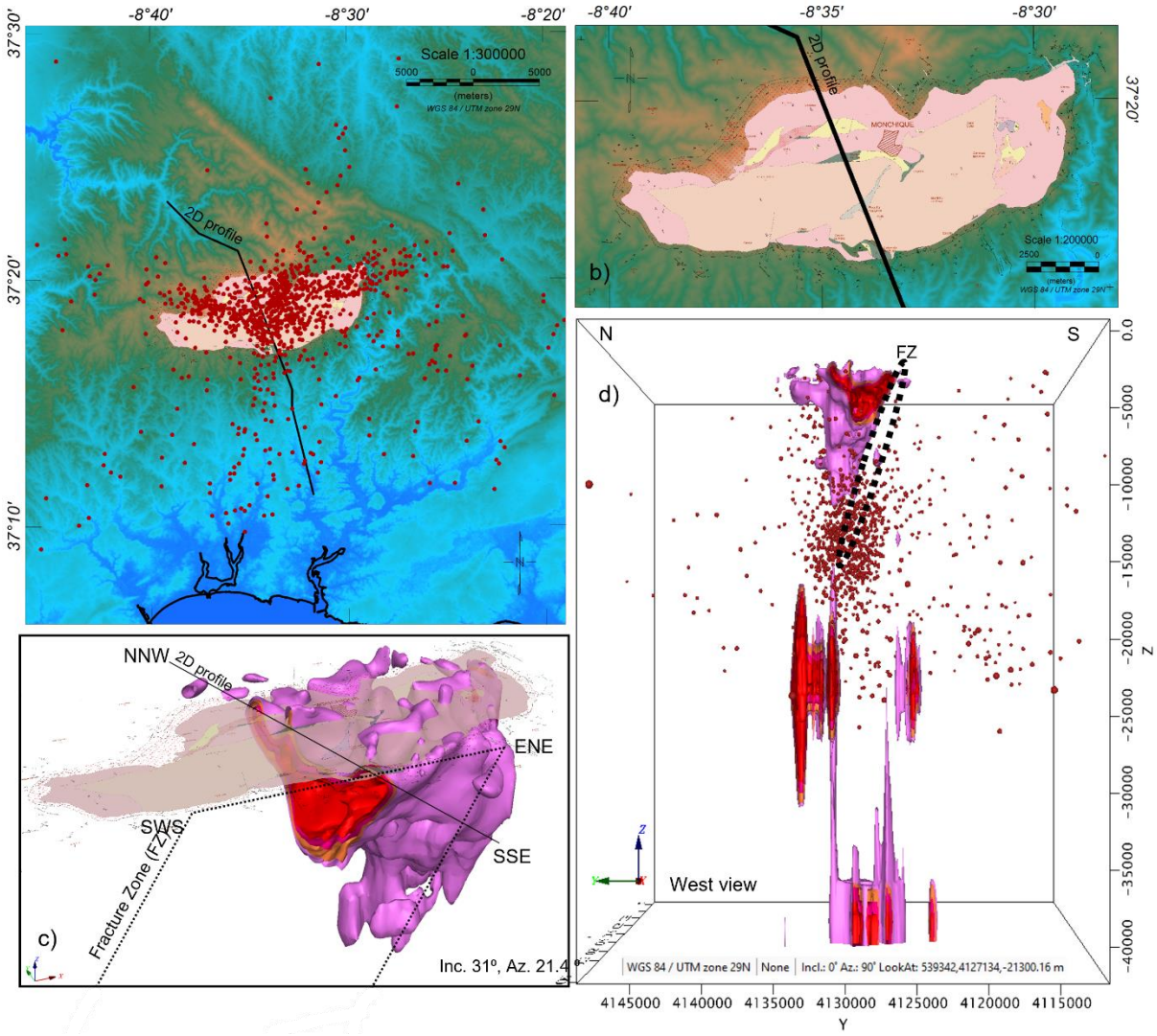

Figure 6.4 a) Topography map with location of 2D profile and map view of hypocenters from Soares (2018). *b) geological map with 2D profile. c) 3D view of geological map with 3D susceptibility inversion isosurface of >0.01 SI cut on the 2D profile (NNW-SSE), and fracture zone FZ (WSW-ENE). d) 3D west view of susceptibility body cut on 2D profile with fracture zone FZ and hypocenter from* Soares (2018).

The MAC is considered a hydrothermal pneumatic intrusion. Is assumed that the groundwater flow is approximately radial since the intrusion is composed of two more or less concentric nepheline syenite bodies. According to the Catalog of Geothermal Resources of Mainland Portugal (CRGPC), the water from the Monchique region circulates inside the massif and in the surrounding environment through a complex system of fractures that provide its penetration in depth (Soares, 2018). Most of the springs of water are in the south of the massif. We suggest that the zone around 10-17 km of depth is the host of the hydrothermal activity where the water circulates and acquired part of its composition influenced by the massif (such as Sodium, feldspar and nepheline (PGRHreport, 2014)); the water probably ascends preferentially by a fracture zone south of the massif as proposed in Figure 6.4.

This fracture zone is also supported by the tomography results from Veludo et al. (2017) where the massif imposes: in the upper 5 km, a high-Vp anomaly with scarce seismicity is observed, which can correspond to the main syenitic body of the massif, lying above a low-Vp anomaly where the majority of the earthquakes are located and correspondent to our proposed fracture zone. To the SW of the massif, there is evidence of significant anomalies in the Vp and Vp/Vs ratios (Veludo et al., 2017). Looking to the tomography map in depth the low vp/vs between extend until 16 km of depth followed by another

high vp/vs area. The ratio vp/vs has a direct proportionality with the density, if the material has a higher density the ratio is going to be higher because the velocity of the P waves, or compressional waves, will increase. This supports a high-density area where the massif is supposed to be, above a low-density area (the fracture zone) and another deeper high-density area that can be the second body of the 3D model. Although the tomography agrees with our model, a high-resolution tomography study would be needed for the area to confirm these results.

The installation of the Monchique intrusion, according to (Clavijo and Valadares, 2003), started with the subvertical dikes, followed by syenites, which is similar to the model also proposed for the installation of the Sintra complex. This later acid magma may have irregular forms and is much greater in volume then the previous basic magma. The heterogeneous boundary syenite must have been formed by the accretion of successive magmatic pulses, during which it incorporated basic and corneal rock fragments generating the breccias that are associated with gabbro outcrops. In the final stage, a large pulse of more homogeneous, nepheline-rich syenitic magma intrudes in the center of the structure slightly displaced to the south, probably using the deformation structures resulting from the previous basic intrusions.

7. Conslusions

Our results lead to the following conclusions.

There is no Bouguer gravimetric anomaly caused by the magmatic intrusion of Monchique. despite the high amplitude of the observed positive free air anomaly, it is canceled after the Bouguer and terrain corrections are applied. This implies that density variations between the intrusion and surrounding materials (host rock) are too small to be noticed in the regional pattern of the area. At the southwest, towards Ponta de Sagres, our results support a rapid shallowing of high-density rocks compatible with mantle material, suggesting a significant crustal thinning. Available seismic modeling corroborates a decrease of crustal depth to around 25 km in this region (Dündar et al., 2016). Further studies are needed to confirm these results and estimate the precise depth of the crust, including offshore data.

The intrusion is composed by a syenite body with plug-like gabbroic bodies, the latter causing the major part of the magnetic anomaly. Because in the geological map the gabbros represent a smaller part of the outcropping massif, the fit of the magnetic anomaly implies that these bodies are larger in depth reaching around 8km. The syenites involve the gabbros on the surface but their extension in depth is undetermined, and we have proposed two possible models for their geometrical relationship. The continuity of the intrusive body, or the existence of other deeper bodies bellow 8km is still open for discussion and may be better understood with a spatially wider data acquisition, with better resolution and closer to the source. It will also profit from more resolved tomographic models. The deeper part of the intrusion locates bellow Picota hill on the east, and the magmatic body elongates for about 10km in W-E direction.

Underneath the superficial intrusive body, a fracture zone between approximately 10-20 km is supported, likely along the same direction as the major concentration of hypocenters, alongside another fracture zone with ENE-WSW directions that outcrops the surface carrying water from the hydrothermal activity to the south part of the massif. But we still need more resolution on the tomography and location of the hypocenters to affirm depth values of material boundaries.

Bibliographic references

Baker, T.F., Bos, M.S., 2003. Validating earth and ocean tide models using tidal gravity measurements. Geophysical Journal International 152, 468–485. https://doi.org/10.1046/j.1365-246X.2003.01863.x

Baranov, V., Naudy, H., 1964. Numerical Calculation of The Formula of Reduction To The Magnetic Pole. GEOPHYSICS 29. https://doi.org/10.1190/1.1439334

Barbosa, S., 1999. Estudo geoestatístico de dados experimentais da anisotropia da suscetibilidade magnética de rochas do maciço de Monchique.

Bernard-Griffiths, J., Gruau, G.R., Cornen, G., Azambre, B., Macé, J., 1997. Continental Lithospheric Contribution to Alkaline Magmatism: Isotopic (Nd, Sr, Pb) and Geochemical (REE) Evidence from Serra de Monchique and Mount Ormonde Complexes, JOURNAL OF PETROLOGY.

Blakely, R.J., 1996. Potential Theory in Gravity and Magnetic Applications, Stanford-Cambridge Program. Cambridge University Press. https://doi.org/10.1017/CBO9780511549816

Bonhomme, M., Mendes, F., Vialette, Y., 1961. Âges absolus par la méthode au strontium des granites de Sintra et de Castro Daire au Portugal. COMPTES RENDUS HEBDOMADAIRES DES SEANCES DE L ACADEMIE DES SCIENCES 252, 3305.

Borges, J.F., Fitas, A.J.S., Bezzeghoud, M., Teves-Costa, P., 2001. Seismotectonics of Portugal and its adjacent Atlantic area. Tectonophysics 331. https://doi.org/10.1016/S0040-1951(00)00291-2

Carrilho, F., Pena, A., Nunes, J., Senos, M.L., 2004. Catálogo sísmico instrumental 1970–2000, Tech. rep. Instituto de Meteorologia, ISBN: 972-9083-12-6, Depósito legal No: 221 955/05.

Clavijo, E., Valadares, V., 2003. A Estrutura do Complexo de Monchique. Comum. VI Cong. Nac. de Geologia, Ciências da Terra especial V.

Custódio, S., Dias, N.A., Carrilho, F., Góngora, E., Rio, I., Marreiros, C., Morais, I., Alves, P., Matias, L., 2015. Earthquakes in western Iberia: Improving the understanding of lithospheric deformation in a slowly deforming region. Geophysical Journal International 203, 127–145. https://doi.org/10.1093/gji/ggv285

Dias, R.P., Cabral, J., 2002. Interpretation of recent structures in an area of cryptokarst evolution—neotectonic versus subsidence genesis. Geodinamica Acta 15. https://doi.org/10.1080/09853111.2002.10510756

Domingues, A., Custódio, S., Cesca, S., 2013. Waveform inversion of small-to-moderate earthquakes located offshore southwest Iberia. Geophysical Journal International 192. https://doi.org/10.1093/gji/ggs010

Duarte, J.C., Rosas, F.M., Terrinha, P., Schellart, W.P., Boutelier, D., Gutscher, M.-A., Ribeiro, A., 2013. Are subduction zones invading the Atlantic? Evidence from the southwest Iberia margin. Geology 41. https://doi.org/10.1130/G34100.1

Dündar, S., Dias, N.A., Silveira, G., Kind, R., Vinnik, L., Matias, L., Bianchi, M., 2016. Estimation of the Crustal Bulk Properties Beneath Mainland Portugal from P-Wave Teleseismic Receiver Functions. Pure and Applied Geophysics 173, 1949–1970. https://doi.org/10.1007/s00024-016-1257-4

Dunn, A.M., Reynolds, P.H., Clarke, D.B., Ugidos, J.M., 1998. A comparison of the age and composition of the Shelburne dyke, Nova Scotia, and the Messejana dyke, Spain. Canadian Journal of Earth Sciences 35. https://doi.org/10.1139/e98-058

el Moudnib, L., Villaseñor, A., Harnafi, M., Gallart, J., Pazos, A., Serrano, I., Córdoba, D., Pulgar, J.A., Ibarra, P., Himmi, M.M., Chourak, M., 2015. Crustal structure of the Betic–Rif system, western Mediterranean, from local earthquake tomography. Tectonophysics 643. https://doi.org/10.1016/j.tecto.2014.12.015

Feio, M., 1951. A evolução do relevo do Baixo Alentejo e Algarve. Com. Ser. Geol. Portugal XXXII, 303–477.

Fernandes, R.M.S., Miranda, J.M., Meijninger, B.M.L., Bos, M.S., Noomen, R., Bastos, L., Ambrosius, B.A.C., Riva, R.E.M., 2007. Surface velocity field of the Ibero-Maghrebian segment of the Eurasia-Nubia plate boundary. Geophysical Journal International 169. https://doi.org/10.1111/j.1365-246X.2006.03252.x

Fernández, M., Marzán, I., Torne, M., 2004. Lithospheric transition from the Variscan Iberian Massif to the Jurassic oceanic crust of the Central Atlantic. Tectonophysics 386, 97–115.

Ferreira, M.R.P., Macedo, C.R., 1979. K-Ar Ages of the Permian-Mesozoic Basaltic Activity in Portugal. Abstracts VI. Europ. Col. Geochron., Cosmochron. and Isotope Geology, Norway.

Geldmacher, J., Hoernle, K., Klügel, A., Bogaard, P. v. d., Wombacher, F., Berning, B., 2006. Origin and geochemical evolution of the Madeira-Tore Rise (eastern North Atlantic). Journal of Geophysical Research 111. https://doi.org/10.1029/2005JB003931

Geldmacher, J., van den Bogaard, P., Hoernle, K., Schmincke, H.-U., 2000. The 40Ar/39Ar age dating of the Madeira Archipelago and hotspot track (eastern North Atlantic). Geochemistry, Geophysics, Geosystems 1. https://doi.org/10.1029/1999GC000018

Gong, Z., Langereis, C.G., Mullender, T.A.T., 2008. The rotation of Iberia during the Aptian and the opening of the Bay of Biscay. Earth and Planetary Science Letters 273. https://doi.org/10.1016/j.epsl.2008.06.016

González, A., Torné, M., Córdoba, D., Vidal, N., Matias, L.M., Díaz, J., 1996. Crustal thinning in the Southwestern Iberia Margin. Geophysical Research Letters 23. https://doi.org/10.1029/96GL02299

González-Castillo, L., Galindo-Zaldívar, J., Ruiz-Constán, A., Pedrera, A., 2014. Magnetic evidence of a crustal fault affecting a linear laccolith: The Guadiana Fault and the Monchique Alkaline Complex (SW Iberian Peninsula). Journal of Geodynamics 77, 149–157. https://doi.org/10.1016/j.jog.2013.10.007

González-Fernández, A., Córdoba, D., Matias, L.M., Torné, M., 2001. Seismic crustal structure in the Gulf of Cadiz (SW Iberian Peninsula). Marine Geophysical Researches 22. https://doi.org/10.1023/A:1012254420429

Granet, M., Wilson, M., Achauer, U., 1995. Imaging a mantle plume beneath the French Massif Central. Earth and Planetary Science Letters 136. https://doi.org/10.1016/0012-821X(95)00174-B

Grange, M., Scharer, U., Merle, R., Girardeau, J., Cornen, G., 2010. Plume-Lithosphere Interaction during Migration of Cretaceous Alkaline Magmatism in SW Portugal: Evidence from U-Pb Ages and Pb-Sr-Hf Isotopes. Journal of Petrology 51. https://doi.org/10.1093/petrology/egq018

Gupta, H.K. (Ed.), 2011. Encyclopedia of Solid Earth Geophysics. Springer Netherlands, Dordrecht. https://doi.org/10.1007/978-90-481-8702-7

Gutscher, M.-A., Dominguez, S., Westbrook, G.K., Gente, P., Babonneau, N., Mulder, T., Gonthier, E., Bartolome, R., Luis, J., Rosas, F., Terrinha, P., 2009. Tectonic shortening and gravitational spreading in the Gulf of Cadiz accretionary wedge: Observations from multi-beam bathymetry and seismic profiling. Marine and Petroleum Geology 26. https://doi.org/10.1016/j.marpetgeo.2007.11.008

Gutscher, M.-A., Malod, J., Réhault, J.-P., Contrucci, I., Klingelhoefer, F., Spakman, W., team, x, 2002. Evidence for active subduction beneath Gibraltar. Geology 30, 1071–1074. https://doi.org/10.1130/0091-7613(2002)030<1071:EFASBG>2.0.CO;2

Ishihara, T., 1989. Gravimetric determination of the density of the Zenisu Ridge. Tectonophysics 160. https://doi.org/10.1016/0040-1951(89)90391-0

Isles, D.J., Rankin, L.R. (Leigh R.), n.d. Geological interpretation of aeromagnetic data.

Kanet, M.F., 1962. A comprehensive system of terrain using a digital computer corrections, GEOPHYSICS.

Lotze, F., 1950. Observaciones respecto a la division de los variscides de la Meseta Iberica. Instituto “Lucas Mallada” (CSIC).

Lourenço, M.C., 1998. Recursos geotérmicos de baixa entalpia em portugal continental. In: 4º Congresso da Água, Lisboa.

Lourenço, M.C., Cruz, J., 2005. Aproveitamentos geotérmicos em portugal continental. XV Encontro Nacional do Colégio de Engenharia Geológica e de Minas da Ordem dos Engenheiros.

Lustrino, M., Wilson, M., 2007. The circum-Mediterranean anorogenic Cenozoic igneous province. Earth-Science Reviews 81. https://doi.org/10.1016/j.earscirev.2006.09.002

Martínez-Loriente, S., Sallarès, V., Gràcia, E., Bartolome, R., Dañobeitia, J.J., Zitellini, N., 2014. Seismic and gravity constraints on the nature of the basement in the Africa-Eurasia plate boundary: new insights for the geodynamic evolution of the SW Iberian margin. Journal of Geophysical Research: Solid Earth 119. https://doi.org/10.1002/2013JB010476

Martins, L.T., 1991. Actividade Ígnea Mesozóica em Portugal. Lisboa.

Martins, L.T., Madeira, J., Youbi, N., Munhá, J., Mata, J., Kerrich, R., 2008. Rift-related magmatism of the Central Atlantic magmatic province in Algarve, Southern Portugal. Lithos 102–124.

Marzoli, A., Renne, P.R., Piccirillo, E.M., Ernesto, M., Bellieni, G., Min, A. de, 1999. Extensive 200-Million-Year-Old Continental Flood Basalts of the Central Atlantic Magmatic Province. Science (1979) 284. https://doi.org/10.1126/science.284.5414.616

Mata, J., Alves, C.F., Martins, L., Miranda, R., Madeira, J., Pimentel, N., Martins, S., Azevedo, M.R., Youbi, N., de Min, A., Almeida, I.M., Bensalah, M.K., Terrinha, P., 2015. 40Ar/39Ar ages and petrogenesis of the West Iberian Margin onshore magmatism at the Jurassic–Cretaceous

transition: Geodynamic implications and assessment of open-system processes involving saline materials. Lithos 236–237. https://doi.org/10.1016/j.lithos.2015.09.001

Mata, J., Kerrich, R., MacRae, N.D., Wu, T.-W., 1998. Elemental and isotopic (Sr, Nd, and Pb) characteristics of Madeira Island basalts: evidence for a composite HIMU - EM I plume fertilizing lithosphere. Canadian Journal of Earth Sciences 35. https://doi.org/10.1139/e98-046

Matias, L.M., 1996. A Sismologia Experimental na Modelação da Estrutura da Crusta em Portugal Continental [Ph. D. thesis]. Universidade de Lisboa-Faculdade de Ciências.

McKerrow, W.S., M.N.C., A.P.E., C.G., C.C.J.& E.R.M.C., 2000. The Late Palaeozoic relations between Gondwana and Laurussia. Geological Society, London, Special Publications 179(1), 9–20.

Merle, R., Jourdan, F., Marzoli, A., Renne, P.R., Grange, M., Girardeau, J., 2009. Evidence of multi-phase Cretaceous to Quaternary alkaline magmatism on Tore–Madeira Rise and neighboring seamounts from ^{40} Ar/ ^{39} Ar ages. J Geol Soc London 166. https://doi.org/10.1144/0016-76492008-060

Merle, R., Schärer, U., Girardeau, J., Cornen, G., 2006. Cretaceous seamounts along the continent–ocean transition of the Iberian margin: U–Pb ages and Pb–Sr–Hf isotopes. Geochimica et Cosmochimica Acta 70. https://doi.org/10.1016/j.gca.2006.07.004

Miranda, J.M., Galdeano, A., Rossignol, J.C., Mendes Victor, L.A., 1989. Aeromagnetic anomalies in mainland Portugal and their tectonic implications, Earth and Planetary Science Letters.

Miranda, R., Valadares, V., Terrinha, P., Mata, J., Azevedo, M. do R., Gaspar, M., Kullberg, J.C., Ribeiro, C., 2009. Age constraints on the Late Cretaceous alkaline magmatism on the West Iberian Margin. Cretaceous Research 30, 575–586. https://doi.org/10.1016/j.cretres.2008.11.002

Morse, P.M., Feshbach, H., 1953. Methods of Theoretical Physics, part two. McGraw-Hill, New York.

Nagy, 1966. The gravitational attraction of a right rectangular prism. https://doi.org/10.1190/1.1439779

Neres, M., Bouchez, J.L., Terrinha, P., Font, E., Moreira, M., Miranda, R., Launeau, P., Carvallo, C., 2014. Magnetic fabric in a Cretaceous sill (Foz da Fonte, Portugal): Flow model and implications for regional magmatism. Geophysical Journal International 199, 78–101. https://doi.org/10.1093/gji/ggu250

Neres, M., Carafa, M.M.C., Fernandes, R.M.S., Matias, L., Duarte, J.C., Barba, S., Terrinha, P., 2016. Lithospheric deformation in the Africa-Iberia plate boundary: Improved neotectonic modeling testing a basal-driven Alboran plate. Journal of Geophysical Research: Solid Earth 121, 6566–6596. https://doi.org/10.1002/2016JB013012

Neres, M., Font, E., Miranda, J.M., Camps, P., Terrinha, P., Mirão, J., 2012. Reconciling Cretaceous paleomagnetic and marine magnetic data for Iberia: New Iberian paleomagnetic poles. Journal of Geophysical Research: Solid Earth 117. https://doi.org/10.1029/2011JB009067

Neres, M., Terrinha, P., Custódio, S., Silva, S.M., Luis, J., Miranda, J.M., 2018. Geophysical evidence for a magmatic intrusion in the ocean-continent transition of the SW Iberia margin. Tectonophysics 744, 118–133. https://doi.org/10.1016/j.tecto.2018.06.014

Nocquet, J.-M., 2012. Present-day kinematics of the Mediterranean: A comprehensive overview of GPS results. Tectonophysics 579. https://doi.org/10.1016/j.tecto.2012.03.037

Oliveira, J.T., 1990. Stratigraphy and syn-sedimentary tectonism in the South Portuguese Zone. Dallmeyer R.D. & Martínez García, E. (Eds.) Pre-Mesozoic Geology of Iberia. Springer, (Berlim-Heidelberg-Nova Iorque), 334–347.

Oliveira, J.T., 1983. The marine carboniferous in Portugal: a stratigraphic and sedimentological approach. Sousa M.J.L. & Oliveira J.T. (Eds.) The Carboniferous of Portugal. Men. Serv. Geol. Portugal, (Lisboa) 129–137.

Oliveira, J.T., Horn, M., Paproth, E., 1979. Preliminary note on the stratigraphy of the Baixo Alentejo Flysch Group, Carboniferous of Portugal, and on the palaeogeographic development compared to corresponding units in northwest Germany. Com. Serv. Geol. Portugal 65, 151–168.

PGRHreport, 2014. Relatório de caracterização - região hidrográfica das ribeiras do algarve (rh8).

Pinheiro, L., W.R., P. dos R.R., W.R.& R.A., 1996. The western Iberia margin: a geophysical and geological overview. Proceedings-ocean Drilling Program Scientific Results, National Science Foundation. 3–26.

Pinheiro, L.M., Wilson, R.C.L., Pena dos reis, R., Whitmarsh, R.B., Ribeiro, A., 1996. The Western Iberia Margin: a geophysical and geological overview. Proceedings of the Ocean Drilling Program, Scientifics Results 149, 3–23.

Plouff, D., 1976. Gravity And Magnetic Fields of Polygonal Prisms and Application To Magnetic Terrain Corrections. GEOPHYSICS. https://doi.org/10.1190/1.1440645

Quesada, C., 1991. Geological constraints on the Paleozoic tectonic evolution of tectonostratigraphic terranes in the Iberian Massif. Tectonophysics, 185(3–4), 225–245.

Ramos, A., Fernández, O., Terrinha, P., Muñoz, J.A., 2017. Neogene to recent contraction and basin inversion along the Nubia-Iberia boundary in SW Iberia. Tectonics 36, 257–286.

Ramos, A., Fernández, O., Terrinha, P., Muñoz, J.A., 2016. Extension and inversion structures in the Tethys–Atlantic linkage zone, Algarve Basin, Portugal. Int. J. Earth Sci 105, 1663–1679.

Ribeiro, A. et al., 1979. Introdution Á la Geologie Génerale Du Portugal. Serv. Geol. Portugal.

Ribeiro, P., Silva, P.F., Moita, P., Kratinová, Z., Marques, F.O., Henry, B., 2013. Palaeomagnetism in the Sines massif (SW Iberia) revisited: evidences for late cretaceous hydrothermal alteration and associated partial remagnetization. Geophysical Journal International 195, 176–191. https://doi.org/10.1093/gji/ggt261

Rocha, J.P., Bezzeghoud, M., Caldeira, B., Borges, J.F., Dia, N., Matias, L., Dorbath, C., 2010. Tomografia sísmica da litosfera continental algarvia.

Rock, N.M.S., 1982. Chemical mineralogy of the Monchique alkaline complex, southern Portugal. Contributions to Mineralogy and Petrology 81, 64–78. https://doi.org/10.1007/BF00371160

Rock, N.M.S., 1979. Petrology and origin of the type monchiquites lamprophyre dykes of Serra de Monchique, Portugal. Trans. of the Royal Soc. Edimburgh 70, 149–170.

ROCK, N.M.S., 1978. Petrology and Petrogenesis of the Monchique Alkaline Complex, Southern Portugal. Journal of Petrology 19, 171–214. https://doi.org/10.1093/petrology/19.2.171

Rodrigues, B., Chew, D.M., Jorge, R.C.G.S., Fernandes, P., 2014. História térmica do Grupo do Flysch do Baixo Alentejo, Zona Sul Portuguesa Thermal history of Baixo Alentejo Flysch Group, South Portuguese Zone, Especial I.

Salah, M.K., 2014. Upper crustal structure beneath Southwest Iberia north of the convergent boundary between the Eurasian and African plates. Geoscience Frontiers 5. https://doi.org/10.1016/j.gsf.2013.10.002

Sallarès, V., Gailler, A., Gutscher, M.-A., Graindorge, D., Bartolomé, R., Gràcia, E., Díaz, J., Dañobeitia, J.J., Zitellini, N., 2011. Seismic evidence for the presence of Jurassic oceanic crust in the central Gulf of Cadiz (SW Iberian margin). Earth and Planetary Science Letters 311, 112–123. https://doi.org/https://doi.org/10.1016/j.epsl.2011.09.003

Saltus, R.W., Blakely, R.J., 2011. Unique geologic insights from "non-unique" gravity and magnetic interpretation. GSA Today 21, 4–11. https://doi.org/10.1130/G136A.1

Sartori, R., Torelli, L., Zitellini, N., Peis, D., Lodolo, E., 1994. Eastern segment of the Azores-Gibraltar line (central-eastern Atlantic): An oceanic plate boundary with diffuse compressional deformation. Geology 22. https://doi.org/10.1130/0091-7613(1994)022<0555:ESOTAG>2.3.CO;2

Schubert, G., 2007. Treatise on Geophysics. https://doi.org/10.1016/C2009-1-28330-4

Serpelloni, E., Vannucci, G., Pondrelli, S., Argnani, A., Casula, G., Anzidei, M., Baldi, P., Gasperini, P., 2007. Kinematics of the Western Africa-Eurasia plate boundary from focal mechanisms and GPS data. Geophysical Journal International 169. https://doi.org/10.1111/j.1365-246X.2007.03367.x

Silva, J.B., Oliveira, J.T., Ribeiro, A., 1990. Structural outline. South Portuguese Zone. Dallmeyer R.D. & Martínez García, E. (Eds.) Pre-Mesozoic Geology of Iberia. Springer, (Berlim- Heidelverg-Nova Iorque), 348–363.

Simancas, J., Poyatos, D., Expósito, I., Azor, A., Lodeiro, F., 2001. The structure of a major suture zone in the SW Iberian Massif: the Ossa- Morena/Central Iberian contact. Tectonophysics 332, 295–308.

Simancas, J.F., Carbonell, R., González Lodeiro, F., Pérez Estaún, A., Juhlin, C., Ayarza, P., Kashubin, A., Azor, A., Martínez Poyatos, D., Almodóvar, G.R., Pascual, E., Sáez, R., Expósito, I., 2003. Crustal structure of the transpressional Variscan orogen of SW Iberia: SW Iberia deep seismic reflection profile (IBERSEIS). Tectonics 22. https://doi.org/10.1029/2002TC001479

Soares, A., 2018. Caracterização da Actividade Sísmica de Monchique. Master thesis, University of Lisbon.

Socias and Mezcua, 2002. Mapa de Anomalías Magnéticas de la Península Ibérica Confeccionado el mapa transnacional de España y Portugal.

Sousa, F.L.P., 1926. La Serra de Monchique.

Stich, D., Ammon, C.J., Morales, J., 2003. Moment tensor solutions for small and moderate earthquakes in the Ibero-Maghreb region. Journal of Geophysical Research: Solid Earth 108. https://doi.org/10.1029/2002JB002057

Stich, D., Martín, R., Morales, J., 2010. Moment tensor inversion for Iberia–Maghreb earthquakes 2005–2008. Tectonophysics 483. https://doi.org/10.1016/j.tecto.2009.11.006

Tait, J.A., Bachtadse, V., Franke, W., Soffel, H.C., 1997. Geodynamic evolution of the European Variscan fold belt: palaeomagnetic and geological constraints. Geologische Rundschau 86(3), 585–598.

Terrinha, P., 1998. Structural Geology and Tectonic Evolution of theAlgarve Basin, South Portugal.

Terrinha, P., Matias, L., Vicente, J., Duarte, J., Luís, J., Pinheiro, L., Lourenço, N., Diez, S., Rosas, F., Magalhães, V., Valadares, V., Zitellini, N., Roque, C., Víctor, L.M., 2009. Morphotectonics and strain partitioning at the Iberia–Africa plate boundary from multibeam and seismic reflection data. Marine Geology 267, 156–174. https://doi.org/https://doi.org/10.1016/j.margeo.2009.09.012

Terrinha, P., Medialdea, T., Batista, L., Somoza, L., Magalhães, V., González, F.J., Noiva, J., Lobato, A., Rosa, M., Marino, E., Brito, P., Neres, M., Ribeiro, C., 2020. Integrated thematic geological mapping of the Atlantic Margin of Iberia. Geological Society, London, Special Publications SP505-2019–90. https://doi.org/10.1144/sp505-2019-90

Terrinha, P., Pinheiro, L.M., Henriet, J.-P., Matias, L., Ivanov, M.K., Monteiro, J.H., Akhmetzhanov, A., Volkonskaya, A., Cunha, T., Shaskin, P., Rovere, M., 2003. Tsunamigenic-seismogenic structures, neotectonics, sedimentary processes and slope instability on the southwest Portuguese Margin. Marine Geology 195. https://doi.org/10.1016/S0025-3227(02)00682-5

Terrinha, P., Pueyo, E.L., Aranguren, A., Kullberg, J.C., Kullberg, M.C., Casas-Sainz, A., Azevedo, M. do R., 2018. Gravimetric and magnetic fabric study of the Sintra Igneous complex: laccolith-plug emplacement in the Western Iberian passive margin. International Journal of Earth Sciences 107, 1807–1833. https://doi.org/10.1007/s00531-017-1573-7

Terrinha, P., Ramos, A., Neres, M., Valadares, V., Duarte, J., Martínez-Loriente, S., Silva, S., Mata, J., Kullberg, J.C., Casas-Sainz, A., Matias, L., Fernández, Ó., Muñoz, J.A., Ribeiro, C., Font, E., Neves, C., Roque, C., Rosas, F., Pinheiro, L., Bartolomé, R., Sallarès, V., Magalhães, V., Medialdea, T., Somoza, L., Gràcia, E., Hensen, C., Gutscher, M.-A., Ribeiro, A., Zitellini, N., 2019. The Alpine Orogeny in the West and Southwest Iberia Margins. https://doi.org/10.1007/978-3-030-11295-0_11

Terrinha, P., Ribeiro, C., Kullberg, J., Lopes, C., Rocha, R., Ribeiro, A., 2002. Compressive episodes and faunal isolation during rifting, Southwest Iberia. J. Geol. 110, 101–113.

Terrinha, P.A.G., 1998. Structural Geology and Tectonic Evolution of the Algarve Basin, South Portugal. Imperial College London (University of London).

Valadares, V., 2004. O Complexo Alcalino de Monchique: novos dados de cartografia, geoquímica e geocronologia.

Veludo, I., Dias, N.A., Fonseca, P.E., Matias, L., Carrilho, F., Haberland, C., Villaseñor, A., 2017. Crustal seismic structure beneath Portugal and southern Galicia (Western Iberia) and the role of Variscan inheritance. Tectonophysics 717, 645–664. https://doi.org/10.1016/j.tecto.2017.08.018

Verati, C., Rapaille, C., Féraud, G., Marzoli, A., Bertrand, H., Youbi, N., 2007. 40Ar/39Ar ages and duration of the Central Atlantic Magmatic Province volcanism in Morocco and Portugal and its relation to the Triassic–Jurassic boundary. Palaeogeography, Palaeoclimatology, Palaeoecology 244. https://doi.org/10.1016/j.palaeo.2006.06.033

Zitellini, N., Gràcia, E., Matias, L., Terrinha, P., Abreu, M.A., DeAlteriis, G., Henriet, J.P., Dañobeitia, J.J., Masson, D.G., Mulder, T., 2009. The quest for the Africa–Eurasia plate boundary west of the Strait of Gibraltar. Earth and Planetary Science Letters 280. https://doi.org/10.1016/j.epsl.2008.12.005

A. Appendix

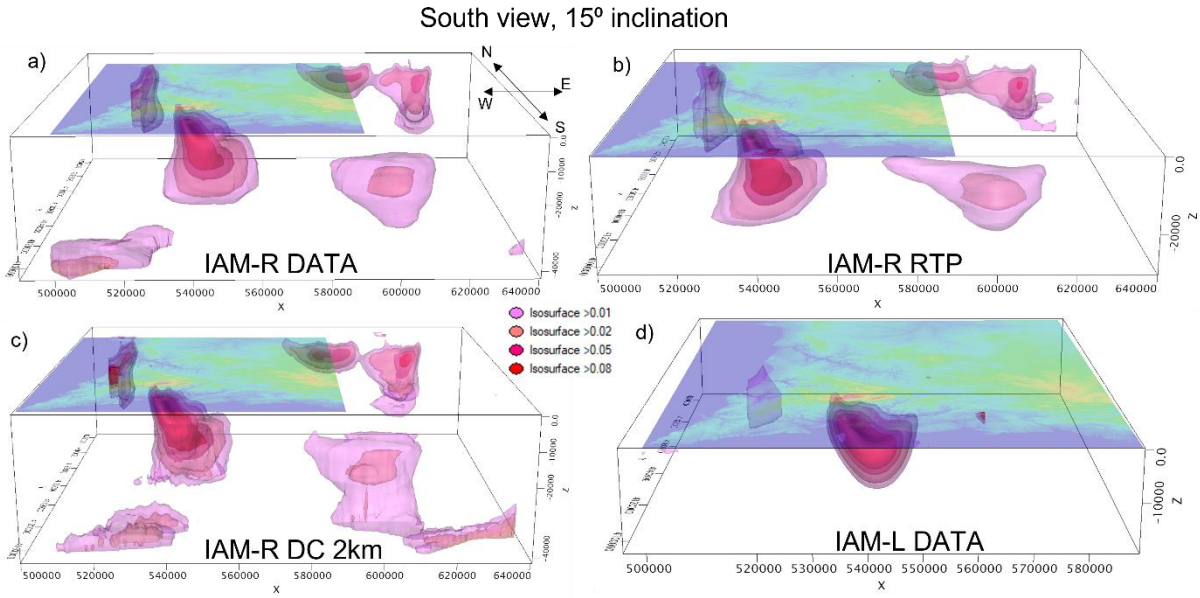

Figure A.1 IAM (Iberian anomaly map) resulted magnetic susceptibility models in South view, inclination of 15º: a) IAM-R (regional) model; b) IAM-R RTP (reduced to pole) model; c) IAM-R DC2km (downward continued for 2 km); and d) IAM-L (localized) model. Shown as isosurfaces of >0.01, >0.02, >0.05 and >0.08 SI. All with the topography map of the localized region for Monchique.

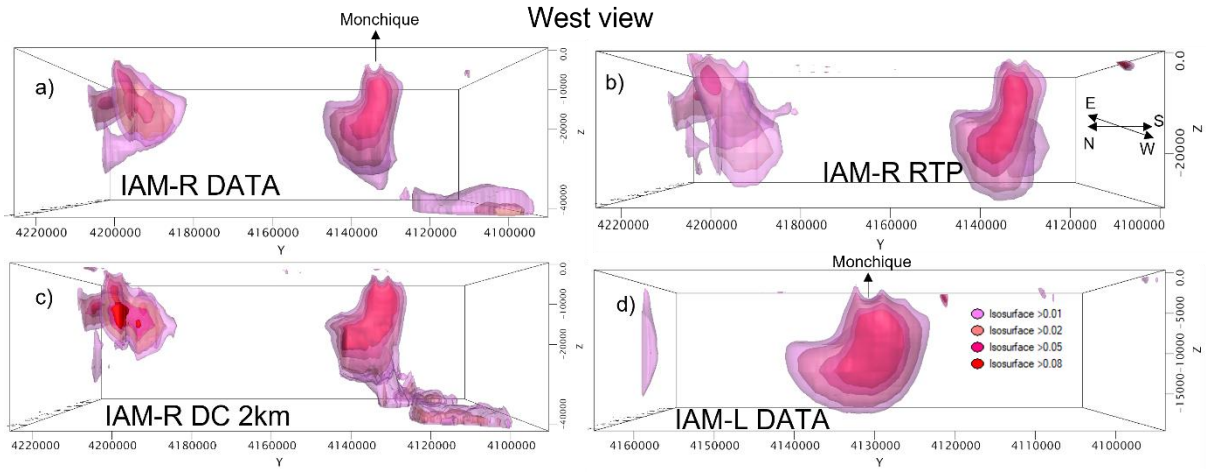

Figure A.2 IAM resulted magnetic susceptibility models in west view: a) IAM-R (regional) model; b) IAM-R RTP (reduced to pole) model; c) IAM-R DC 2km (downward continued for 2 km); and d) IAM-L (localized) model. Shown as isosurfaces of >0.01, >0.02, >0.05 and >0.08 SI.

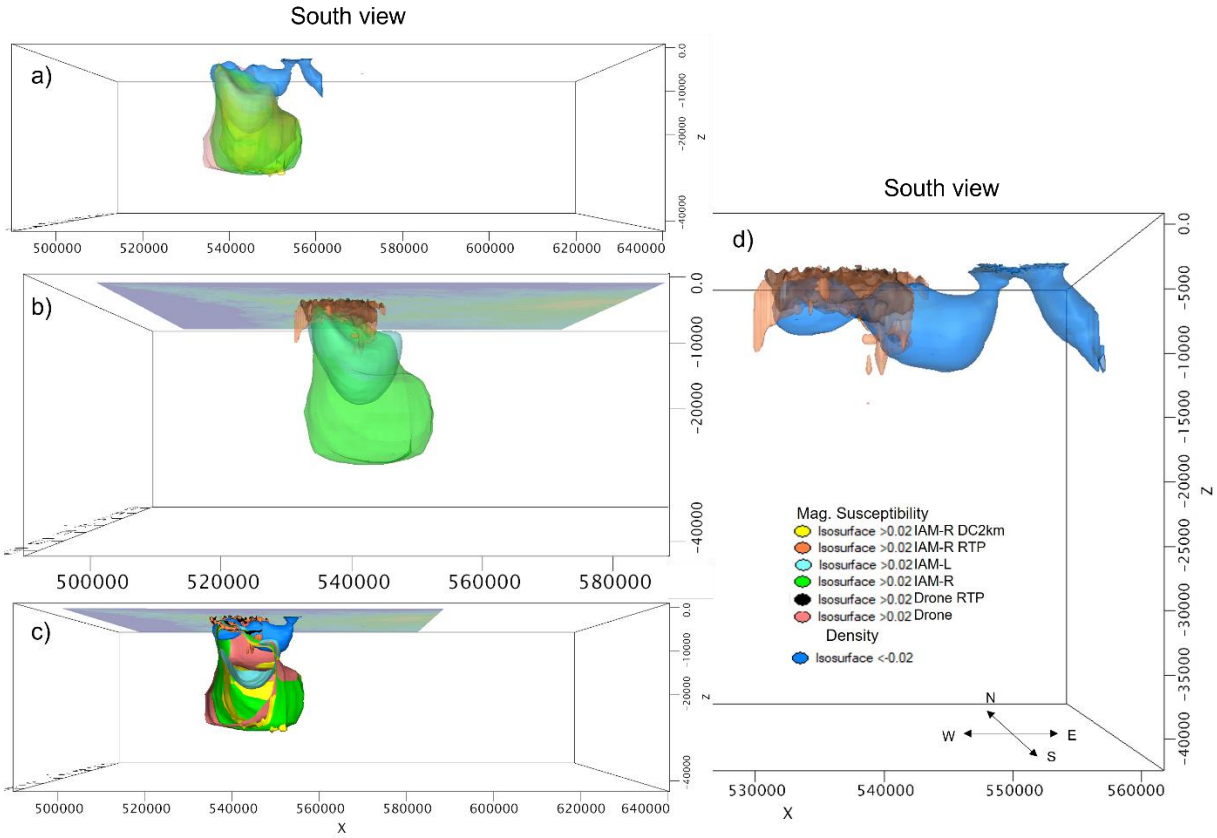

Figure A.3 Models overlap viewed from South: a) Overlap of IAM models and density model; b) overlap of IAM-l and IAM-R models and drone models; c) Overlap of all models cut on A3-A4 section (EW); d) Magnetic susceptibility models for drone data with density models overlapped, viewed from South (density values of <-0.02 or ρ<2650 kg/m^3).